Investigation of microparticles behavior in Newtonian, viscoelastic, and shear-thickening flows in straight microfluidic channels

Mohammad Charjouei Moghadam

A THESIS SUBMITTED TO
THE FACULTY OF GRADUATE STUDIES
IN PARTIAL FULFILLMENT OF THE REQUIREMENTS
FOR THE DEGREE OF
MASTER OF APPLIED SCIENCE

Graduate Program in
MECHANICAL ENGINEERING

York University
Toronto, Ontario
December 2021

Abstract

Sorting and separation of small substances such as cells, microorganisms, and micro- and nano-particles from a heterogeneous mixture is a common sample preparation step in many areas of biology, biotechnology, and medicine. Portability and inexpensive design of microfluidic-based sorting systems have benefited many of these biomedical applications. The mechanism of particle focusing and separation in complex biological (like blood) and environmental (like contaminated water) samples is less understood due to their rheological complexity. Accordingly, we have investigated microparticle hydrodynamics in fluids with various rheological behaviors (i.e., Newtonian, shear-thinning viscoelastic and shear-thickening non-Newtonian) flowing in straight microchannels. Numerical models were developed to simulate particles trajectories in Newtonian water (Objective 1) and shear-thinning polyethylene oxide (PEO) (Objective 2) solutions. These models were verified and validated against past experimental works done in our group and also available works in the literature. The validated models were then used to perform numerical parametric studies and non-dimensional analysis on the Newtonian inertia-magnetic and shear-thinning elasto-inertal focusing regimes. The studied parameters included channel cross section shape, particle size, magnetization, fluid viscosity, flow rate and channel width. For the shear-thinning elasto-inertial regime, a non-dimensional study was carried out considering the important non-dimensional numbers such as the Reynolds number (Re), Deborah number (De), dimensionless channel length (L) and blockage ratio (β). Based on this investigation, the commonly used design threshold, i.e., $\mathrm{De} \cdot \mathrm{L} \cdot \beta^2 = 1$, for particle focusing was modified and a new threshold was proposed ($\mathrm{De} \cdot \mathrm{Re}^{0.2} \cdot \mathrm{L} \cdot \beta^2 = 5$). This reduced particles dispersion throughout the width of the channel from $\sim 20\%$ to $\sim 3\%$. Based on this analysis and the new thresholding

scheme, an empirical non-dimensional correlation was developed to predict elasto-inertial particle dispersion in straight square cross section microchannels. Using this new correlation, variation in predicted dispersion was reduced from ∼15% to less than ∼5%. Finally, the straight microfluidic device that was tested for Newtonian water and shear-thinning viscoelastic PEO solution, were adopted to experimentally study microparticle behavior in SiO_2/Water shear-thickening nanofluid (Objective 3). For the same experimental conditions, we observed two side focusing lines of microparticles in shear-thickening fluids in contrast to dispersion in Newtonian and single line center focusing in shear-thinning fluids. The effects of significant parameters including flow rate, particle size and nanofluid concentration were then investigated on shear-thickening particle focusing. These experimental observations are reported for the first time in the literature, and they can facilitate and lead to more fundamental theoretical studies in this field in the future. The presented numerical models, proposed design threshold and predictive equation can be used as reliable tools to simulate and optimize the design of microfluidic particle sorters.

Acknowledgements

I would like to start by thanking my supervisor, Dr. Pouya Rezai for giving me the opportunity to take this project at the ACμTE lab and for his continuous guidance and support during this time. Throughout my master's and above all the technical aspects, I learned that success is a process of small consistent efforts guided by passion and humility. The chance to work among such a hard-working and down to earth group of friends was one of the most formative life experiences I ever had.

I would like to appreciate the continuous support and encouragement of my co-supervisor, Dr. Armin Eilaghi. I would also like to thank the time and consideration of my defense committee Prof. Amirfazli and Prof. Karimpour who kindly examined and critically reviewed my thesis.

I would like to express my sincere gratitude and love to my wonderful parents, Fahimeh and Saeed, my smart brother, Masoud whose continuous and unconditional love and support was the drive for me to go on. This thesis would not have been finished without them. I am also thankful to my dear friends in Iran, Canada and USA who were always there for me in happiness and sadness, despite the miles and borders between us. Thank you, Ali, Arsalan, Alireza, Matin, Pouriya, Sajed and Iman.

Table of Contents

List of Tables

List of Figures

Chapter 1
INTRODUCTION AND LITERATURE REVIEW

1.1 Introduction and Motivation

The current global pandemic revealed that rapid diagnostic testing of patients, and later on, large-scale monitoring of environmental samples like water and air, are key actions needed for containing the novel coronavirus SARS-CoV-2 spread [24]. In a more general sense and in many infectious disease applications, rapid and on-site sample preparation and monitoring systems are urgently needed to devise appropriate prevention and remediation plans [25, 26]. Current research is trending towards development of rapid, low cost, and sensitive technologies for sample preparation and monitoring at the Point-of-Use (PoU)* for various biotechnological applications such as diagnosis [27], genomics [28, 29], cellomics [30] and immunoassays [31].

Typically, fluidic samples obtained from nature (e.g., ground water), aqueous foods (e.g., raw milk), and/or bodily fluids (e.g., blood) are relatively complex fluids containing a mixture of debris, cells such as white and red blood cells, microorganisms like bacteria and viruses, and potentially other organisms like parasites, creating a heterogeneous matrix of particles [32]. Furthermore, rheological complexity of these fluids, e.g., Newtonian† versus non-Newtonian‡ (viscosity changing with shear rate) behavior, would introduce new challenges and opportunities

* The location after sample acquisition when the technology, products and/or service is used .
† A Newtonian fluid is a fluid in which the viscous stresses arising from its flow, at every point, are linearly correlated to the local strain rate—the rate of change of its deformation over time.
‡ A non-Newtonian fluid is a fluid that does not follow Newton's law of viscosity, i.e., constant viscosity independent of stress. In non-Newtonian fluids, viscosity can change when under force to either more liquid or more solid.

for PoU sample preparation and particle detection [33]. In general, the research in this thesis was inspired by these types of fluids where various rheological properties of fluids and their effects on microparticles hydrodynamics in micro-environments were aimed to be studied.

The main focus of research on PoU devices has been placed on microparticles smaller than ~50µm due to challenges associated with their isolation and detection. Sub-50µm particles include most of the biological cells and microorganisms (called bioparticles), while larger particles suspended in these fluids can be manipulated easily using conventional systems like filters and centrifugation [34].

One of the most challenging and time-consuming steps in detecting bioparticles is the sample preparation process wherein the target bioparticle should be labeled, sorted, and separated from the rest of the content [35]. This will enhance the downstream detection process by ensuring that detection inhibitors are removed from these multi-phase fluids. As mentioned earlier, sample preparation is preferred to be conducted at the points of sample acquisition, so that target bio-contaminants can be detected rapidly with portable sensors to prevent outbreaks and corrective actions can be undertaken more effectively [36, 37]. Accordingly, portable devices are needed that can carry out sample preparation and analysis with a relatively low cost and ease of use, where the operator does not have to interfere with the process of handling samples that can introduce noise and error down to the detection module.

Laboratory-based methodologies for particle and cell sorting usually involve sedimentation, filtration, or centrifugation. These methods are known to be time-consuming, prone to filter clogging, and expensive. Other commonly used methods such as Fluorescence-Activated Cell Sorting [38, 39] and Magnetic-Activated Cell Sorting [40] are more accurate and specific to target cells. But they require compatibility with fluorescent tagging and in-line fluorescent imaging, analysis and downstream sorting that makes them costly, complex and inaccessible especially for PoU applications.

Biological testing and sample preparation at the PoU using portable devices has accelerated the movement towards miniaturization of electromechanical systems for fluid handling and analyte detection in recent years [41, 42]. An ideal sorting method must meet certain requirements such as offering a simple and low-cost design, working continuously at high throughput, being efficient in terms of energy consumption, operating without a diluting sheath flow and performing multiplex separation with high purity and efficiency [21].

Recently, many biological practices such as cancer diagnosis [43-48], immunomagnetic assays [49, 50] and pathogen separation [51-54] have benefitted from microfluidic-based sorting systems that meet most of these requirements above and exceed expectations by offering minimal reagent consumption and portability [55, 56]. In addition to their compact, inexpensive, and disposable characteristics, microfluidics ability to manipulate small amounts of fluid (on the scale of microliters and below) in microchannels has significantly decreased the required volumes of samples and reagents. Due to these characteristics and as a major step in sample preparation, a growing field of research is involved in micro- and nano-particle sorting and separation at the PoU with microfluidic devices [57]. Below, we review various microfluidic techniques that have been reported for particle separation and their applications in the aforementioned fields. This review aims to bring out the knowledge and technical gaps in this domain to justify the research performed in this thesis.

1.2 Microfluidic Particle Sorting Methods

Microfluidic particle separation methods can be categorized into two groups based on their separation mechanisms and the forces exerted on the particles. If particles are separated from each other solely due to the hydrodynamic forces applied from the fluid flow, the technique is called a *Passive Sorting Method*. In cases where there are external sources of energy (other than the pump that moves the fluid) and external forces are exerted on the particles, the technique is called an *Active Sorting Method*. Another way to categorize microfluidic sorters is by the nature of their base fluid, i.e., being Newtonian or non-Newtonian. In the next sections, we will review the passive and active sorting methods with their applications in particle separation in Newtonian and non-Newtonian viscoelastic fluids. These studies are done in the context of experimental and numerical works as reviewed briefly in sections 1.2.1 and 1.2.2, respectively.

1.2.1 Experimental Techniques in Microfluidics Microparticle Sorting

1.2.1.1 Passive Microfluidics Sorting Methods

Drag and inertial forces (described further in chapter 2 sections 2.1.2.2) exerted from the fluid to the particles and the laminar hydrodynamic behavior of the flow can be used to separate particles from each other in passive microfluidic devices [58]. Particle size is a major characteristic affecting the magnitude of these forces. Therefore, many methods have been developed to sort particles based on their hydraulic diameters. Among these passive sorting methods, Deterministic Lateral Displacement (DLD) [59], Pinched Flow Fractionation (PFF) [3], and inertial microfluidics [60] in straight [7] and spiral [53] microchannels can be named.

DLD was first developed in 2004 by Huang et al. [59]. As shown in Fig. 1-1a, this method uses an array of small pillars in a channel to separate the particles based on their sizes. DLD works because around each pillar, the smaller particles remain in the same streamline while the larger particles enter a new streamline due to the force exerted on them from the pillar (F_{DLD}) and thus become separated from the smaller particles [61]. In Fig. 1-1a, the size and configuration of pillars and their arrangement direction inside the channel help moving all the large particles to the right and all the small particles almost straight through the channel. DLD microdevices can be modified to separate multiple particles by using a series of different pillar arrays to separate different particles from the stream, one at a time (Fig. 1-1b) [2]. Among the applications of this method, separating blood cells (red, white, and platelets) from the plasma is the most common [2, 61]. This method can be disadvantageous due to its relatively low-throughput and frequent blockage by particle clogging in between the pillars.

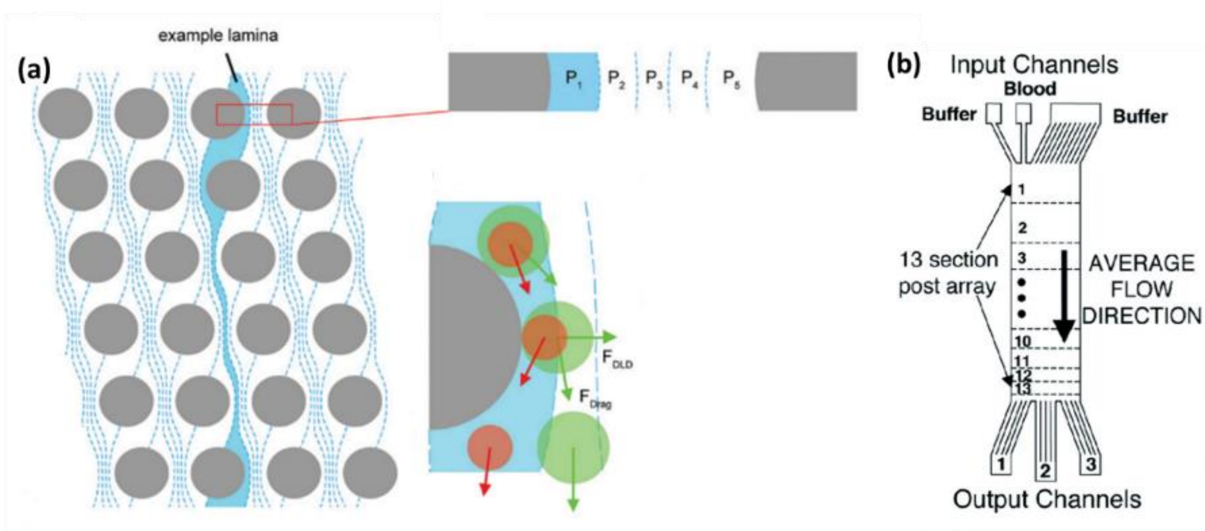

Figure 4-1. (a) Deterministic Lateral Displacement (DLD) separation method using an array of micropillars in a microchannel. Larger particles are separated from the smaller particles and move to another streamline due to the force exerted from the pillar [1]. (b) Using a series of pillars with different configurations to separate multiple particles or cells from each other [2]. Permissions obtained from RSC.

PFF was also introduced in 2004 by Yamada et al. [3]. As shown in Fig. 1-2a, PFF devices have two inlets with different flow rates, a pinched section with a small cross-section, and an expansion zone. They can separate two particles based on their size (Fig. 1-2a insert). The upper inlet containing the particle solution has a lower flow rate than the lower inlet containing the sheath flow. In the pinched section, particles with different sizes take position at different streamlines with the aid of the sheath flow and become separated at the downstream expansion zone. Vig and Kristensen [4] have attempted to enhance the performance and separation efficiency of the PFF method by adding an additional segment in the expansion zone as shown in Fig. 1-2b, which expands the part of the flow in which the two particle streams are present. A major drawback of this method is the need for the sheath flow which dilutes the solution and requires higher control on the flow rates using equipment such as additional syringe pumps.

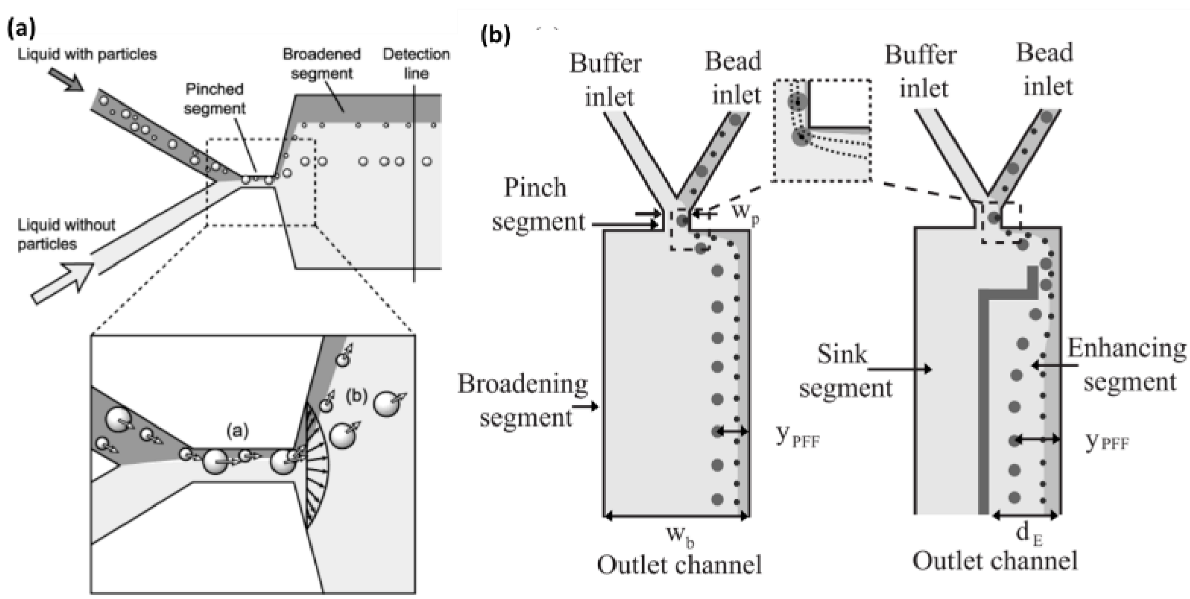

Figure 1-5 (a) Pinched Flow Fractionation (PFF) method using a pinched section to separate particles based on their size [3]. (b) Modifying the PFF channel to enhance the separation efficiency [4]. Permissions obtained from ACS and AIP.

One of the most frequently used passive methods is the exploitation of size-dependent inertial forces on the particles to focus and separate them in straight and spiral channels. In Newtonian flows, when the diameter of the particle, d_p, is considerably large in accordance to the hydraulic diameter of the channel, D_h, the inertial forces can help focus the particles (with $\frac{dp}{D_h} > 0.07$) at equilibrium positions on the center of the walls depending on the flow condition and the channel geometry [62]. This condition is achieved when the particle's Reynolds number ($Re_p = Re(d_p/L_c)^2$, where *Re* is the Reynolds number, and L_c is the channel characteristic length or the channel's narrowest dimension) is in the order of unity. This area of research is called inertial separation or inertial microfluidics [63, 64].

Inertial separation in straight channels can happen in various device designs which will be discussed among a few examples. Generally, all these devices implement the difference between the magnitude of inertial forces for particles with different sizes. This method works since the particles tend to focus at the centers of the long cross-sectional walls in a rectangular microchannel, due to the balance between the shear- and wall-induced inertial lift forces as shown in Fig. 1-3a and described further in Chapter 2. Zhou et al. [6] introduced an inertial microfluidic separation device (Fig. 1-3b) in which two different particles first focus inertially at the center of the longer channel walls in a high-aspect-ratio channel (height>width). Then, a change in the channel aspect ratio polarity resulted in the inertial migration of larger particles to new focusing points and their separation from the smaller particles which were not strongly affected by inertial forces in the low aspect ratio region. Wang et al. [7] implemented the same idea but with modifications to make it easier to fabricate the device, due to difficulties associated with making high-aspect-ratio channels (Fig. 1-3c). In their device, all particles first focus at the center of the longer wall in a low-aspect-ratio channel while only the larger particles re-focus inertially after channel bifurcation and become separated from the smaller particles. Wang and Papautsky [7] developed a device to perform separation in multiple steps and achieve multiplex separation (Fig. 1-3d). In this method, particles were focused at the center of the long walls in a high-aspect-ratio channel. The larger particle could then be separated from the stream by placing an expansion and contraction vortex generator section beside the channel.

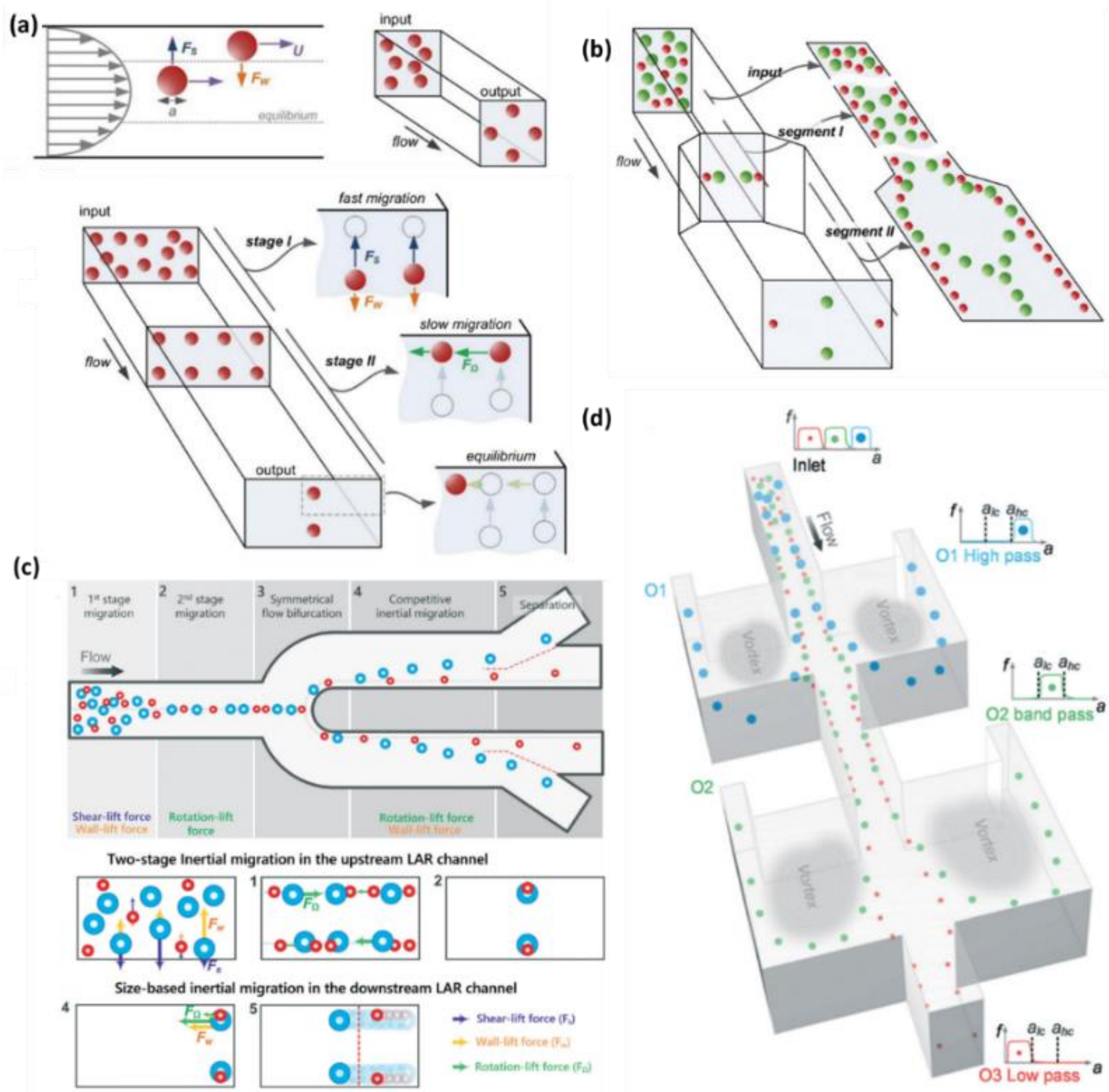

Figure 1-6 (a) Inertial particle focusing in a rectangular microchannel under the effect of shear-induced (F_s) and wall-induced (F_w) inertial forces [5]. (b) Separation of particles based on their size by changing the aspect ratio of the channel [6]. (c) Separation of particles based on their size by bifurcating the channel [7]. (d) Multiplex separation of particles based on their size with multiple separation steps and vortex sections beside the channel [8]. Permissions obtained from RSC.

Inertial separation offers simple design using straight microchannels, a high throughput, and no need for a sheath buffer flow. However, its performance is limited to separating two particles at a time. This happens since particles tend to focus at two to four channel sides in rectangular or square cross-sections, respectively. Multiple separation steps or active controls are needed to separate more than two particles based on their sizes. Inertial particle manipulation is a major method that was investigated in this thesis, so more details about this method will be provided in Chapter 2.

1.2.1.2. Active Microfluidics Sorting Methods

One major advantage of active sorting methods over the passive ones is their capability of sorting particles based on their intrinsic characteristics such as magnetic [65, 66], dielectric [67, 68] or optical [69, 70] properties rather than just their size. Among the active microfluidic sorting methods, magnetophoretic sorting with permanent magnets has attracted a lot of attention due to its semi-passive nature, yet specificity and high precision in sorting target biomarkers [58, 71-77]. Various microfluidics magnetophoretic methods are proposed to perform microfluidic magnetic separation and among the more conventional ones, we can name multitarget magnetic activated cell sorter (MT-MACS) [78], H-shaped magnetic separator [79], and on-chip free flow magnetophoresis [75]. On-chip free flow magnetophoresis was developed by Pamme and Manz in 2004 [9]. In this method, a laminar stream of sample solution enters the separation chamber, along with multiple laminar streams of a buffer. In the separation chamber, magnetic particles deflect from their stream toward a magnet beside the channel. The amount of deflection differs for magnetic particles with different sizes. The non-magnetic particles continue in the same stream as they enter the chamber. Separation of two magnetic particles from a non-magnetic particle has been reported using this device (Fig. 1-4). Dr. Pamme and her group later published several papers on the development and applications of this method in cell detection and separation [75, 80-82].

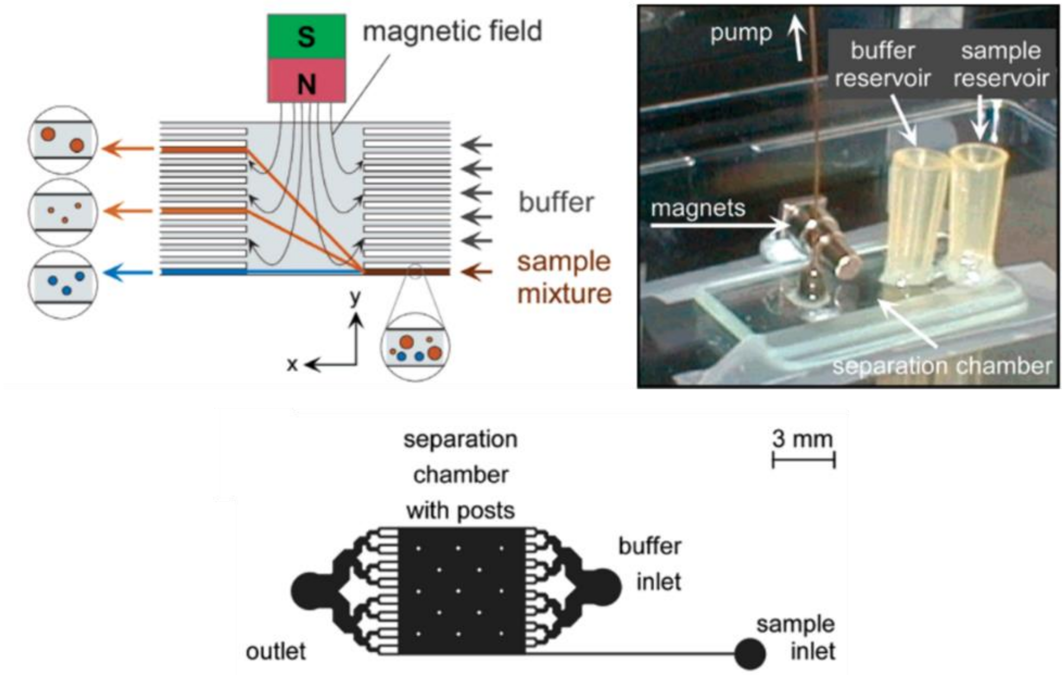

Figure 1-4 On-chip Free Flow Magnetophoresis method schematic, actual device and design [9]. Permissions obtained from ACS.

The passive sorting methods can also be combined with the active techniques to create hybrid separation approaches with improved performances in terms of multiplexing and separation efficiency. Recently, a separation device based on multiplex inertia-magnetic fractionation (MIMF) was developed by our group to sort magnetic and non-magnetic particles in water (Fig. 1-5) [10, 21]. In this high-throughput and sheathless device, 5, 11, 15 µm magnetic and 35 µm non-magnetic particles were inertially focused in a rectangular straight channel and separated from each other at an expansion zone based on their size, due to the use of the permanent magnet beside the channel. The magnitudes of inertial and magnetic forces which depend on the size of particles aligned them in different equilibrium positions which led to their separation at the expansion zone (Fig. 1-5). This device has become the basis of investigation in this thesis as it provides a straight channel for fundamental particle focusing studies, a downstream expansion zone for particle visualization under a microscope, the possibility of testing fluids with various viscosity properties, and lastly, offering the ability to introduce active forces if needed, such as magnetic force, in the focusing zone to perform hybrid sorting analysis.

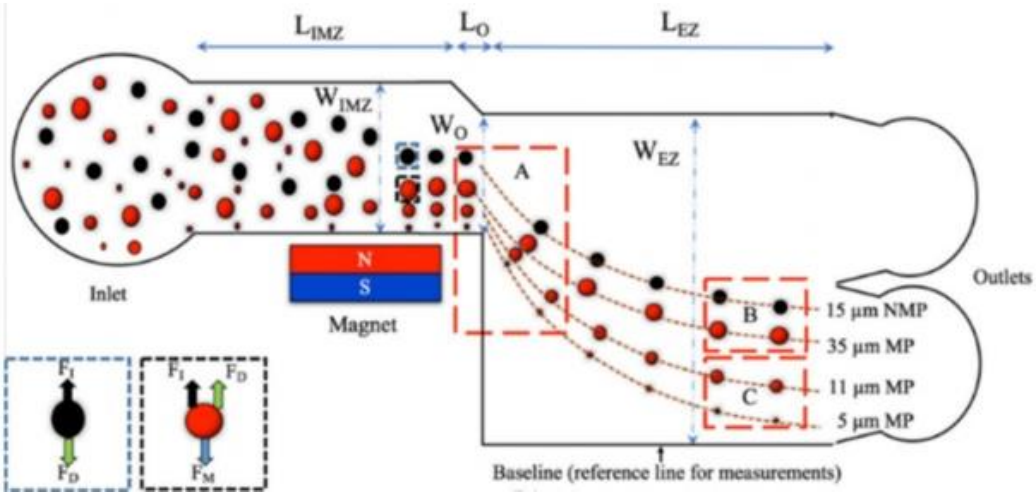

Figure 1-5 Multiplex Inertio-Magnetic Fractionation (MIMF) method for separation of three magnetic particles from a non-magnetic particle. Particles attain different equilibrium positions due to the balance between inertial lift (F_I), drag (F_D), and magnetic (F_M) forces. [10]. Permissions obtained from Springer Nature.

By using continuous flow magnetophoresis [10], the selective separation of microparticles and cells was possible due to their continuous deflection through multiple reagent and washing streams resulting in a large reduction in processing times [77]. There is great potential for magnetophoretic microfluidic devices for cell isolation and separation with high throughput and purity. These devices acquire innovative features and become more precise, more robust and automated [77]. This could be obtained by realizing microfluidic devices based on soft magnetic microelements with different structures, geometries, and arrangements to enable precise generation of high gradient magnetic field in specific regions[83]. Further improvement could be realized by merging various passive or active manipulation techniques along with the magnetophoresis to yield higher purity and throughput [77].

1.2.1.3 Shear-Thinning Viscoelastic Fluids in Microfluidics

The above-mentioned passive and active techniques have mostly used water with Newtonian properties as their carrier fluid. Nevertheless, in many of the biological, water and wastewater, and food testing applications, the carrier fluid is a non-Newtonian fluid such as blood [84], saliva [85], DNA solutions [86] and milk [87]. Their non-Newtonian behavior is due to the abundance of deformable cells or ling molecular chains in their complex structure [88]. In non-Newtonian viscoelastic fluids, the viscosity of the fluid is not constant and changes with the shear rate. This can introduce new forces on the particles (e.g. viscoelastic lift) [89] that could be taken advantage of as a passive approach in particle focusing and separation (further discussed in Chapter 2). Viscoelastic fluids can also be synthetically formed by dissolving polymers in water or another Newtonian medium [14, 23, 90-93]. Examples include mixing polymers like polyvinylpyrrolidone (PVP) [23], polyethylene oxide (PEO) used in this thesis [90, 91], polyacrylamide (PAA)[93], and hyaluronic acid (HA) [92] with water. In viscoelastic fluids, an elastic force (described in Chapter 2) is exerted on the particles in addition to the common inertial and drag forces present in non-Newtonian flows [94]. If the elastic force is dominant over the inertial force, particles will focus at the center and the four corners of the channel (Fig. 1-6b). But, if the elastic and inertial forces are comparable, a centerline focusing at the center of the channel can occur (Fig. 1-6c). This phenomenon (called elasto-inertial focusing) turns out to be very useful in particle separation and enhancing the separation quality of previous methods as single-stream focusing is not easily achievable in Newtonian fluids.

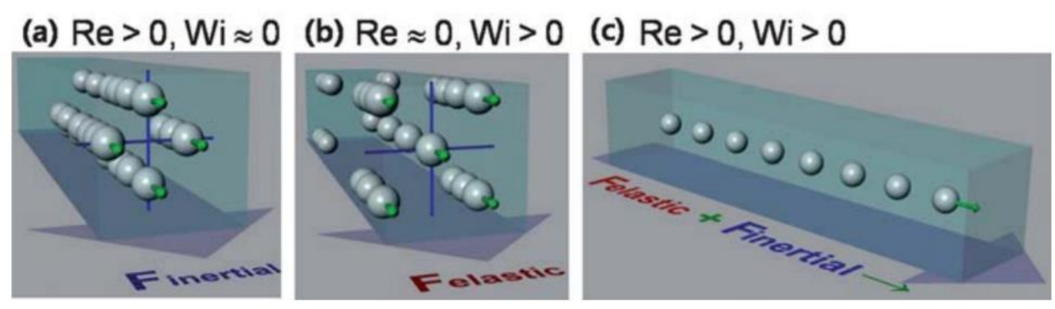

Figure 1-6 Particle focusing under (a) inertial, (b) elastic, and (c) elasto-inertial regime [11]. These focusing situations will be described in depth in Chapter 2. Permissions obtained from RSC.

The earliest study of particle manipulation in non-Newtonian fluid flows through rectangular microchannels was performed by Leshansky et al. [33]. They demonstrated a tunable viscoelastic focusing of particles in a shallow microchannel (45 µm high, 1000 µm wide) in dilute polymer solutions. In such a slit-like channel, the flow becomes essentially 2D with insignificant corner effects, and hence the elastic lift force directs particles toward the midplane. The observed lateral migrations were explained by a simple 2D theory based on scaling arguments for particles of different sizes in both 8% PVP and 45 ppm PAA (mixed with 76 wt.% glycerol) solutions at various flow rates. Particle focusing in viscoelastic fluid flows through straight square microchannels has thus far been studied the most in the literature [88]. Faridi et al. used the concept of elasto-inertial separation [12] to develop a microfluidic device that separates bacteria from blood cells (Fig. 1-7). In their device, bacteria-infected blood enters a square microchannel from two sides while a viscoelastic buffer enters the channel from the center. Blood cells which are larger than bacteria focus at the center and exit the device from the center outlet, while the bacteria remain in the original stream and exit from the side outlets. This technique could be useful in the diagnosis of sepsis or Bloodstream Infections (BSI).

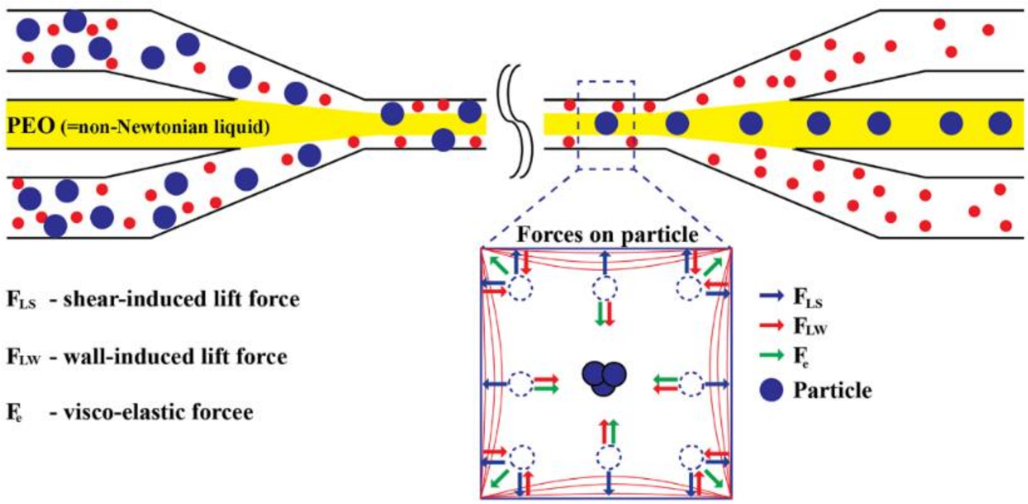

Figure 1-7 Schematic illustration of elasto-inertial microfluidics-based particle migration and separation in flow through straight channel. The net result of elastic (F_e) and inertial forces (shear-induced lift force, F_{LS}, and wall-induced lift force, F_{LW}) would focus larger particles at the center [12]. Permissions obtained from Analytical Chemistry.

Existing passive methods have been modified and optimized to take advantage of elasto-inertial focusing such as DLD [13], PFF [14], and inertial separation in straight [95] and spiral [90] channels. Using DLD method, Li et al. [13] showed separation of two particles in viscoelastic fluids (Fig. 1-8). They demonstrated that the elasticity of the fluid which affects the shear rate gives an additional means for controlling the separation process in the DLD device and thus, the critical separation size can be dynamically controlled. They reported an increase of up to 40% in separation size by changing the viscoelastic properties of the fluid.

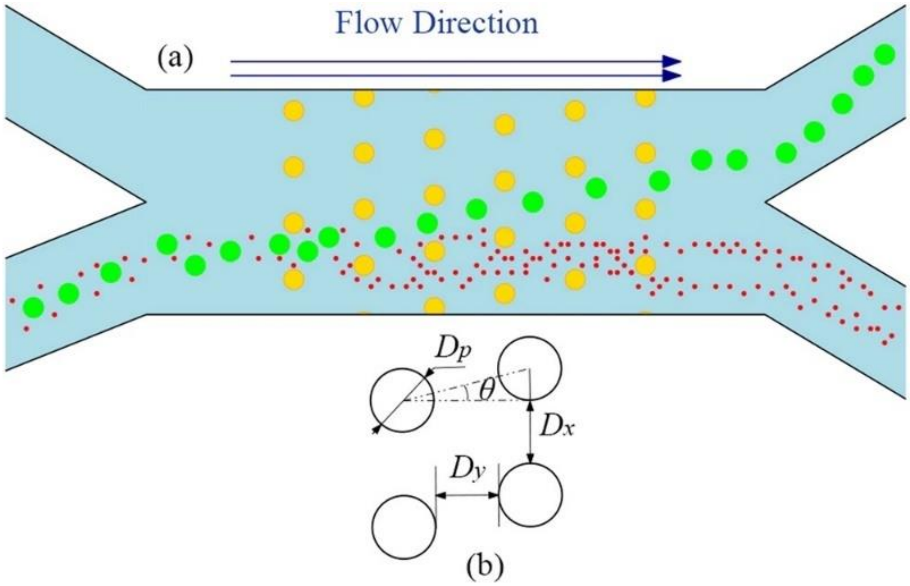

Figure 1-8 Schematics of (a) a DLD device with periodic pillar arrays (yellow) and how large particles (green) and small particles (red) are separated, (b) a unit of rhombic posts with diameter Dp. [13]. Permissions obtained from Nature.

Lu and Xuan [14] combined viscoelastic flows with conventional PFF and called their method elasto-inertial pinched flow fractionation (eiPFF) (Fig. 1-9). They concluded that in comparison to the conventional PFF, their method would significantly enhance the throughput and separation resolution due to the presence of additional elastic force especially on larger particles which pushes them towards the center of the pinched section and reinforces their separation from the smaller particles.

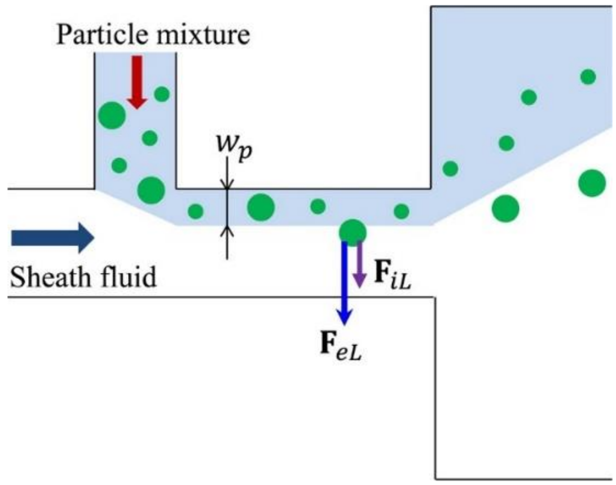

Figure 1-9. Schematic illustration of the mechanism for eiPFF. The sheath-fluid focused particle-mixture solution has a width of w_p in the main-branch. The net result of $\boldsymbol{F}_{el}$ (the elastic lift force) and $\boldsymbol{F}_{iL}$ (the inertial lift force) would separate larger particles and focus them lower to the center of the channel. [14]. Permissions obtained from Analytical Chemistry.

In a more recent work by our group [15], an inertia-magneto-elastic microfluidic device (Fig. 1-10) was designed to separate particles taking advantage of shear-thinning viscoelastic fluid properties as well as particle size and magneticity. This was an improved version of the device shown in Fig. 1-5 for testing PEO-water viscoelastic liquids with suspended microparticles. Particles would focus at the center of the straight microchannel due to elasto-inertial effects after which separation occurs as they would enter the magnetic field. Non-magnetic particles would continue at their straight path while magnetic ones are pulled towards the magnet. Magnetophoretic force is more dominant than elasto-inertial lift forces on smaller particles (9 µm) as they are pulled towards the lower side of the channel. Larger magnetic particles (15 µm) are focused between the centerline and the lower side as the elaso-inertial lift forces become more significant. This device is capable of triplex sorting of 9 µm and 15 µm magnetic microparticles and 15 µm non-magnetic microparticles with high efficiency and purity (94.8% and 96.6% respectively) which shows its high potential for biological applications. Once again, this device was used as a platform for our numerical and experimental studies in this thesis due to its advantages introduced earlier in this chapter. The research gaps related to the devices and experiments in Fig. 1-5 and 1-10 will be discussed later in this chapter.

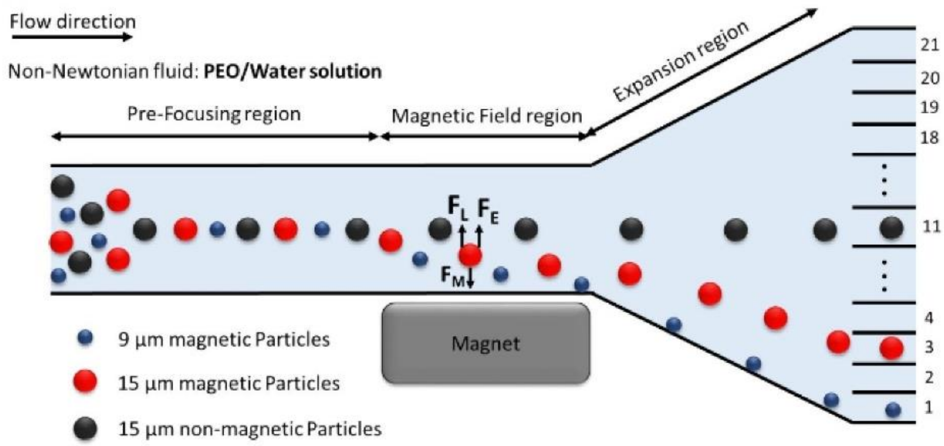

Figure 1-10 Schematic of the triplex sorting of 9 and 15 µm magnetic particles (MP) and 15 µm non-magnetic particles (NMP) in a viscoelastic fluid, showing the inertial (F_L), elastic (F_E) and magnetic (F_M) forces on the MP. Stokes drag force always opposes the direction of lateral motion of a particle and is not shown in here [15]. Permissions obtained from Elsevier.

In the past decade, particle migration phenomena induced by the viscoelasticity of the suspending medium have been greatly clarified, and much success has been achieved [96]. In perspective, however, some key points need to be examined. As remarked by Karimi et al. [97], an open issue is that the viscoelasticity-induced migration mechanism, although effective over a relatively wide range of flow rates, is partly constrained to low–Reynolds number regimes, with obvious implications on the overall accessible throughput. A proper rheo-engineering of the fluid, in line with the work by Nam et al. [95], might lead to enhanced throughputs by using viscoelastic liquids with low viscosity and high elasticity.

Even though shear-thinning viscoelastic fluids are routinely utilized in microfluidics sorting, non-Newtonian effects are not limited to that of shear-thinning. Contrary to the shear-thinning behavior, the fluid viscosity might increase with the shear rate. These fluids are known as shear-thickening fluids or STFs [98]. Shear thickening fluids hold promise in many industrial applications. Patenting activity has involved both specific applications and the preparation of the STFs themselves. Their current applications could be categorized in three main branches namely; devices with adaptive stiffness and damping [99], smart structures [100] and body amour [101]. Despite the plethora of fundamental and technical research on shear-thinning viscoelastic microfluidics, the behavior of shear-thickening fluids in microfluidics is less explored and the available works are scarce in literature. In the next section, we briefly review the origins of shear-thickening behavior in non-Newtonian suspensions and their applicability in microfluidics.

1.2.1.4 Shear-Thickening non-Newtonian Fluids, and Opportunities in Microfluidics

Shear thickening fluids represent a subset of certain non-Newtonian fluids that exhibit increased viscosity with an increase of shear rate [102]. The origins of shear-thickening behavior in colloidal suspensions are debated in recent literature [103-106]. Whilst shear thickening has been observed and reported for around a century, most early accounts were simply qualitative and did not consider the microstructural rearrangements responsible [107]. The first attempt at explaining the microstructure came from the work by Hoffman [108-110]. It was demonstrated by Hoffman that for a number of polymer particle suspensions, an ordered hexagonally packed layers appeared prior to the shear thickening transition. Hoffman proposed that these ordered layers formed and moved across each other at low shear rates, resulting in the shear thinning region. At higher shear rates, the repulsive forces between particles are overcome, increasing viscosity. However, with other dispersions, the formation of an ordered structure is prior to shear thickening [111].

Another major and more recently developed viewpoint for shear thickening fluids is the theory of *hydro clusters* (Fig. 1-11) [112]. In short, this theory states that as the external force exceeds a certain critical value, the dispersed phase deviate from the equilibrium position and cannot return in time, so that they gather to form hydroclusters. In the flow process, when the relaxation time (the characteristic time in which a system relaxes under certain changes in external conditions) is longer than the convection time (the characteristic time for mass transfer due to the bulk motion of a fluid), the hydroclusters will be formed and grow, resulting in higher viscosity [113].

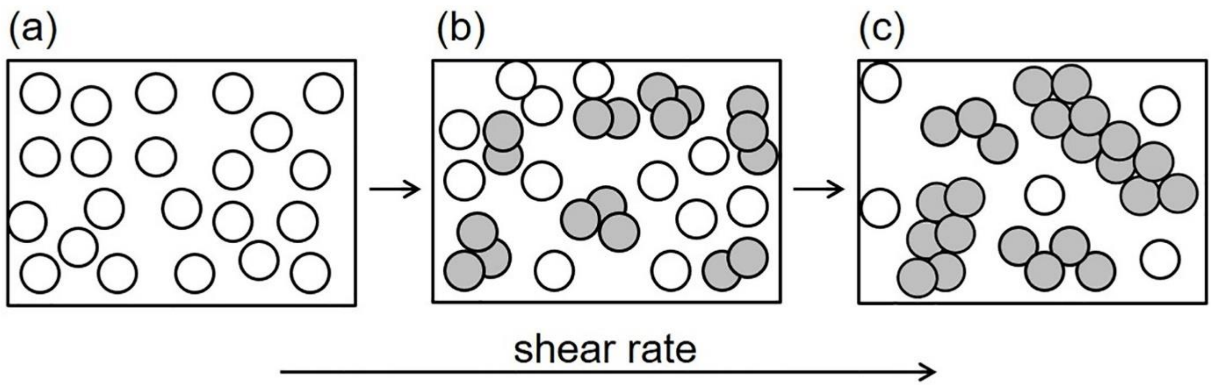

Figure 1-11 Schematic illustrating hydroclusters formation [16]. Permission obtained from RSC.

Fig. 1-11a illustrates a slight change in the microstructure of a suspension at low shear rates, although Brownian motion is able to restore the initial configuration, which in turn results in a slight variation in viscosity values. As the shear rate increases, the structure loses its regeneration capacity, and the microstructural changes compose small aggregates that orient in the flow direction. This process leads to a suspension with reduced viscosity and, thus, to a shear-thinning behavior (Fig. 1-11b). As the shear rate is increased further, hydrodynamic forces prevail in the system and its structure is drastically modified as a greater number of aggregates is formed. When the shear rate is greater than a critical value, small aggregates assemble in view of hydrodynamic forces and form hydroclusters. These hydroclusters act as barriers that contribute to a greater resistance to flow, i.e. a much higher viscosity (Fig. 1-11c) [16].

Among the colloidal suspensions, some nanofluids [114] (suspensions of nanoparticles dispersed in a base liquid phase) are known to show shear-thickening behavior. Their rheology is complex and depends on the parameters of the suspended phase [115] such as the nanoparticle size, concentration, and shape. It is also reported that the properties of the suspending phase [109, 116-118] such as viscosity, shear, extensional flow, steady or transient flow, time and rate of deformation, surfactant and even electrical or magnetic field [115] would impact the rheology of the nanofluids.

Nanofluids such as SiO_2 nanoparticle in water are reported to show shear thickening behavior even in very low nanoparticle concentrations (< 1 wt%) [17]. Moldoveanu et al. [17] experimentally studied the viscosity of SiO_2/Water nanofluids for shear rates between 0.01 and 1000 s^{-1} (Fig. 1-12). They confirmed the shear-thickening behavior of SiO_2/Water nanofluid in their investigated shear rates and proposed a power law equation to model the viscosity.

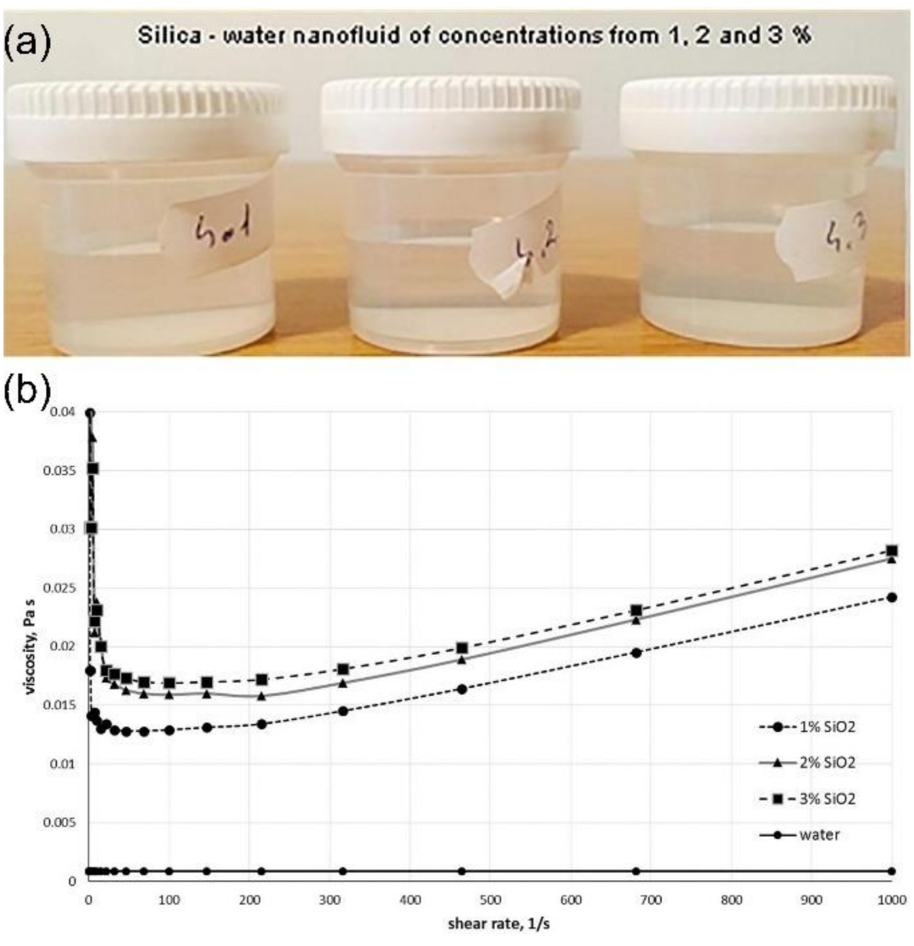

Figure 1-12 (a) Prepared SiO2/water nanofluids with various concentrations (1, 2 and 3 wt%) and their (b) viscosity measurements at various shear rates (0<γ<1000 s^{-1}) [17]. Permission obtained from Elsevier.

In a more recent study, Gu et al. investigated the shear thickening behavior of SiO_2/water nanofluids of various concentrations (< 0.2 wt%) at different shear rates ($0 < \gamma < 3500\ s^{-1}$) by a double-direction shear test (Fig. 1-13) [18]. They also studied the reversibility of viscosity change in this nanofluid. They hypothesized that the shear-thickening mechanism of nanofluids is that the particle aggregation is caused by the separation of particles and base liquid due to high velocity [18].

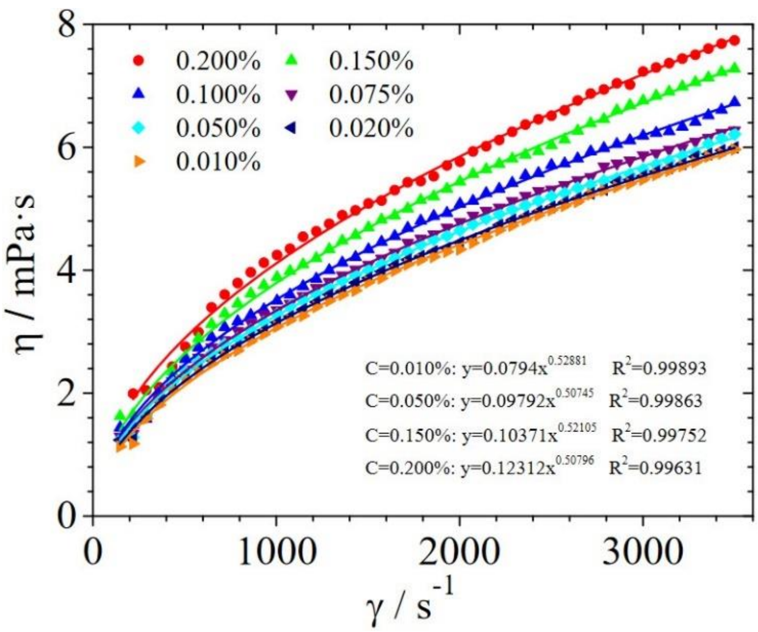

Figure 1-13 Viscosity measurement of SiO2/water NF in various concentrations (< 0.2 wt%) and shear rates ($0<\gamma<3500\ s^{-1}$)[18]. Permission obtained from AGER.

In addition to its shear-thickening behavior, SiO_2/Water nanofluids are also reported to be highly homogeneous and transparent at the above concentrations [17]. All these characteristics make this shear-thickening nanofluid an ideal choice to be investigated as a carrier fluid for other microparticles in microchannels. Whether or not the shear-thickening behavior of this nanofluid would cause microparticles to focus in microchannels is a fundamental research question that remains to be answered.

So far, we have reviewed major experimental works in microfluidics particle sorting. Even though experimental investigations are informative and always needed, at early investigation stages they can be time-consuming, resource-intensive and limited in depth and breadth of study.

Numerical methods have been adopted to facilitate the design of microfluidic-based particle sorting systems. In the next section we review the numerical techniques that are developed to study and design various microfluidics particle sorting methods.

1.2.2 Numerical Techniques in Microfluidics Microparticle Sorting

Recently, numerical approaches have been utilized to obtain better insights into the underlying physics of particle migration in microfluidics. In particular, fundamental aspects of particle focusing inside straight and curved microchannels have been explored in detail to determine the dependence of focusing behavior on particle size, channel shape, and flow Reynolds number [119]. Starting with simulating the motion of spherical particles in a fluid medium, earlier models [120, 121] were mostly limited to either 2D domains or simple geometries [122, 123]. Recently, more complex geometries such as straight, spiral and T-shaped microchannels have been simulated [62, 124]. A major advantage that these models can provide is the capability to investigate the effect of multiple dominant forces on particle focusing and separation, such as the combined effects of inertial focusing and magnetophoresis on magnetic particles.

Polyflow [122, 123] and CFD-ACE [62, 125, 126] programs were among the popular numerical solvers adopted for simulation. These solvers were abandoned due to their inability to accommodate the multi-physical complexity of the microfluidic-based sorting systems. COMSOL Multiphysics and ANSYS-Fluent are being adopted nowadays as they cover a wide range of numerical analyses with accuracy and simplicity. For instance, in 2015, Amin [127] performed a simulation on the effects of inertial focusing in a spiral microchannel with a trapezoidal cross section employing the discrete phase model (DPM) of ANSYS-Fluent. Particles' trajectories were calculated considering the dominant forces acting on them including the drag, buoyant, and lift forces. The lift force was included in the force balance through the addition of a User Defined Function (UDF). A polynomial approximation based on the variations of the lift coefficient with Re number was derived to predict the lift coefficient. In a more recent study, Parrot [128] utilized a similar numerical framework and modified the proposed lift coefficient based on the particle distance from the sidewall rather than the Re number. They were able to successfully model the focusing behavior of particles in accordance with empirical results. However, their model was only applicable to a limited range of Reynolds numbers.

As the experimental microfluidics works progressed towards adoption of active methods, so did the numerical techniques. One major challenge was to accurately model the impact of magnetophoretic force among other active forces. Numerical studies on magnetophoretic microfluidic-based sorting systems, are scarce in the literature [129]. Among the earlier studies, analytical models [130, 131] and CFD-ACE+ program [126] were adopted for simulation. Specialized numerical models [132, 133] have also been developed to simulate specific cases. Forbes and Forry [134] developed a numerical model to investigate microfluidic magnetophoretic separation of immunomagnetically labeled rare mammalian cells. Their model accounts for the magnetic orientation, magnet type, flow rate, channel geometry, and buffer to achieve the desired level of magnetophoretic deflection or capturing. Hale and Darabi [135] utilized COMSOL Multiphysics to simulate their magnetophoretic microfluidic device for DNA isolation and studied the effect of various parameters on the magnetic flux within a separation channel. In another study, Kim et al. [136] used a similar COMSOL approach as Hale and Darabi [135] and modeled hydrodynamic viscous drag and magnetophoretic repulsion forces to predict particle trajectories in their microfluidic device. Their model showed that the strength of the magnetic field is proportional to the magnetic force generated by the magnet at the bottom of the channel, and an asymmetric magnetic field is generated to cause the lateral migration of the particles. Its acceptable accuracy and the fact that it ran on a commercial simulation platform are the main advantages of this numerical approach [136] for modeling the magnetophoretic force in microfluidics.

The numerical works in microfluidics are not limited to Newtonian fluids. As for non-Newtonian viscoelastic fluids, one major approach for simulation of particles in viscoelastic medium is based on the Oldroyd-B constitutive model (described later in Chapter 2) [89]. This approach is most accurate in applications with Deborah number ($\mathrm{De} = \frac{\text{Elastic force}}{\text{Viscous force}}$) larger than 2., Trofa et al [137] developed an Arbitrary Lagrangian–Eulerian (ALE) formulation to account for both the effects of inertia and viscoelasticity. They were able to accurately simulate particle motion on a wider range of De and Re numbers. They found that, for comparable values of the Deborah and Reynolds numbers, inertial effects are negligible: migration is in practice driven by fluid viscoelasticity only. At moderate Reynolds numbers ($20 < \mathrm{Re} < 200$) and by lowering De, the transition from viscoelasticity-driven to inertia-driven regimes occurs through two intermediate regimes characterized by multiple stable solutions, i.e. attractors of particle trajectories at different vertical positions across the gap [137]. In another work in 2017, Lee and Ahn [19] developed a Lattice-Boltzmann numerical algorithm to investigate dynamics of single rigid particle suspended in viscoelastic medium (Fig. 1-14). To validate their algorithm, three benchmark problems (two-dimensional simulation) were tested; viscoelastic flow past a cylinder, a single particle migration in a viscoelastic Couette flow, and dynamics of two particles in a viscoelastic Couette flow. Simulation results were compared with previous simulation results implemented by finite element method (FEM) and finite volume method (FVM). They concluded that hydrodynamic properties and the motion of the particles induced by viscoelasticity are correctly captured. As a first report, this study has its significance, which solves the flow behavior of solid particles immersed in a viscoelastic medium on the LBM framework [19].

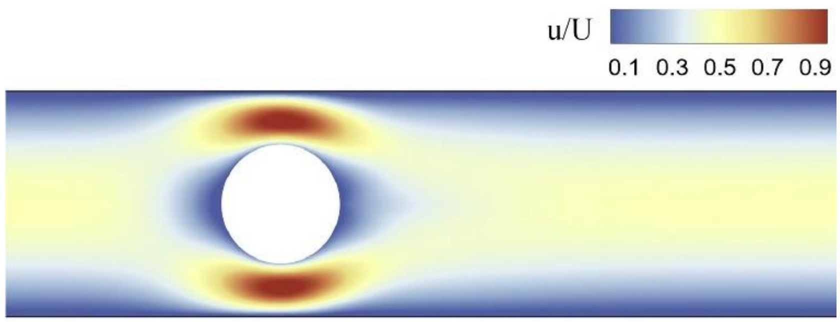

Figure 1-14 Simulation contours of normalized streamwise velocity, u/U around a single rigid particle suspended in viscoelastic medium of De = 2.0 [19]. Permission obtained from the Journal of Non-Newtonian Fluid Mechanics.

In one of the more recent numerical works on viscoelastic focusing, Raoufi et al [20] developed a DNS approach to study elasto-inertial focusing of particles in straight channel (Fig. 1-15). They numerically explored the effects of elasticity, channel cross-sectional geometry and sample flow rates on the focusing phenomenon in elasto-inertial systems. Their results revealed that increasing the aspect ratio weakens the elastic force more than inertial force, causing a transition from one focusing position to two. They also concluded that increasing the channel width weakens the elastic force more than the inertial force, causing one focusing band in a square channel to increase to two bands in a rectangular cross-section [20]. Despite the widely accepted merit of DNS approaches for fundamental flow studies, they are known to require increased computational resources and sophisticated coding knowledge to implement on regular large-scale simulations [119, 138].

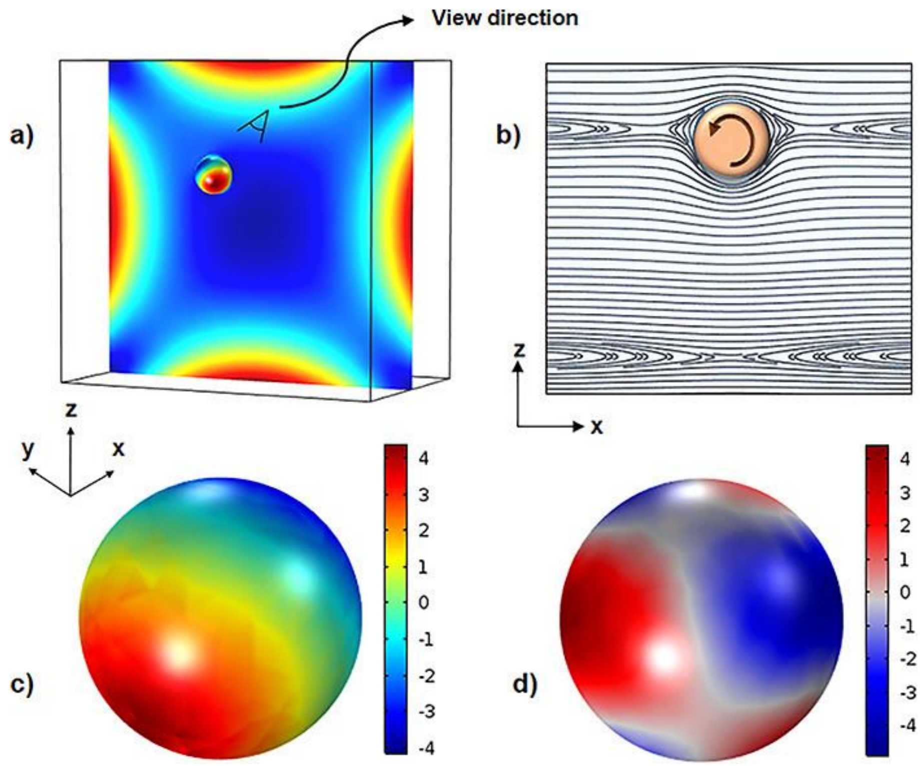

Figure 1-15 DNS of elast-inertial focusing by Raoufi et al. [20] (a) Contour of first normal stress difference ($N1$) and pressure in the cross section of the channel and over the particle, respectively, for a flow rate of 25 µl/min. (b) Streamlines around the particle in the x-z symmetry plane. (c) Distribution of non-dimensional inertial and (d) elastic stresses on the surface of the particles. Permission obtained from the AIP Biomicrofluidics.

To design microfluidic devices in inertia-elastic regime, one major threshold that is commonly used is the one proposed by Del Giudice et al. [23]. This threshold considers the effects of non-dimensional numbers such as De and nondimensional channel length ($L = \frac{Channel\ Length}{Channel\ Hydraulic\ Diamater}$) and blockage ratio ($\beta = \frac{Particle\ Diameter}{Channel\ Hydraulic\ Diamater}$) on particle dispersion in straight microchannels. They reported that when $De \cdot L \cdot \beta^2 \geq 1$, elasto-inertial focusing is realized. One way to obviate the need for expensive simulations is to use parametric thresholds such as the one proposed by Del. Giudice et al. [23] to design microchannels. This threshold, though being very advantageous in many aspects, might not always provide the most accurate predictions as it is developed based on a 15-point parametric investigation and does not consider the effects of inertia as offered by the Re number.

1.3 Research Opportunity, Objectives, and Activities

Numerical methods are being used to facilitate the design of microfluidics sorting systems and expand on experimental outcomes. Based on our literature survey, a numerical framework which accounts for all the effects of magnetophoretic focusing, inertial and drag forces as well as hydrodynamic fractionation is currently lacking. With the help of such model, the unknown effects of various parameters such as magnetization, particle size and flow viscosity on inertia-magnetic focusing of microparticles in our experimentally tested straight microfluidic device [21] could be investigated. When it comes to design of elasto-inertial sorting systems, a full-scale parametric study to investigate the effects of all non-dimensional numbers (De, Re, L and β) that could be implemented on the readily available commercial solvers is also needed. With the help of such numerical framework, the validity of the earlier proposed particle focusing thresholds (section 1.2.2) could be verified and if needed modified to accurately predict particle focusing in straight microchannels with viscoelastic flows. Such parametric study and design threshold could lead to a more accurate prediction criteria for elasto-inertial focusing of microparticles flowing in straight microchannels. Finally, as discussed in section 1.2.1.4, given the potential of shear-thickening SiO_2/water nanofluid to be injected in microchannels, the straight microfluidic device that were tested for Newtonian and shear-thinning non-Newtonian fluids in our group [15] could be utilized to experimentally study microparticle behavior flowing in shear-thickening non-Newtonian fluids for the first time.

To address the abovementioned research gaps, the following objectives were defined in this thesis:

1- Developing a comprehensive numerical platform to parametrically study inertia-magnetic microparticle focusing in Newtonian Fluids in straight microchannels.

2- Expanding the numerical model in objective 1 to non-Newtonian fluids to study the elasto-inertial focusing in shear-thinning viscoelastic fluids and optimize previously proposed design criteria for particle focusing in straight microchannels.

3- Investigating microparticle focusing in shear-thickening non-Newtonian fluids in straight microchannels.

The present research attempts to accomplish these objectives by conducting the following activities.

1- Studying the physics of particle migration in viscoelastic fluids; inertial, elastic and elasto-inertial focusing; and the rheology of shear-thickening fluids and their applicability in microfluidics.

2- Studying and identifying the shortcomings of numerical methods in microfluidics particle focusing with a focus on inertia-magnetic and elasto-inertial regimes.

3- Developing, validating, and performing numerical simulations to model inertia-magnetic and elasto-inertial microfluidics particle sorting.

4- Performing a parametric study on inertia-magnetic and elasto-inertial microfluidic particle focusing and proposing a modified threshold for design of elasto-inertial microfluidic sorting systems.

5- Performing experiments and demonstrating particle focusing in shear-thickening nanofluids in a straight microchannel.

6- Developing an in-house image processing code in Python to quantify and characterize the shear-thickening particle focusing experiments.

7- Performing a parametric study to identify the impact of relevant parameters on particle focusing efficiency in shear-thickening fluids.

1.4 Thesis Structure

In Chapter 2, we have discussed the theory of inertia-magnetic and elasto-inertial focusing, the non-dimensional numbers that can be used to understand these regimes and the details of our numerical schemes used in simulations. Also, in this chapter, we have presented the geometry of the microfluidic devices under study, experimental setup, device fabrication, sample preparation, and data analysis processes used in Chapters 3. Chapter 3 includes the results and discussions of the parametric numerical studies on inertia-magnetic and the elasto-inertial microfluidics sorting. Furthermore, we demonstrated microparticle focusing in shear-thickening nanofluids the results of this study is also presented in chapter 3 . Chapter 4 presents a summary of this thesis, its limitations, and ideas for the future work to continue this project.

Chapter 2

NUMERICAL AND EXPERIMENTAL METHODS§

The research in this thesis involved both numerical (objectives 1 and 2) and experimental (objective 3) investigations of microparticle focusing in water, PEO-water (shear-thinning), and SiO_2-water (shear-thickening) fluids, all within straight microchannels (Fig. 1-5 and Fig 1-10). To supplement the numerical objectives 1 and 2 of the thesis (mentioned in section 1.3) with experimental data for model validation, we used the results that were developed previously in our group [15, 21]. It is important to note that we have not conducted new experiments for objectives 1 and 2 and only used the previous experimental results conducted in our group [15, 21] for validation of our developed numerical models. These results are based on experimental works performed on two microfluidic devices, as depicted in Fig. 2-1 and Fig. 2-2. These devices involved a straight microchannel inside which fluids with various viscosity properties were flown, i.e., Newtonian water for objective 1 and shear-thinning PEO-water for objective 2. Microparticles with various sizes and magnetic properties were also suspended in these fluids and tested for focusing in various flow conditions within microchannels. Downstream the straight microchannels, an expansion region was implemented within which the microparticles' velocity was dropped so that they could be imaged under a microscope. In this thesis, we used the above past experimental data to validate our numerical models, then took advantage of them to expand

§ Some of the text of this chapter is extracted from the author's published journal papers below:

139. Moghadam, M.C., A. Eilaghi, and P. Rezai, *Inertia-magnetic particle sorting in microfluidic devices: a numerical parametric investigation.* Microfluidics and Nanofluidics, 2019. **23**(12): p. 135.

140. Charjouei Moghadam, M., A. Eilaghi, and P. Rezai, *Elasto-inertial microparticle focusing in straight microchannels: A numerical parametric investigation.* Physics of Fluids, 2021. **33**(9): p. 092002.

the knowledge in the field in objectives 1 and 2 by performing fundamental parametric investigation of microparticle focusing in microchannels. For this purpose, the numerical models were developed to simulate the inertial, magnetic, and viscoelastic focusing of microparticles in microchannels similar to the experimental channels above. Hybrid modes of particle focusing were also investigated in these models, hence the simulation schemes for inertia-magnetic and elasto-inertial focusing behaviors, respectively for our first and second objectives, are described in section 2.1. For the third objective, i.e., experimental investigation of particle behavior in shear-thickening SiO_2-water fluids (section 2.2), the same straight microfluidic device that was modeled for the shear-thinning PEO-water fluid in section 2.1 was microfabricated and tested. This research enabled us to compare the effects of Newtonian, shear-thinning, and shear-thickening flows on microparticle hydrodynamics in the same microfluidic geometry, as later discussed in the final chapter of the thesis.

The numerical and experimental methods of the thesis are described in sections 2.1 and 2.2, respectively, while the theory of microparticle focusing and the physics behind various modes of focusing such as inertial, magnetic. and viscoelastic effects are described within section 2.1.

2.1 Numerical Modeling

This section describes the geometry, theory, and the equations that were used in the numerical models to investigate the inertia-magnetic focusing of microparticles in Newtonian fluids and elasto-inertial focusing in shear-thinning non-Newtonian fluids as defined by the first and second objectives in section 1.3.

2.1.1 Model Geometries

2.1.1.1 Inertial and Magnetic Particle Focusing in Newtonian Fluids (Inertia-Magnetic Regime)

To satisfy the 1st thesis objective, inertial and magnetic focusing of microparticles flowing in Newtonian deionized (DI)-water in the straight microchannel similar to an experimental work in our group [21] was modeled in ANSYS Fluent. The schematic diagram and geometrical specifications of the modeled device is presented in Fig. 2-1. The model is a microfluidic device consisting of three regions, namely the inertia-magnetic focusing zone, the middle narrowing section, and the asymmetric hydrodynamic expansion zone. The inertia-magnetic focusing zone was designed as a narrow microchannel over which the magnetic particles (MPs) were affected by inertial and magnetic forces, caused by the flow hydrodynamics and a permanent magnet located by the side of the channel, respectively.

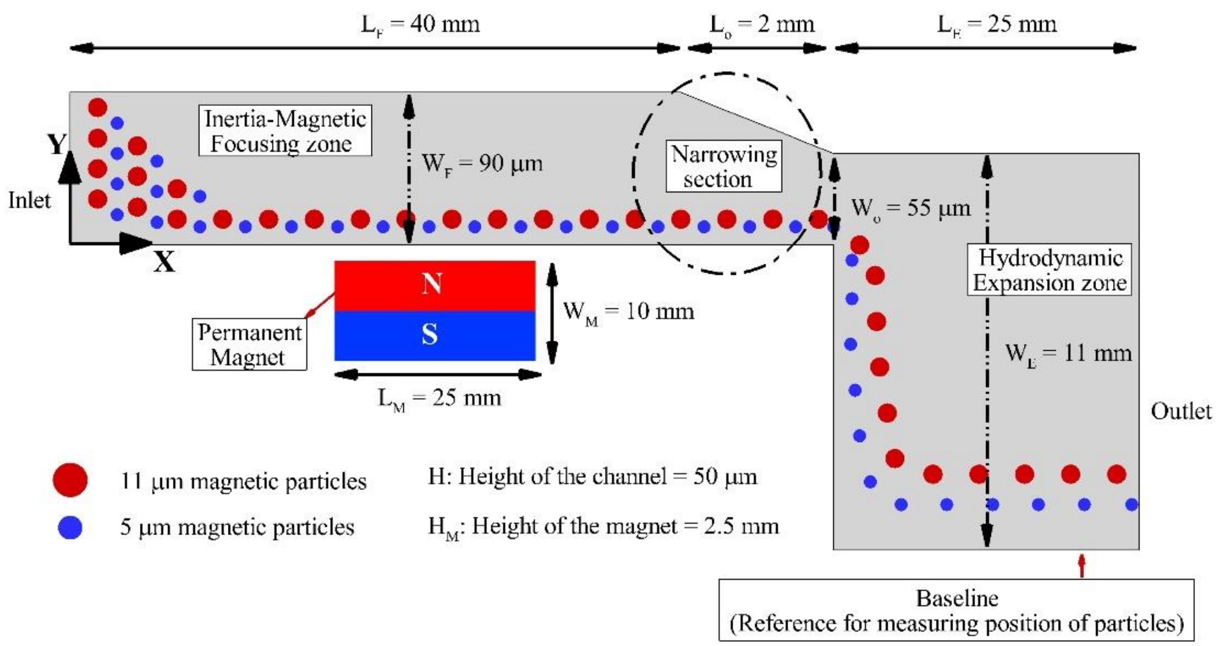

Fig. 2-1. Schematic diagram of the modeled microfluidic device (first introduced by Kumar and Rezai [21]*) which consisted of an upstream inertia-magnetic focusing channel with a permanent magnet beside it, a narrowing section at the center, and a downstream hydrodynamic expansion zone and fractionation channel. The figure also shows the sizes of particles and channel sections as well as the working principle of the device. Particle positions reported in this paper are all based on the expansion zone's bottom channel baseline. Permission obtained from Microfluidics and Nanofluidics.*

2.1.1.2 Elastic and Inertial Particle Focusing in Shear-Thinning non-Newtonian Fluids (Elasto-Inertial Regime)

As per the 2nd thesis objective, we modified the numerical model for Newtonian fluids in objective 1 to capture the non-Newtonian effects of shear-thinning viscoelastic fluids. For this purpose, and in order to validate the model further in the process, we use the experimental work by our group [15] to develop the numerical scheme. The studied straight channel geometry and the interplay of significant forces on particle focusing are shown schematically in Fig. 2-2. This device consisted of a straight microchannel of square cross section leading to a 45° symmetric expansion zone for particle imaging. As compared to the previous device in Fig. 2-1, the authors modified their microfluidic device in Fig. 2-2 by 1) removing the middle narrowing section and 2) making the expansion zone symmetric around the channel axis. These design modifications were done to facilitate the downstream imaging of microparticles and allow for possible symmetrical focusing behavior. Since we aimed to develop a numerical model that captures the inertial, magnetic, and viscoelastic effects, we applied the same modifications to our model geometries while performing validation studies.

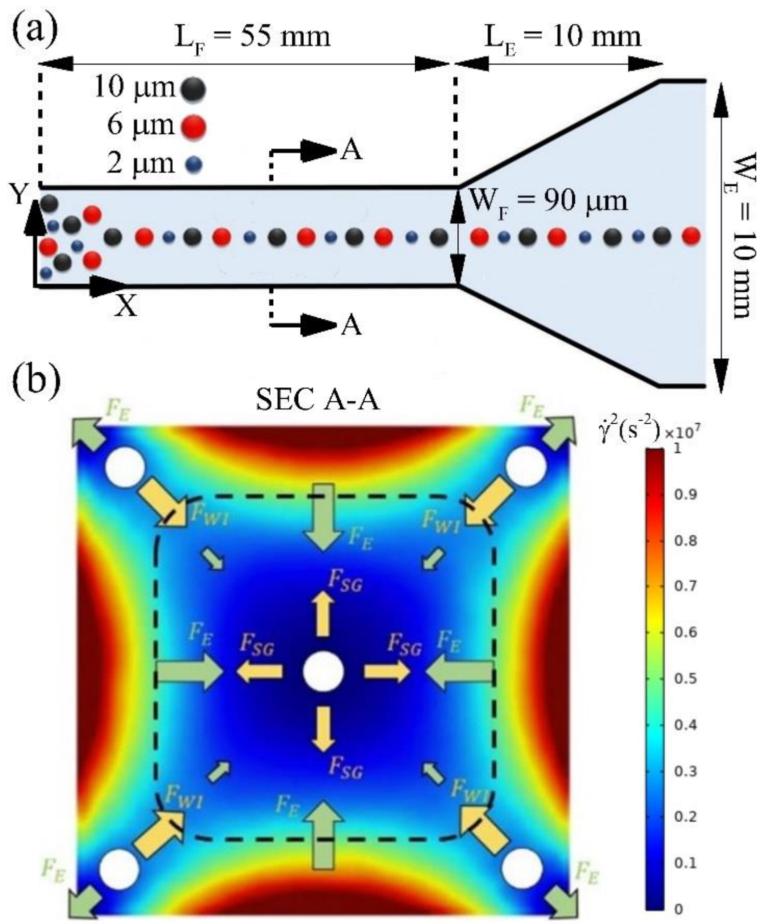

Fig. 2-2. Elasto-inertial particle focusing in a straight microchannel. (a) The studied straight microchannel with a downstream expansion region for velocity drop and observation of microparticles in experiments. The dimensions shown were used for experimental validation. (b) Color contour showing the square of the shear rate, $\dot{\gamma}^2$, in the middle cross section (X = 27.5 mm) of the straight microchannel and the interplay of the elastic lift force (F_E) with the wall (F_{WI}) and shear gradient (F_{SG}) components of the inertial lift force. Permission obtained from Elsevier.

2.1.2 Numerical Model Theory and Working Principles

To achieve a better convergence behavior, the numerical procedure was divided into two stages. First, the steady-state solution of the flow without injecting particles and the applied forces was obtained. Then, particles were injected into the flow where their trajectories were re-calculated based on the applied drag, inertial, magnetic and/or elastic lift forces. The solved equations for each stage are described below.

2.1.2.1 Fluid Flow Simulation in Microchannels

Standard laminar flow steady-state governing equations, i.e., the continuity Eq. (1) and the Navier-Stokes Eq. (2), without introducing the microparticles, were solved in order to find the converged steady-state solution of the flow.

$$\nabla \cdot (\rho \vec{u}) = 0 \tag{1}$$

$$\nabla \cdot (\rho \vec{u}\vec{u}) = -\nabla p + \nabla \cdot (\bar{\bar{\tau}}) + \rho \bar{g} \tag{2}$$

In Eq. (1-2), ρ is density, $\vec{u}$ is fluid velocity, p is static pressure and $\bar{\bar{\tau}}$ is the stress tensor described by Eq. (3).

$$\bar{\bar{\tau}} = \mu \left[(\nabla \vec{u} + \nabla \vec{u}^{T}) - \frac{2}{3} \nabla . \vec{u} I \right] \tag{3}$$

where μ is molecular viscosity, I is the identity tensor, and the second term on the right-hand side is the effect of volume dilation.

Since we tested fluids with different viscosities in this thesis, considering the effect of this parameter was of significant importance in the numerical models. For the case of Newtonian DI water used in the 1st objective of the thesis, the viscosity was set as a constant value at 8.9×10^{-4} Pa·s [141]. However, the fluid viscosity was not constant in our 2nd objective study as shear thinning viscoelastic PEO-water solutions at various PEO concentrations were used. The shear-rate dependent fluid viscosity was modeled based on the Carreau Eq. (4) [142, 143]. This model assumes a Newtonian linear behavior at low and high shear rates, and a power-law viscosity at the intermediate shear rates [15, 144, 145].

$$\frac{\mu - \mu_\infty}{\mu_0 - \mu_\infty} = [1 + (\lambda \dot{\gamma})^2]^{(n-1)/2} \tag{4}$$

where $\dot{\gamma}$ is the shear rate and μ_∞ is the infinite shear viscosity, μ_0 is the zero-shear viscosity, λ is the relaxation time and n is the Carreau index. The values of these parameters depend on the concentration and molecular weight of the PEO added to water, and in this study, they were interpolated from the data available in [142] as provided in Table 2-1, for three PEO concentrations of 2500, 5000 and 10000 ppm at the molecular weight of 400,000 g/mol.

Table 2-1. Carreau model parameters used in the simulation. The molecular weight of the PEO solutions is 4×10^5 *g/mol.*

PEO Concentration (ppm)	μ_∞ **(Pa.s)**	μ_0 **(Pa.s)**	λ **(s)**	**n**
2500 ppm	0.002	0.0021	0.00371	0.5309
5000 ppm	0.003	0.005	0.00311	0.5538
10000 ppm	0.004	0.012	0.00504	0.4978

2.1.2.2 Particle Trajectories Simulation in Microchannels and the Involved Forces

After the flow field was obtained in the first stage of the simulation (section 2.1.2.1), microparticles were injected into the fluid and their trajectories were computed in a Lagrangian reference frame. For each particle, an ordinary differential equation was solved for each component of the position vector.

The trajectory equations were solved by stepwise integration over discrete time steps. Integration of time yields the velocity of the particle at each point along the trajectory, with the trajectory itself predicted by Eq. (5).

$$\frac{dx}{dt} = \vec{u}_p \tag{5}$$

In Eq. (5), x is displacement, t is time and $\vec{u}_p$ is the particle velocity.

At each time step, the forces acting on each particle were queried from the computed fields at the current particle position. The force balance equations on a particle inside water or PEO-water are shown in Eq. (6) or (7) for the 1st and 2nd objectives studies, respectively. The particle position was then updated, and the process was repeated until the specified end time of the simulation.

$$\frac{d\vec{u}_p}{dt} = (\vec{F}_D + \vec{F}_L + \vec{F}_M)/m \tag{6}$$

$$\frac{d\vec{u}_p}{dt} = (\vec{F}_D + \vec{F}_L + \vec{F}_E)/m \tag{7}$$

In Eq. (6), $\vec{F}_D, \vec{F}_L, \vec{F}_M$ and $\vec{F}_E$ are the drag, inertial lift, magnetophoretic and elastic lift forces, respectively. In Eq. (6-7), m is the spherical particle mass.

For the Newtonian DI-Water used in the 1st objective study, since we are working at very low Re numbers (Re < 1), the drag force is defined by Stoke's drag law [146] in Eq. (8).

$$\vec{F}_D = 3\pi\mu d_p \vec{u}_p \tag{8}$$

where d_p is the particle diameter.

For shear thinning viscoelastic fluids, although the Stoke's drag has been used in some previous numerical works [147], the drag force on a particle flowing in such medium has been reported to be different from the Stoke's drag [148]. Therefore, we chose an equation from Bush and Phan-Thien [148] for the drag force in objective 2 that is suitable for the range of our parameters.

$$\vec{F}_D = 3\rho\pi {d_p}^2 {\vec{u}_p}^2 \left(1 + {X_p}^{\frac{2}{(n-1)}} \cdot \frac{\lambda.{U_p}^3}{{d_p}^2}\right)^{(n-1)/2} / Re \tag{9}$$

Eq. (9) parameters depend on the concentration and molecular weight of the PEO solution. Parameter X_p is the drag correction factor [149]. X_p values were interpolated from the data provided by Phan-Thien [148] . For 2500, 5000 and 10000 ppm PEO solutions, the X_p values were determined to be 1.408, 1.399 and 1.421, respectively.

The inertial lift force, $\vec{F}_L$ in Eq. (6) and (7), involves several components which include (i) rotation-, (ii) slip shear-, (iii) shear gradient- and (iv) wall-induced lift forces [63]. Shear gradient (F_{SG}) and wall-induced (F_{WI}) lift forces, as shown in Fig. 2-2b, are the two dominant components of inertial force acting on a particle in a plane Poiseuille flow. Shear gradient-induced lift force pushes the particles away from the centerline of the channel due to the curvature of the velocity profile. Wall-induced lift force repels the particles away from the channel walls due to the pressure difference around the particle caused by the wall-induced decrease in particle velocity. To account for both shear-induced and wall-induced components of the inertial lift, our simulation took advantage of the results from Ho and Leal [150] for their general force equation that describes forces acting on small rigid spheres in low Re numbers using the Lorentz generalized reciprocal theorem. The resulting general lift force Eq. (10) includes the wall-induced and shear-induced lift forces.

$$\vec{F}_L = \frac{1}{m}\rho\frac{{d_p}^4}{16{D_h}^2}\varphi\big(\varphi G_1(s) + \gamma G_2(s)\big)\vec{n} \tag{10}$$

$$\varphi = \left|R(\vec{n}\cdot\nabla)\vec{u}_p\right|$$

$$\gamma = \left|\frac{R^2}{2}(\vec{n}\cdot\nabla)^2\vec{u}_p\right|$$

$$\vec{u}_p = \big(I - (\vec{n}\otimes\vec{n})\big)\vec{u}$$

In Eq. (10), $\vec{n}$ is the wall normal at the nearest point on the reference wall, $\otimes$ symbol represents the tensor product of the $\vec{n}$ vectors, R is the distance between the channel walls, s is the dimensionless distance from the particle to the reference wall, and G_1 and G_2 are dimensionless functions of s as previously reported [150, 151]. The inertial lift force only acts in the direction perpendicular to the velocity of the fluid. The spherical particles were further assumed to be small compared to the channel width and rotationally rigid.

The force acting on a magnetic particle due to a permanent magnet (Fig. 2-1) such as the one used in our experiments [21] and model (Eq. (6)) in this study can be expressed by Eq. (11) [40].

$$\vec{F}_M = \frac{4\pi}{3}M\nabla B{r_p}^3\frac{1}{m_p} \tag{11}$$

where r_p is the radius of the particle ($=d_p/2$), M is magnetization and ∇B is the magnetic field gradient. Based on the data of Kumar and Rezai [21], magnetization and magnetic field gradient were set to $M=2.7\times10^6$ A/m and $\nabla B=10$ T/m for validating our model, respectively. Magnetic field magnitude inside the channel was set to B=300 mT, also based on the reported experimental results.

The elastic lift force, F_E in Eq. (7), develops due to the changes in the normal stress differences in viscoelastic flows [88]. In viscoelastic fluids, both the first ($N_1 = \tau_{xx} - \tau_{yy}$) and second ($N_2 = \tau_{yy} - \tau_{zz}$) normal stresses contribute to particle migration. τ_{xx}, τ_{yy}, and τ_{zz} are normal stresses that are directed toward the flow, the velocity gradient and the vorticity direction, respectively. Normally, the effects of N_2 can be neglected in diluted viscoelastic solutions, because $N_1 \gg N_2$ [152-154] and we can approximate the elastic lift force by only considering the N_1.

The Oldroyd-B model is a special case of the Oldroyd 8-constant model, partially capturing numerous important viscoelastic phenomena but with many fewer parameters and is a popular model among experimentalists and theoreticians [155]. In simple shear cases, the normal stresses in an Oldroyd-B fluid have two time constants ($N_1 = 2\eta_0(\lambda_1 - \lambda_2)\dot{\gamma}^2$). Where λ_1 is the relaxation time and λ_2 is the retardation time. In the case of our viscoelastic PEO-water fluids, $\lambda_2 = 0$ and the Oldroyd-B approximation reduces to the Upper Convective Maxwell (UCM) [155] ($N_1 = 2\eta_0\lambda\dot{\gamma}^2$).

After the flow field is simulated and the shear rate ($\dot{\gamma}$) distribution is obtained, it can be related to the first normal stress (N_1) using an analytical approximation based on the Oldroyd-B constitutive model ($N_1 = -2\eta_p\lambda\dot{\gamma}^2$). This analytical approximation is routinely used in the literature for viscoelastic fluids [89, 153, 156].

The elastic lift force originating from an imbalance in the distribution of N_1 over the size of the particle can be expressed as [156]:

$$\vec{F}_E = C_{eL} d_p{}^3 \nabla N_1 = -2 C_{eL} d_p{}^3 \eta_p \lambda \nabla \dot{\gamma}^2 \tag{12}$$

In Eq. (12), C_{eL} is a non-dimensional elastic lift coefficient taken to be 0.05 [147] in our simulations, η_p is the part of the solution viscosity that can be related to the polymeric contribution, λ is the fluid relaxation time, and $\dot{\gamma}_c$ is the shear rate.

Capillary Breakup Extension Rheometry (CaBER) measurement is used to determine the λ value of the PEO solutions, resulting in $\lambda = 18\lambda_z (c/c^*)^{0.65}$ [157]. The overlapping concentration c^* is expressed as $0.77/[\eta]$ [158], where the intrinsic viscosity $[\eta]$ is given by the Mark-Houwink relation, $[\eta] = 0.072 M_w{}^{0.65}$ [159]. The Zimm relaxation time is determined as $\lambda_z = F[\eta] M_w \eta_s / N_A k_B T$ according to Zimm theory. Here, the pre-factor F is 0.463 for PEO solutions, η_s is the solvent viscosity, and N_A and k_B are Avogadro's number and Boltzmann's constant, respectively.

2.1.3 Boundary Conditions and Solver Settings

The boundary conditions of the microfluidic devices shown in Fig. 2-1 and Fig. 2-2 were set in our model to provide the closest approximation to the experimental conditions. A uniform velocity profile was imposed at the inlet in the x direction described with $u = U_{inlet}$. The transverse fluid velocities in the y and z directions were both assumed to be zero ($v = w = 0$). The non-slip boundary condition was applied on the device walls and formulated with $u = v = w = 0$. At the outlet, a constant pressure boundary condition with zero-gauge static pressure was assumed ($p_{outlet} = 0$).

At each time step taken by the solver, the forces acting on each particle were queried at the current particle position. Due to the very low volume fraction of particles ($\varphi << 1$ v/v %), particle-

particle interaction forces were neglected in the model. Channel walls were assumed to be rigid, and the “bounce” condition was assumed for the particles hitting the walls. Flow velocity and particle concentration were monitored as benchmark parameters to check for convergence.

Solver settings for the inertia-magnetic focusing in Newtonian fluid (Objective 1) and elasto-inertial focusing in shear-thinning viscoelastic fluid (Objective 2) are explained below in sections 2.2.4.1 and 2.2.4.2, respectively.

2.1.3.1. Solver Settings for Inertial and Magnetic Particle Focusing Regimes

ANSYS-Fluent DPM (Discrete-Phase-Modeling) scheme was employed to inject microparticles into the DI-Water and compute their trajectories in a Lagrangian reference frame. To be consistent with the experimental work, the particle to water mixture concentration was approximately 1.1×10^{7} particles/mL. A User-Defined-Function (UDF) code in C language was written and incorporated into the conventional DPM model to account for the inertial lift force (wall- and shear gradient-induced) and the prescribed magnetic field and the applied magnetophoretic force on the microparticles to recalculate their final trajectories. The equations were discretized and solved utilizing the SIMPLEC (semi-implicit method for pressure linked equation consisted) algorithm. Two-way coupling was assumed between the fluid flow and the particles trajectories by which the impacts of the fluid flow on the trajectory of the particles and vice versa were considered. This was accomplished by alternately solving the discrete and continuous phase equations until the solutions in both phases converged. For all the simulation cases, solutions became stabilized when residuals dropped below the prescribed value of 10^{-9}.

2.1.3.2. Solver Settings for Elastic and Inertial Particle Focusing Regimes

As mentioned earlier (section 2.1.2.1), we are using Carreau equation (Eq. 4) to model the viscoelastic solution. This equation along with the inertial lift equations (Eq. 10) are built-in models within COMSOL-Multiphysics commercial package. Therefore, for our 2nd objective, COMSOL-Multiphysics particle tracing module was employed to inject microparticles into the shear-thinning viscoelastic solution and compute their trajectories in a Lagrangian reference frame. Particles were randomly injected into the flow field from the inlet with the concentration of 2×10^5 particles/ml to match the experimental conditions in [15]. The fluid flow equations were solved utilizing the direct MUMPS (MUltifrontal Massively Parallel Sparse direct Solver) method. For the particle simulation, the iterative GMRES (Generalized Minimal RESidual) method was adopted with respective residual and relative tolerances of 10^{-3} and 10^{-6}, respectively.

2.2 Experimental Procedure

This section describes sample preparation, device fabrication and experimental procedure that were used as per our third objective defined in section 1.3, i.e. investigation on microparticle behavior in shear thickening SiO_2-water fluids.

2.2.1 Sample Preparation

A concentrated (40% wt.) aqueous solution of 20 nm SiO_2 nanoparticles were acquired from Alfa Aesar Germany. The batch nanofluids were diluted and prepared in volume concentrations of 1, 2 and 3%. The resulting suspensions were subjected to ultrasonic vibration for about 30 min to ensure that a uniform nanoparticle dispersion was obtained. It should be noted that the NF suspensions were found to be very stable, even after a relatively long resting period. Our experiments were performed using microparticles with the diameter of 5 μm (CM-50-10, 5-5.9

μm), 10 μm (CM-80-10, 8-9.9 μm) and 15 μm (CM-150-10, 14-17.9 μm) from Spherotech Inc., USA. The ratio of microparticle solution and SiO_2/water nanofluid solution were chosen in a way to obtain ~2×10^5 micro particles/mL of nanofluid in each experiment.

2.2.2 Microfluidic Device Design and Fabrication

The microfluidic device shown schematically in Fig. 2-2 was microfabricated from polydimethylsiloxane (PDMS) as shown in Fig. 2-3 a-b. It consisted of an inlet, a straight 55 mm long square cross-section microchannel, and a symmetric expansion zone (45° transition angle and 10 mm length).

The device layouts were designed in the SolidWorks software and printed on photomasks by CAD/Art Services, Inc., OR, USA. The device master molds were fabricated using photolithography. SU-8 2075 photoresist (Microchem Corp., MA, USA) was spun on silicon wafers with the diameter of 4 inches (Wafer World Inc., FL, USA) using a spin coater (200DBX Develop-Bake System, Brewer Science, Cost Effective Equipment, MO, USA). Then, the molds were pre-baked on hot plates at 65°C and 95°C based on Microchem's SU8 data sheet. SU8 coated wafers were exposed to UV light (UV KUB 2, Kloé, Montpellier, FR) through the photomasks. After post baking the UV-exposed molds at 65°C and 95°C, they were washed with SU-8 developer to dissolve the unexposed SU-8 on the silicon wafers. The molds were finally hard baked at 200°C for 20 minutes.

The molds were then used to fabricate the microfluidic devices using soft-lithography [160]. PDMS (Dow Corning Sylgard 184 Silicone, Ellsworth Adhesives, ON, Canada) was mixed at 1:10 ratio of base to curing agent and poured over the SU-8 molds with inlet and outlet tubes installed in place on top of channel reservoirs. The PDMS prepolymer was cured at 100°C for 1 hour, then peeled off the mold and bonded to a glass slide (Brain Research Laboratories, MA, USA) using an oxygen plasma machine (Harrick Plasma, PDC-001, NY, USA).

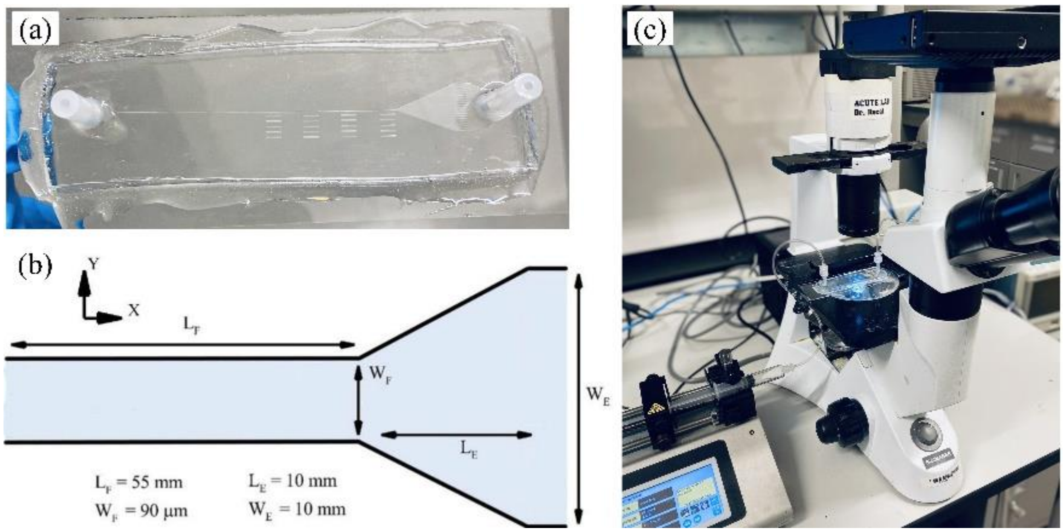

Fig. 2-3. Straight channel microfluidic device(a) and dimensions of the device used in the microfluidic shear-thickening experiments (b). Experimental setup (c).

2.2.3 Experimental Setup

The experimental setup, shown in Fig. 2-3c, consisted of one of the straight microfluidic devices tested under an inverted fluorescent microscope (BIM500FL, Bioimager, ON, Canada) equipped with a high-speed camera (Fastec IL3, Canada). Singleplex samples (meaning one microparticle type at a time) of suspended microparticles inside SiO_2-water nanofluid solutions were prepared and flown into the device at various flow rates of 1.0-20 mL/hr using a syringe pump (KD Scientific Inc., MA).

2.2.4 Data Analysis and particle counting

Up to 1300 image frames were obtained by the camera on the microscope per experimental condition. Afterwards. they were overlapped using the open-source ImageJ software, as shown in Fig. 2-4a and 2-4c for 10 µm particles in water and 2.0% v/v SiO_2, inside the device. An in-house image processing code was developed in Python (See Appendix A) to count the number and position of particles in a narrow vertical slice in each frame. This slice was chosen at a distance of ~1000 µm from the start of the expansion zone (Fig. 2-4c) and its width was calculated based on the flow velocity so that the particles that entered the camera's field of view were counted only once. The normalized (using the channel width) distribution of particles throughout the expansion zone width were then plotted as in Fig. 2-4b and 2-4d. To find the center point of the deflected particle stream and the dispersion of particles, fractions of focused particles were analyzed, by fitting a Gaussian curve onto the distribution of particles (Fig. 2-4d). The peak position of the fitted curve showed the position of the focused particles in the channel and the diagram's full width at half maximum (FWHM) was used to represent the distribution of the focused particles, or the particles' dispersion [5]. For consistency and ensuring the repeatability of results, the experiments were repeated 3 times.

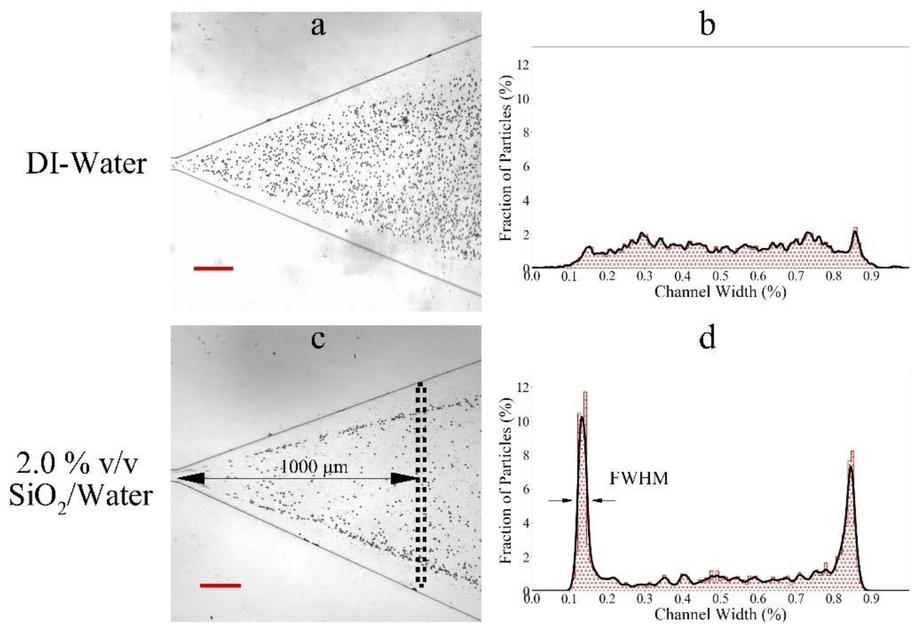

Figure 2-4 Overlapped images (up to 1300 frames) of 10 µm particles at 1 mL/hr flow rate flowing in (a) water and (c) 2.0 % v/v SiO_2/Water in the device shown in Fig. 2-3. The fitted Gaussian distribution curve shown in (b) and (d) with full width at half maximum (FWHM) used as a measure for particle dispersion (scale bars = 200 µm).

Chapter 3
RESULTS AND DISCUSSION

The numerical models described in Chapter 2 were used to study microparticle hydrodynamics in straight microchannels, in three focusing regimes as defined by thesis objectives (section 1.3). As we have developed numerical models to address the first two objectives, the results of the previous experimental investigations [15, 21] conducted in our group was used to validate the numerical models.

For objective 1, inertial focusing of microparticles was numerically studied in a Newtonian fluid, with consideration of the effect of a magnetic force pulling the particles towards the sidewall of the microchannel, termed inertia-magnetic focusing (section 3.1). The model was verified and validated against our experimental findings [21]. Then, a parametric numerical study was performed to investigate the unknown effects of multiple significant parameters on inertia-magnetic focusing of microparticles in straight channels.

For objective 2, in section 3.2, we expanded our Newtonian numerical scheme in section 3.1 to include the shear-thinning effects of viscoelastic non-Newtonian fluids. After verification and validation of the model against another experimental work in our lab [15], a parametrical study was conducted, and a new design criterion was proposed for elasto-inertial particle focusing in straight microchannels.

For objective 3, in section 3.3, the microfluidic device that was tested with the Newtonian and shear-thinning non-Newtonian fluids in section 3.2 was used to investigate particle behavior in shear-thickening non-Newtonian fluids. The experimental results were quantified and characterized using our python code and the effects of significant parameters were investigated.

3.1 Microparticle Focusing in Newtonian Fluids**

This section describes the verification, validation and parametrical study that was conducted on inertial and inertia-magnetic focusing of microparticles suspended in Newtonian fluids within straight microchannels, using the developed inertia-magnetic model (section 2.1) to address the first objective (section 1.3) of the thesis. We first verified our model by investigating its mesh independency and fluid flow characteristics (section 3.1.1), then validated the model against the experimental results of Kumar and Rezai [21] in which a similar device was utilized (section 3.1.2). Lastly, we used our validated model to investigate the unknown effects of magnetization ($0\text{-}2.7\times10^6$ A/m), microparticle size (0-30 µm), and fluid viscosity (0.5-1.5 mPa.s) on inertia-magnetic focusing and sorting of microparticles in straight microchannels (section 3.1.3).

3.1.1 Model Verification

3.1.1.1 Mesh Independency Study

The device geometry in Fig. 3-1a was meshed with hexahedral cells with regular connectivity (Fig. 3-1b). As a reminder, the straight channel width, height, and length were 90µm, 50µm, and 42 mm respectively, to be aligned with the experimental work used later for model validation. The narrow inertia-magnetic focusing and the expanded hydrodynamic fractionation microchannel cross sections had 45 and 25 grid points in the vertical and horizontal directions, respectively. The mesh was more refined near the microchannel walls and the entrance of the expansion zone to accurately capture the flow fluctuations around these areas.

** The results of section 3.1 are published in 139. Moghadam, M.C., A. Eilaghi, and P. Rezai, *Inertia-magnetic particle sorting in microfluidic devices: a numerical parametric investigation.* Microfluidics and Nanofluidics, 2019. **23**(12): p. 135.

In order to ensure mesh independency of our simulations, while minimizing the computational costs, several mesh sizes (i.e., number of mesh elements) in the range of 5.7×10^4 to 1.1×10^6 elements were considered. Based on our initial investigations using water as the carrying fluid in the microchannel, we found that larger flow fluctuations occur at the centerline of the inertia-magnetic focusing microchannel, especially as the flow enters the expansion zone, due to the difference between the cross-section sizes. Therefore, the magnitude of axial velocity along the microchannel centerline and the axial velocity profile on the cross section of the expansion zone entrance were plotted in Fig. 3-1c and 1d, respectively, for different mesh sizes in the case of DI-water flowing at 1 mL/hr in the microchannel.

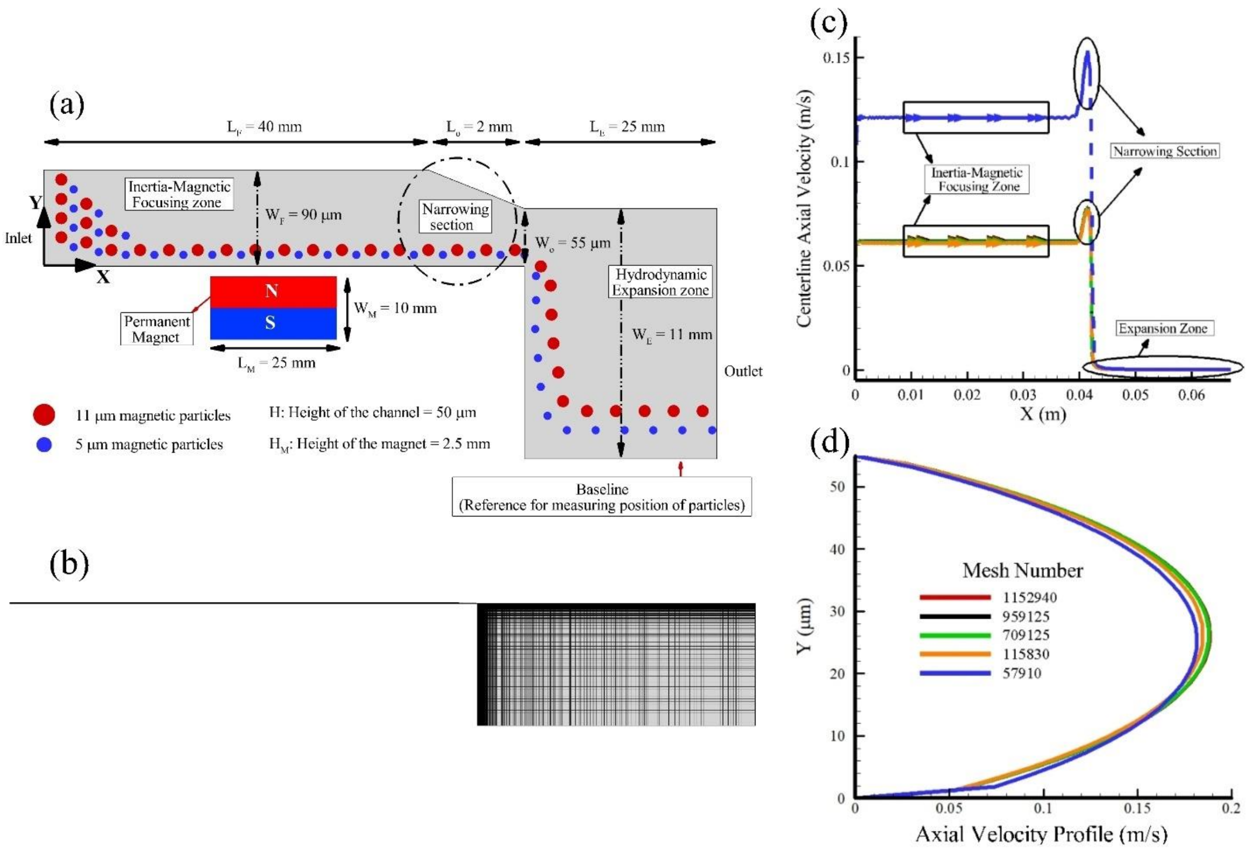

Fig. 3-1. (a) The straight microchannel device geometry and (b) its computational grid. Numerical simulation of DI-water flowing at 1 mL/hr in the straight microchannel for various mesh sizes. (c) Axial velocity magnitude along the centerline of the microchannel. (d) Axial velocity profile on the entrance cross section of the expansion zone.

As shown in Fig. 3-1c, the centerline velocity is expectedly constant in the inertia-magnetic focusing and the expanded channel regions, while the largest velocity fluctuations along the centerline of the microchannel occur before the expansion zone where the microchannel narrows down and the centerline velocity spikes due to the decrease of channel cross section. The axial velocity profile on the entrance cross section of the expansion zone is presented in Fig 3-1d showing an expected parabolic profile. As seen in Fig. 3-1c and 1d, increasing the number of mesh elements to more than 959125 had a negligible impact of less than 0.01% on the centerline velocity and the axial velocity profile and the flow became independent from the mesh. Therefore, this computational mesh size was chosen for our simulations.

3.1.1.2 Fluid Flow Study

We continued our verification studies by modeling the fluid velocity contours around the expansion zone entrance region without the presence of magnetic particles and the magnetic field at a flow rate of Q=3 mL/hr (Fig. 3-2).

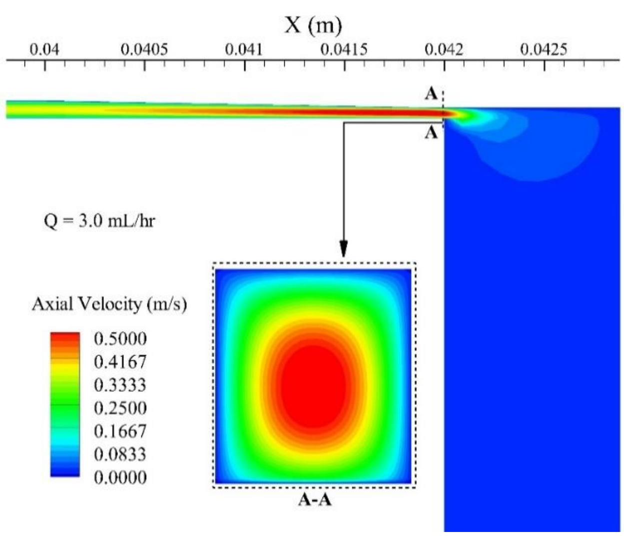

Fig. 3-2. Axial velocity contours at a flow rate of Q=3mL/hr in the straight microchannel, shown around the expansion zone entrance and at its cross section.

As shown in Fig. 3-2, the flow velocity reaches a maximum local magnitude at the middle of the expansion zone entrance, due to the change of cross section of the microchannel just before the expansion region. Across the cross section of the microchannel, the flow velocity is not constant, owing to the effect of viscosity. No-slip condition at the walls causes the fluid particles to become stationary while the axial velocity increases symmetrically towards the center of the microchannel, ultimately resulting in a horseshoe-shaped parabolic velocity profile, with minimum velocity at the walls and maximum velocity at the center of the channel like a Poiseuille flow [161]. With the model being verified above for predicting the velocity profile of the Newtonian DI-Water in the microchannel, we could move on to injecting the microparticles in the next step and validating the model against the experiments in [21].

3.1.2 Model Validation

After the model was verified in section 3.1.1, we validated its performance for predicting particle trajectories against our previously published experimental results [21].

3.1.2.1. Inertial and Magnetic Focusing of Magnetic Microparticles

The capability of our model in predicting the microparticle trajectories both with and without the presence of a magnet in the straight microchannel was investigated. For this, distribution of 11μm magnetic microparticles at different flow rates were investigated around the expansion zone of the device and compared to the results of Kumar and Rezai [21] in Fig. 3-3.

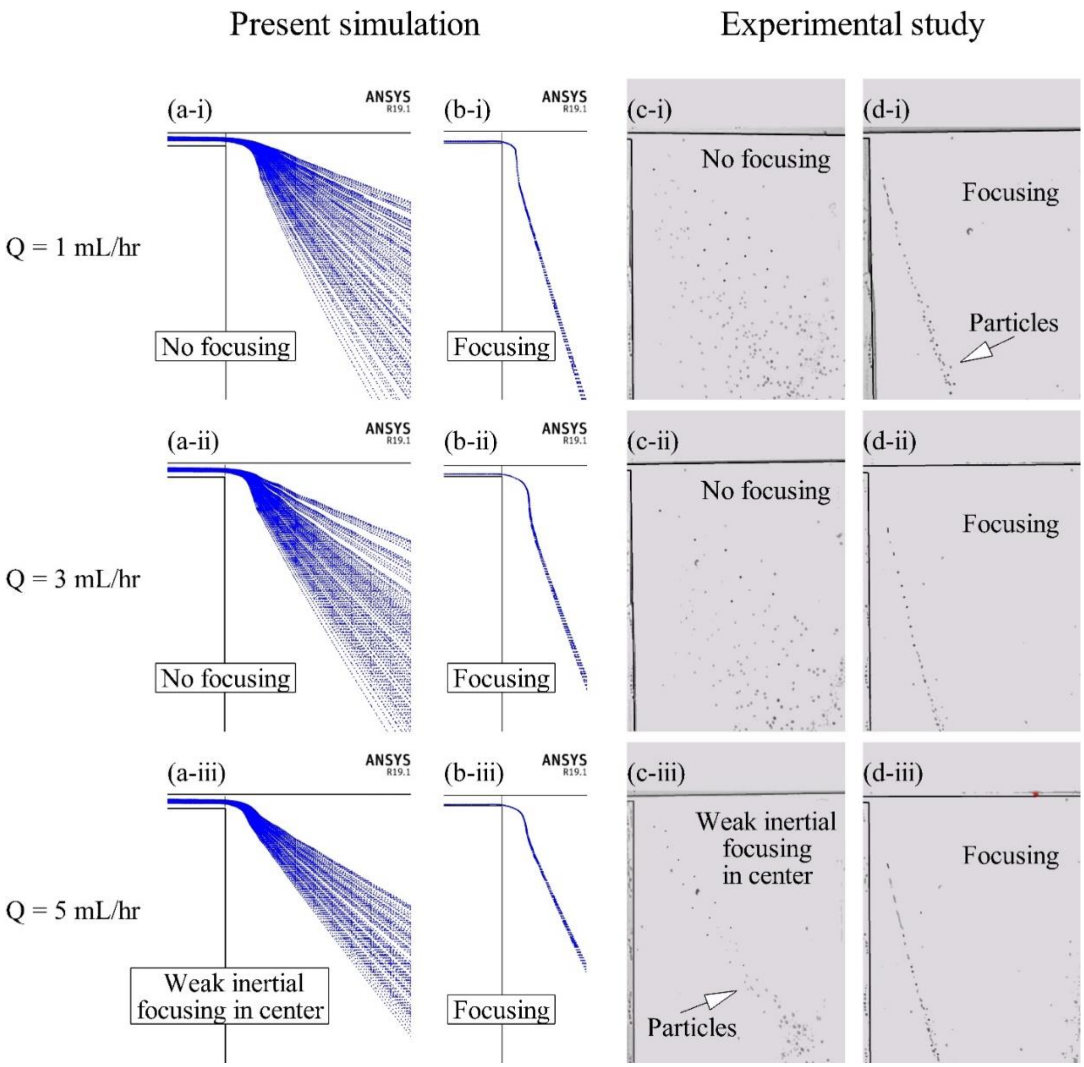

Fig. 3-3. Distribution of 11µm magnetic microparticles at different flow rates around the expansion zone of the straight microchannel, for the cases of numerical simulation (a) without and (b) with magnetic focusing, as well as experimental results (c) without and (d) with magnetic focusing. Experimental figures were reproduced based on the work of Kumar and Rezai [21], with the permission from Springer Nature.

For all the flow rates, 11 µm magnetic microparticles were found to be randomly distributed in the channel without the magnetic field in our model (Fig. 3-3a). However, when we introduced the magnetic field (Fig. 3-3b), microparticles were found to be magnetically focused at the side-wall of the focusing region and deflected as a narrow particle band into the expansion region. These results match with the experimental results of Kumar and Rezai [21]. Moreover, as shown in Fig. 3-3a with no magnetic focusing, microparticles focused weakly in the expansion region as the flow rate was increased from 1 to 5 mL/hr. This observation, which is experimentally supported, can be attributed to the inertial forces acting on the magnetic microparticles that are more pronounced at higher flow rates [64, 162, 163].

3.1.2.2 Effect of Magnetic Focusing on the Exit Position of Microparticles

Further model validation attempts were made quantitatively by investigating the exit position of magnetic microparticles with and without modeling the magnetic focusing effect. The fraction of particles (*f*) were calculated at the exit region of the device, with respect to the bottom sidewall of the expansion channel (i.e. baseline in Fig. 2-1 and 3-1a), for the 11 µm magnetic microparticles flowing at 3 mL/hr. Results were compared with the experimental data [21] in Fig. 3-4.

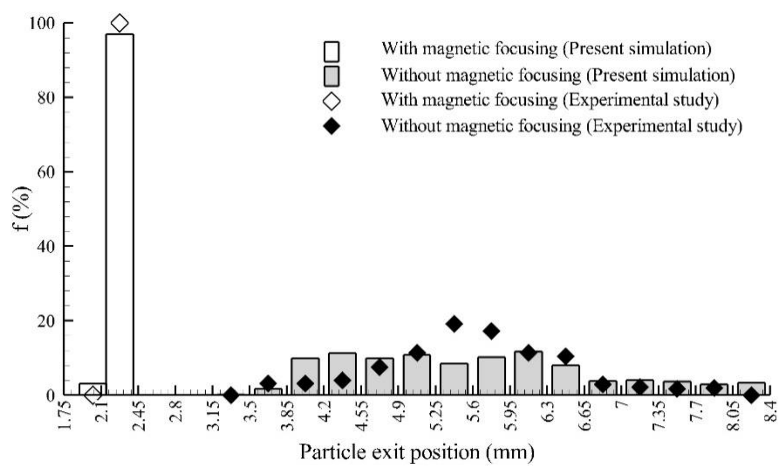

Fig. 3-4. Comparison of the experimental [21] and numerical exit positions (at the device outlet) of 11µm magnetic microparticles flowing at 3 mL/hr in the straight microchannel.

As shown experimentally [21] in Fig. 3-4, without magnetic focusing the particles were randomly dispersed along a wide range of the outlet, 3.5–8.4mm away from the sidewall. However, magnetically-focused particles fell within a narrower range of the outlet concentrating at 2.0–2.4mm from the sidewall. Numerical simulations predicted the exit position of microparticles to be 1.98–2.42mm and 3.42–8.33mm from the sidewall, for the cases with and without magnetic focusing, respectively. The numerical simulation for both cases found particles to be distributed approximately 0.05mm wider than the experiments. The discrepancy between the numerical simulation and the experiments was greater for the fraction of particles, especially for the case without magnetic focusing in the mid-range of 5.25–5.95 mm. Maximum discrepancy was found to be around 10% within the range of 5.25–5.6mm. Considering the fact that the overall distribution range of focused and dispersed particles was captured acceptably by the model, the 10% maximum mismatch for a specific range was deemed acceptable, so we concluded that the model can predict particle trajectories with reasonable accuracy.

3.1.2.3 Effect of Flow Rate on Inertia-Magnetic Focusing of Microparticles

We also investigated the effect of flow rate on the exit position of 11μm magnetic microparticles at the device outlet, and validated our numerical simulation with the experimental measurements [21]. Particles' exit position flowing at different flow rates in the presence of magnetic field are displayed along the outlet in Fig. 3-5, for both the present simulation and the experimental cases.

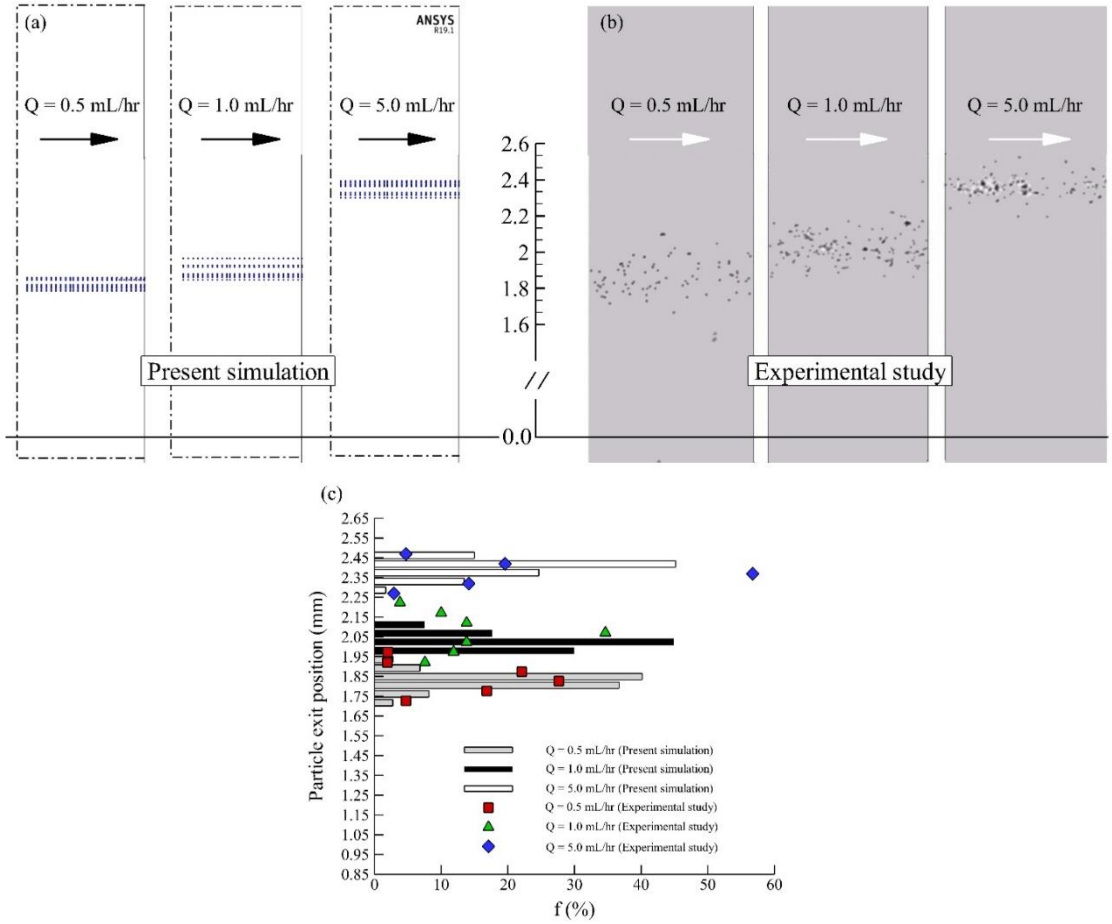

Fig. 3-5. Effect of flow rate on exit position of magnetically focused 11µm microparticles in the straight microchannel. (a) Present simulation. (b) Experimental study [21] with permission from Springer Nature. (c) Exit position of magnetically focused 11µm particles demonstrating both the numerical and experimental results.

As shown in Fig. 3-5, the particles were deflected further away from the channel sidewall with increasing the flow rate. The focusing zone ranges in the simulations were 1.72–1.98, 1.98–2.11, and 2.29–2.46mm for the flow rates of 0.5, 1, and 5mL/hr, respectively. In experiments [21], these ranges were 1.73–1.97, 1.92–2.22, and 2.27–2.47mm for 0.5, 1, and 5mL/hr flow rates, respectively. These findings indicate that the numerically predicted exit positions of the particles correspond well with the experimental data [21] with a mismatch of less than 5%. This increase in particle deflection with increase in the flow rate can be attributed to the inertial lift force acting against the magnetic force. For particle Reynolds number, Re_p, larger than one, inertial lift force becomes more important and microfluidics inertial focusing will be realized [64, 163]. In our case, for the flow rate of 5mL/hr ($Re_{p,11}$ = 1.12), inertial force becomes significant but not enough to dominate the magnetic focusing at the sidewall. The particles were still mainly pulled towards the sidewall at this flow rate while being deflected approximately 5% of the width of the expansion zone towards the channel center.

3.1.2.4. Duplex Inertia-Magnetic Fractionation of Microparticles

For final step of model validation, inertia-magnetic fractionation of two microparticles with different sizes was investigated. These numerical results are compared against the experimental measurements for the mixture of 5μm and 11μm magnetic microparticles flowing at 5mL/hr in the channel as shown in Fig. 3-6.

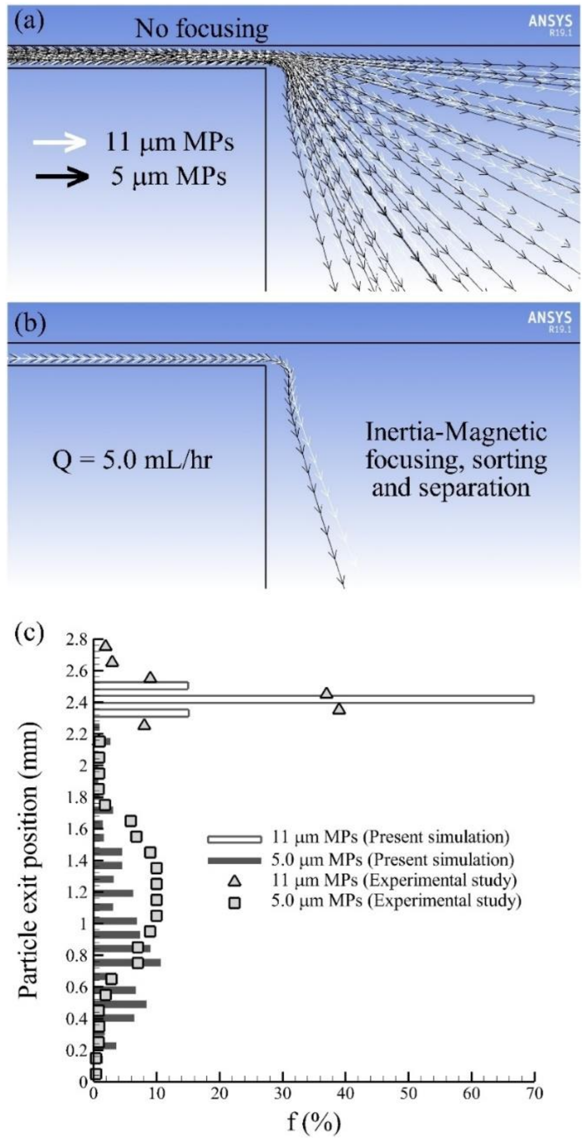

Fig. 3-6. Distribution of 5 and 11μm magnetic particles flowing at 5mL/hr in the straight microchannel considering the effects of inertia-magnetic sorting for the cases of (a) without the magnet and (b) with the magnet at the entrance to the expansion region. (c) Magnetically focused particles exit positions at the outlet of the device featuring both the numerical and experimental results.

As shown in Fig. 3-6a, without introducing the magnetic force, microparticles of both sizes enter the expansion zone region completely dispersed and randomly distributed throughout a wide range of the channel. In contrast, when we repeated the simulation under the same condition except with introducing the magnetic field (Fig. 3-6b), we observed the streams of magnetically focused microparticles to be separated based on their difference in size. The spatial fraction distribution of particles at the outlet is shown in Fig. 3-6c. It was found that 5μm and 11μm particles were distributed within the range of 0.10–2.20mm and 2.29–2.46mm away from the baseline, respectively, while in the experiments [21], these ranges were found to be 0.05–2.15mm (for 5μm) and 2.15–2.75mm (for 11μm).

Despite imposing the same throughput at the inlet as that of the experiment, in order to assess if the same number of particles exit the domain after the simulation, we recalculated the rate of particles per second at the outlet to report the possible inconsistencies due to particles loss or accumulation in the domain. The simulation results predicted a fractionation efficiency and particle throughput of 100% and 1.38×10^4 particles/s at the outlet, respectively, while these parameters were reported to be 98% and 1.30×10^4 particles/s in the experiments [21]. Again, an acceptable agreement is observed with the errors of 2% and 6% for the fractionation efficiency and throughput, respectively.

The results in this section showed that the model could predict the behavior of microparticles in Newtonian DI-Water in a straight microchannel. Therefore, we proceeded further with this model to investigate the unknown effects of other parameters on inertial and magnetic focusing in the following sections.

3.1.3 Parametric Numerical Study

3.1.3.1 Further Investigation of Duplex Inertia-Magnetic Fractionation

To expand the discussions on the results of section 3.1.2, the impacts of inertial lift and magnetic forces as well as the channel narrowing section on particle fractionation are visually presented here. Initially, we analyzed cross-sectional particle trajectories along the channel length for two flow rates in Fig. 3-7.

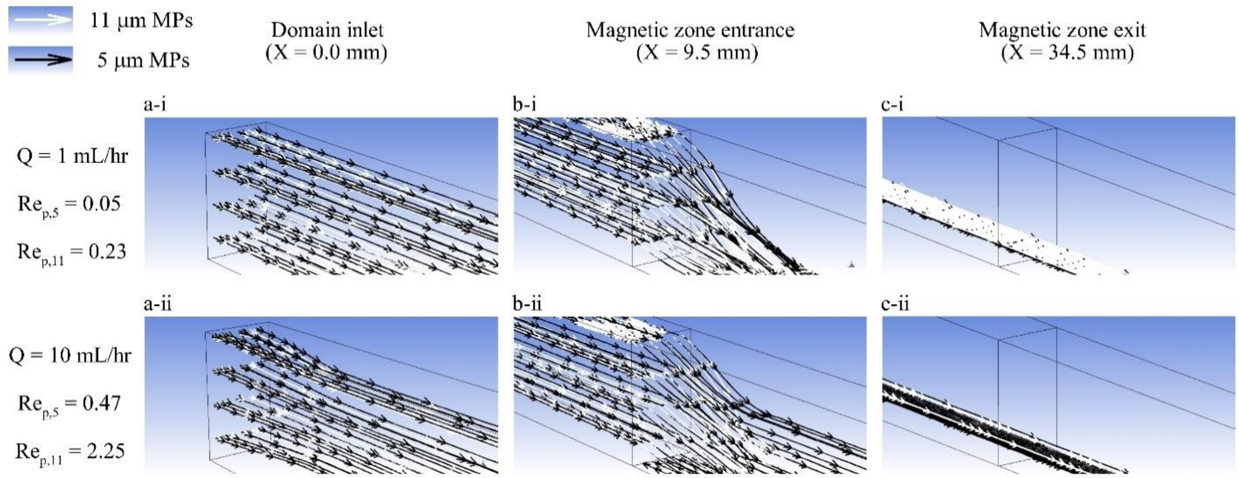

Fig. 3-7. Particle trajectories of 5µm and 11µm magnetic microparticles flowing at different flow rates near the (a) Domain inlet, (b) Magnetic zone entrance and (c) Magnetic zone exit.

As shown in Fig. 3-7a, particles are randomly injected into the domain and move along the length of the channel. At 10 mL/hr (Fig. 3-7a-ii), soon after injection, particles start to migrate away from the side walls to the center of the channel as inertial lift forces are more dominant at this flow rate. As expected, particle trajectories are deflected towards the bottom side of the channel as soon as they enter the magnetic zone (Fig. 3-7b). But this deflection is different for different flow rates and particle sizes. Based on Fig. 3-7b, 11µm particles are quicker to migrate to the bottom side of the channel compared with the 5 µm ones. Also, at 1 mL/hr (Fig. 3-7b-i), particles migration to the bottom side is quicker than the 10 mL/hr as the inertial lift and the drag forces which depend on particle velocity are less pronounced at lower flow rates to resist the magnetophoretic force. At the magnetic zone exit (Fig. 3-7c), particles are fully focused at the bottom side of the channel, while at 10 mL/hr, 11 µm particles focus at two inertial equilibrium positions at 22 µm away from the centerline of the channel.

As hypothesized by Kumar and Rezai [21], by increasing the flow rate, the effect of inertial force becomes more dominant on large particles (also shown in Fig. 3-7c). Moreover, because of the 3D paraboloid nature of the velocity profile in a rectangular cross-section, it was claimed that the

11μm magnetic particles would follow symmetric streamlines while the 5μm magnetic particles would lie on various ones. Consequently, 5μm magnetic particles become distributed over a larger region compared to 11μm magnetic particles, as shown by us in Fig.3-7c.

To investigate the potentially significant effect of inertial lift and study its impact on focusing and separation of particles, we simulated the 3D distribution of 5μm and 11μm particles at different flow rates around the expansion zone entrance of the device (Fig. 3-8) considering the effects of the magnet and the narrowing section right before the expansion region (shown by L_o = 2mm and W_o = 55μm in Fig. 2-1).

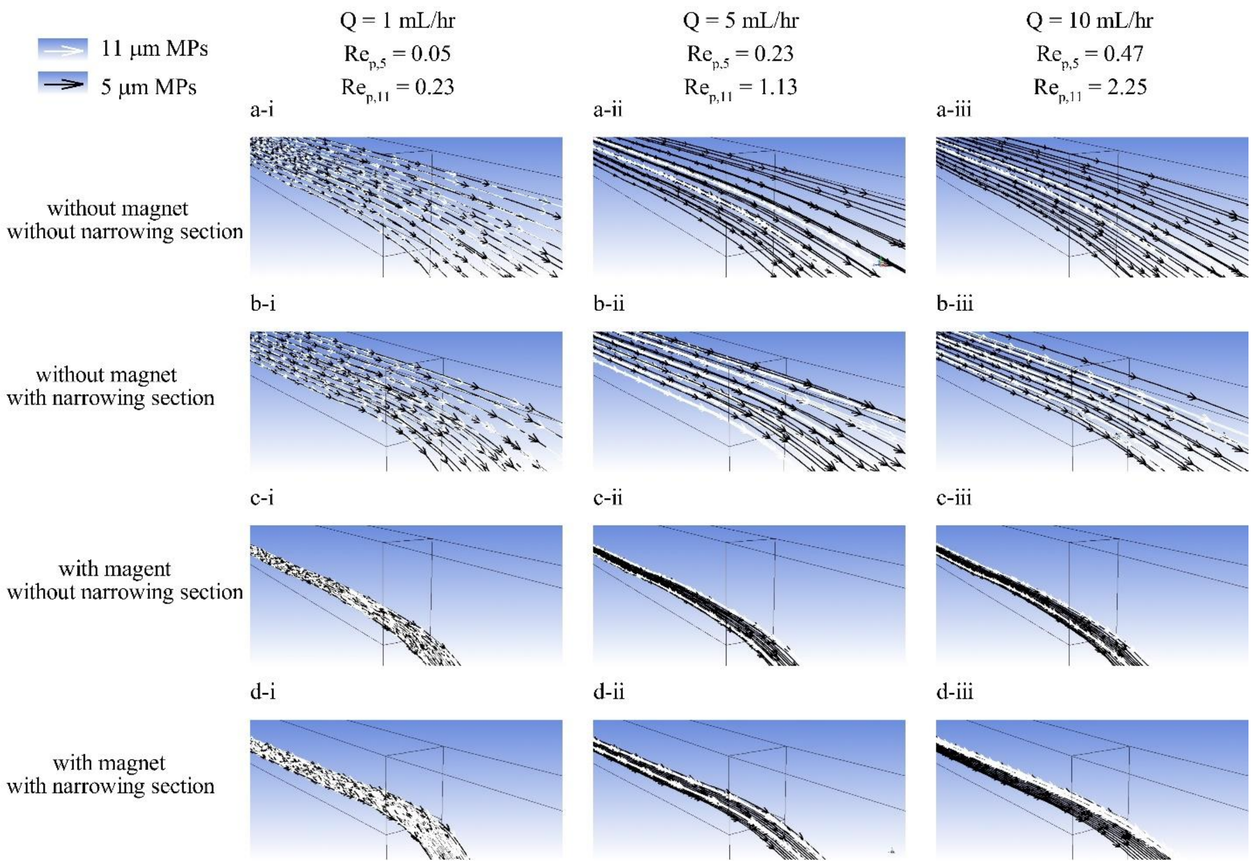

Fig. 3-8. Distribution of 5μm and 11μm magnetic microparticles flowing at different flow rates near the expansion zone entrance of the device, for the cases of (a) without magnet and narrowing section, (b) without magnet and with narrowing section, (c) with magnet and without narrowing section, and (d) with magnet and narrowing section.

Microparticles flowing in rectangular microchannels migrate to two equilibrium positions along the larger side of the channel due to the shear and wall induced lift forces [5, 63, 164], provided that the particle Reynolds number exceeds unity. As shown in Fig. 3-8a-d, for all the studied flow rates of 1–10mL/hr, 5µm particles have particle Reynolds numbers lower than one ($0.05 \leq Re_{p,5} \leq 0.47$). Expectedly, no significant inertial focusing is observed for these particles in any of the investigated cases. Without the magnet (Fig. 3-8a and 3-8b), 5µm particles are dispersed throughout the channel while adding the magnet (Fig. 3-8c and 3-8d) results in their magnetic focusing on a plane against the channel wall close to the external magnet. This multi-streamline focusing explains why 5µm particles were found to be distributed over a wider range of the outlet in both simulation and experimental data in Fig. 3-8c, proving Kumar and Rezai's hypothesis to be correct [21].

For 11µm particles, Reynolds number exceeds unity and becomes $Re_{p,11} = 1.13$ and $Re_{p,11} = 2.25$ at 5mL/hr and 10mL/hr flow rates, respectively. In Fig. 3-8a, without both the magnet and the narrowing section in the setup, 11µm particles were focused at the center of the two largest sides and approximately 20µm and 22 µm away from the centerline of the channel at 5mL/hr and 10mL/hr flow rates, respectively. When we added the narrowing section in the setup in Fig. 3-8b, making the end cross section almost square shape, we observed particles migrating to all four sides of the square cross section but not fully focus at their center points. This can be explained by the short length of the narrowing section ($L_o = 2$ mm) that might not allow for full focusing considering the low particle Reynolds numbers. With introducing the magnetophoretic force in the setup in Fig. 3-8c, particles moved to the bottom side of the channel while 11µm particles still remained inertially focused at two equilibrium positions and approximately 20µm and 22µm away from the centerline of the channel at 5mL/hr and 10mL/hr flow rates, respectively. Adding the narrowing section at the end (Fig. 3-8d) caused the 11μm particles to move away from the sidewalls and focus more at the center of the channel especially for the higher flow rate of 10mL/hr. In this case, 11μm particles focused at 15μm and 9μm away from the centerline of the square shape cross section at 5mL/hr and 10mL/hr flow rates, respectively.

Furthermore, comparing particle trajectories at two different locations of magnetic zone exit (Fig. 3-7c-i and 3-7c-ii) and expansion zone entrance (Fig. 3-8c-i, 3-8d-i, 3-8c-iii and 3-8d-iii), a slight deflection of particles away from the bottom side towards the center of the channel is noticeable at the expansion zone entrance especially for higher flow rate of 10 mL/hr. This can be attributed to the removal of the magnetophoretic force in the section following the magnetic zone exit until the expansion zone entrance (34.5 mm $< X <$ 42 mm), that leaves the inertial lift and the drag as dominant forces determining the particles equilibrium positions. Numerical results show that at 10 mL/hr, particles equilibrium positions are approximately 5 μm higher at the expansion zone entrance than the magnetic zone exit.

3.1.3.2 Effect of Magnetization on Inertia-Magnetic Focusing of Microparticles

With the numerical model validated against the experimental measurements, we investigated the effect of other important parameters on the focusing of microparticles, starting with the magnetization effect, M (section 2.1.2.2, Eq. (11)). Magnetization can be changed using different magnets and their orientation and positioning in the straight microchannel device in order to enhance the quality and efficiency of particle focusing and sorting. Accordingly, we investigated the exit position of 11μm magnetic particles flowing at 3mL/hr in the straight microchannel device with different magnetizations in Fig. 3-9.

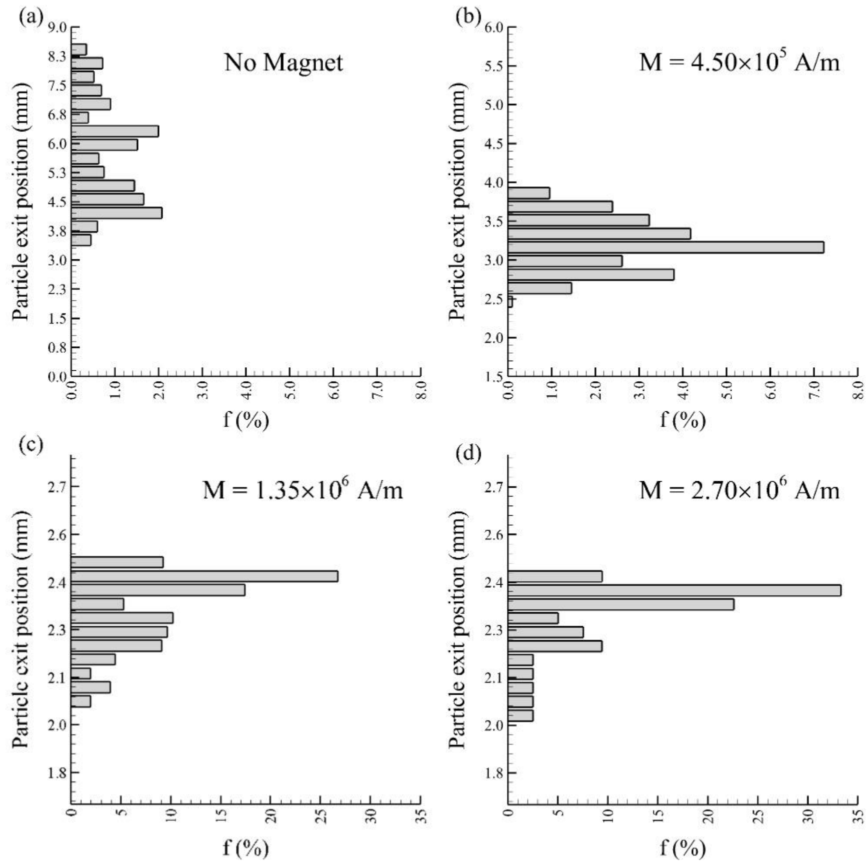

Fig. 3-9. Exit position of magnetically focused 11 µm particles flowing at 3mL/hr with different magnetization magnitudes of (a) M=0 with no magnet, (b) M=4.50×10⁵ A/m, (c) M = 1.35×10⁶ A/m and (d) M = 2.7×10⁶ A/m

As displayed in Fig. 3-9, by increasing the magnetization, particles' focusing quality was enhanced significantly. With no magnet in the setup, particles were randomly distributed over a wide region of the outlet within 3.42–8.33mm from the baseline. Increasing the magnetization to 4.5×10^5 A/M (~17% of the experimental value [21]) enhanced the effect of magnetic focusing. In this case, particles were found to be distributed over a narrower range of 2.42–3.82mm from the baseline. For magnetizations higher than 1.35×10^6 A/M (~50% of the experimental value [21]), magnetic saturation was achieved and no significant change in the focusing was observed. For these cases, particle distribution ranges were found to be almost identical to those of the experiment at 2.02–2.46mm. This study indicates that some design modifications can be considered to accommodate even a weaker magnet, with the same length, in this microfluidic setup to achieve similar results.

At lower magnetization values of 4.5×10^5 A/m, increasing the length of the magnet may also allow the particles to better focus along the channel sidewall before entering the expansion zone.

3.1.3.3 Effect of Microparticle Diameter on Inertia-Magnetic Focusing

Microparticles of various sizes are used as surrogates for biological substances to design microfluidic sorters, or as carriers for conjugation of target analytes and their separation. Microplastic contaminants in water, with variations in size and shape, are also becoming an important concern in water quality applications [165, 166]. Therefore, the impact of changing the microparticle size on their inertia-magnetic focusing and exit position from the straight microchannel device was studied numerically. The distribution of magnetic microparticles with different diameters of 5, 11, 20 and 30 μm, flowing at 0.5mL/hr is displayed in Fig. 3-10. Magnetization was kept at M=2.7×10^6A/M in all cases, similar to the previously used experimental value.

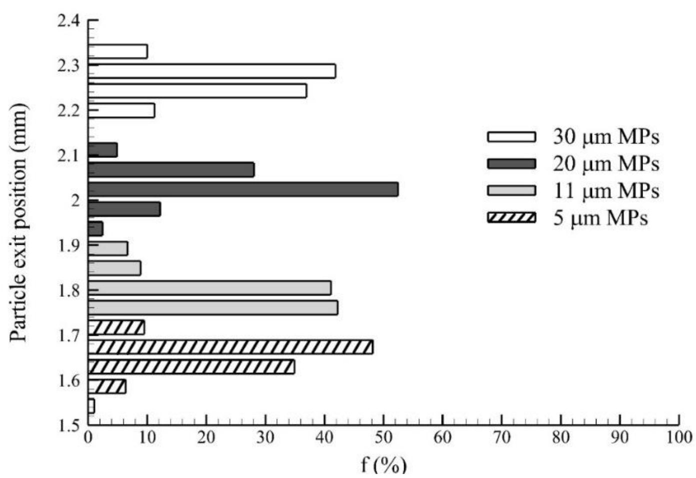

Fig. 3-10. Exit position of inertia-magnetically focused microparticles with different sizes flowing at 0.5mL/hr in the straight microchannel. Magnetization was 2.7×10^6 A/M in all cases.

The exit positions were found to be 1.54–1.72mm, 1.72–1.89mm, 1.94–2.11mm, and 2.20–2.33mm for 5, 11, 20 and 30μm microparticles, respectively. As demonstrated, there is a direct relation between the particles exit position and their size, meaning that larger particles concentrate further away from the baseline at a given flow rate. After inertia-magnetic focusing on top of the magnet, larger particles experience larger inertial forces towards the center of the channel in the narrowing section, as shown in Eq (10), hence they assume positions further away from the baseline.

This modeling also demonstrated that a fourplex separation is potentially achievable for the range of particles, magnetization and flow rates reported above. This was later shown in almost similar experimental settings by Kumar and Rezai [10].

3.1.3.4 Effect of Fluid Viscosity on Inertia-Magnetic Focusing of Microparticles

Recently, a significant attention has been given to fluids other than water due to the prominence of viscoelastic and non-Newtonian solutions in various biomedical applications [167-171]. Hence, we became interested in studying the effect of fluid viscosity on inertia-magnetic focusing of microparticles in the straight microchannel. DI water viscosities were obtained from Sabaghan et al. [172] with the density being relatively unchanged within the studied viscosity range ($0.5 < \mu$ (m.Pa.s) < 1.5). The results are presented for 11μm particles in two cases of constant Re_p and constant flow rate in Fig. 3-11a and 3-11b, respectively. Magnetization was kept at $M=2.7\times10^6$ A/M in all cases.

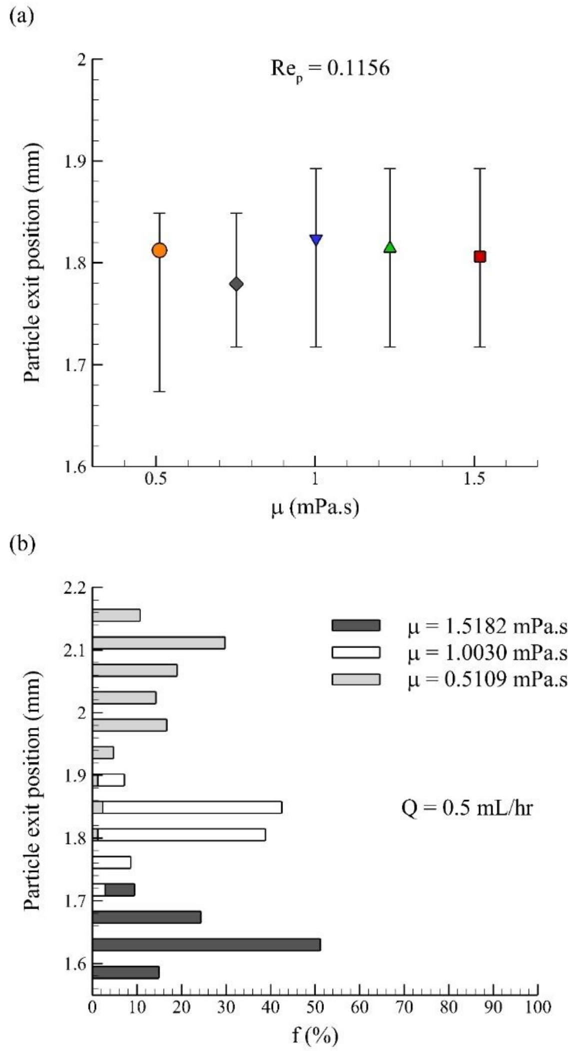

Fig. 3-11 Effect of fluid viscosity on exit position of inertia-magnetically focused 11µm particles at (a) $Re_p = 0.1156$ and (b) Q = 0.5mL/hr. Magnetization was 2.7×10^6 A/M in all cases.

As shown in Fig. 3-11a, for the case of constant particle Reynolds number, changes in fluid viscosity barely had an impact on the particle exit position. The 11µm particles exited the device within the range of 1.67–1.89mm with a mean position of 1.81mm when fluid viscosity was decreased from 1.52mPa.s to 0.51mPa.s. Drag force on the particles is directly dependent on the fluid dynamic viscosity and particle velocity (see Eq. 8) In order to keep the particle Reynolds number (Re_p) constant, we needed to increase the flow rate as well to compensate for the increased viscosity. Therefore, drag force and the resulting hydrodynamic separation would not change significantly. On the other hand, at a constant flow rate of 0.5mL/hr in Fig. 3-11b, as the fluid viscosity declined (Re_p increased), particles were focused further away from the baseline. In this case, the exit position of 11µm particles were 1.59–1.72, 1.63–1.85, 1.72–1.89, 1.76–1.94 and 1.80–2.16 mm for the fluid viscosities of 1.52, 1.23, 1.00, 0.75 and 0.51 mPa.s, respectively (some not shown in Fig. 3-11b due to overlap, and for better visualization of other data points). At a constant flow rate and particle diameter (Fig. 3-11b), increasing the viscosity increases the drag force on the particles while not changing other acting forces significantly (Eq. 10 and 11). In the narrowing section, particles migrating inertially to the channel center experience larger resistive drag forces towards the channel sidewall in more viscous fluids, hence they assume positions closer to the baseline.

3.2 Microparticle Focusing in non-Newtonian Shear-Thinning Viscoelastic Fluids[††]

This section describes verification, validation, parametrical study and the proposed design thresholds that was conducted with the developed elasto-inertial model (section 2.2) to address the second objective (section 1.3) of the thesis. In this section of the thesis, we tried to present our data in non-dimensional forms after learning about the benefits of this method in the literature.

We first verified our model by investigating its mesh independency and fluid flow characteristics for both Newtonian and viscoelastic fluids. The model was then validated against the experimental results obtained by us [15] and other researchers [23] in which particle dispersion in viscoelastic

[††] The results of section 3.2 are published in 140. Charjouei Moghadam, M., A. Eilaghi, and P. Rezai, *Elasto-inertial microparticle focusing in straight microchannels: A numerical parametric investigation.* Physics of Fluids, 2021. **33**(9): p. 092002.

fluids inside straight channels with square cross sections were investigated. We then used our validated model to conduct a parametric study on all the non-dimensional numbers involved in this phenomenon to propose a correlation for predicting the particle focusing in viscoelastic fluids in microchannels.

3.2.1 Model Verification

3.2.1.1 Mesh Independency Study

The device geometry in Fig. 2-2 was meshed with rectangular cells with regular connectivity. To ensure mesh independency of our simulations, while minimizing the computational costs, several mesh sizes corresponding to the number of mesh elements in the range of 7.125×10^4 to 1.14×10^6 were considered. Based on our initial investigations, we found that the variation of elastic lift force along the width of the channel was heavily mesh dependent. Also, along the centerline of the elasto-inertial focusing microchannel, large variations in fluid viscosity were observed for different mesh densities. Therefore, the normalized elastic lift force and fluid viscosity (by their corresponding maximum values), along the normalized width (Y/W_F) and centerline ($X/(L_F+L_E)$) of the microchannel were plotted in Fig. 2-2, for different mesh sizes in the case of 1000 ppm PEO flowing at 1.5 mL/hr. Equations 4 and 12 were used for the fluid viscosity and elastic force acting on the particles, respectively. The mesh was more refined near the microchannel walls and the entrance of the expansion zone to accurately estimate the flow fluctuations around these areas.

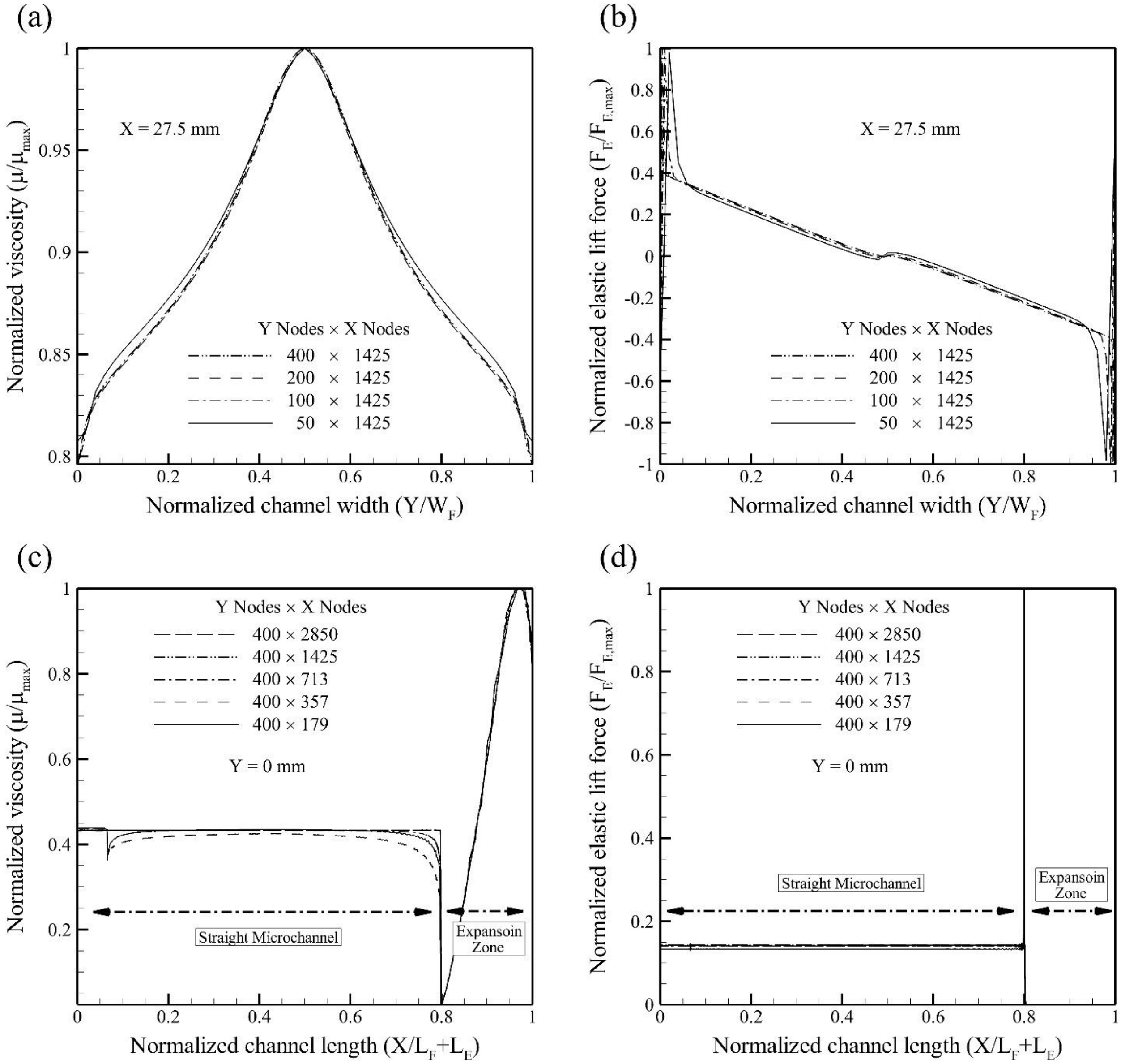

Fig. 3-12. Normalized viscosity (a and c) and normalized elastic lift force (b and d) profiles against the normalized channel width (a-b) and the normalized channel length (c-d) for various mesh sizes.

In Fig. 3-12a and 3-12b, for normalized viscosity and elastic lift force, respectively, the number of nodes along the width of the channel varied while it was kept constant at 1425 nodes along the channel length. As shown, increasing the number of width nodes from 200 to 400 had a negligible impact of less than 0.01% on the normalized viscosity and elastic lift force, while lower number of nodes at 100 and 50 had a significant effect on these values. The same trend was followed in

Fig. 3-12c and 3-12d where the number of nodes along the length of the channel varied while the width nodes remaining constant at 400. Variations were indistinguishable when the number of length nodes were increased from 1425 to 2850 with less than 0.005% difference measured between the results. According to these results, the rectangular grid structure of 200×1425 nodes was selected for this study.

3.2.1.2 Fluid Flow Study

Our verification was further followed by comparing the micro-PIV based velocity profiles of Newtonian and non-Newtonian fluid flows in a straight microchannel with a square cross section from [22], with the results of our numerical model in Fig. 3-13.

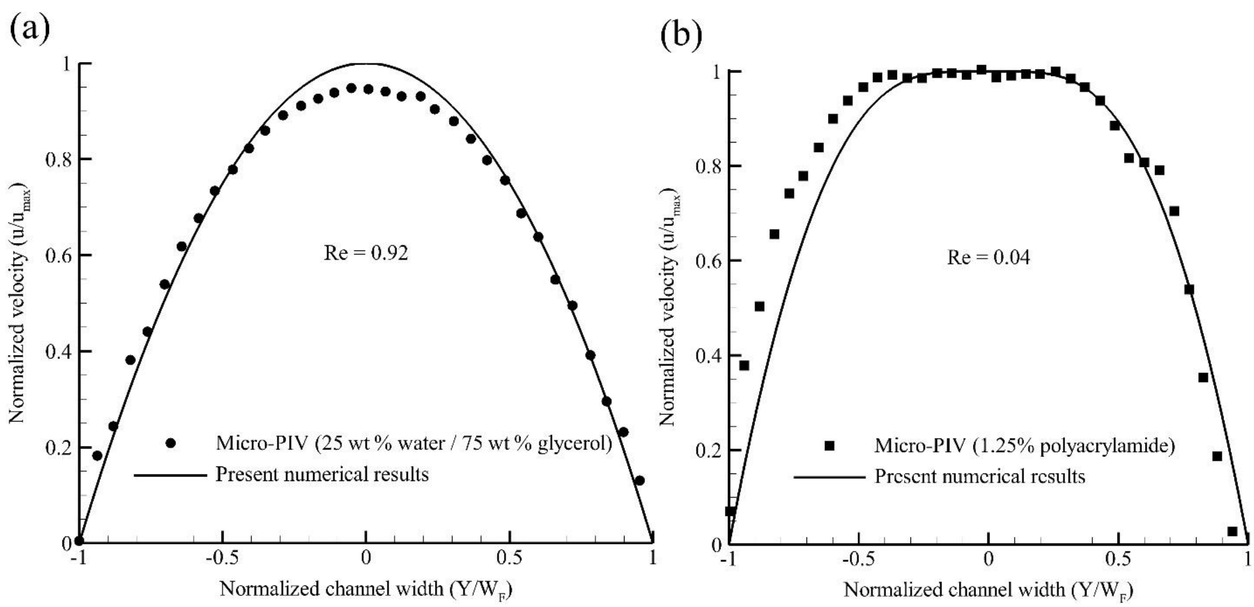

Fig. 3-13. Normalized velocity profiles of our numerical model against the micro-PIV measurements of Fu et al. [22] for (a) a Newtonian fluid with 25 wt % water and 75 wt % glycerol, and (b) a non-Newtonian viscoelastic fluid of 1.25% polyacrylamide in water.

In Fig. 3-13a, normalized velocity distribution in the mid-plane of a 400 µm × 400 µm straight microchannel is plotted for a 25 wt% water and 75 wt% glycerol solution flowing at Re = 0.92. As shown, an agreement between our numerical results and the micro-PIV measurements of Fu et al. [22] with an average mismatch of 0.5% is observed.

As for the viscoelastic flow in Fig. 3-13b, our numerically obtained velocity profile is compared with the micro-PIV velocity profile of the polyacrylamide (PAAM) solution of 1.25% concentration in a 600 μm × 600 μm straight microchannel [22]. Carreau parameters in Eq. (4) for this viscoelastic solution were taken from fu et al. [22]. The major characteristic of the viscoelastic fluid flow is the flattened profile in the central part of the channel. This can be explained by the increased viscosity of the shear-thinning fluid at the center due to the decrease in the shear rates. Again, an agreement between our numerical model and the micro-PIV measurements is demonstrated with an average mismatch of 2%. The maximum mismatch between the results in Fig. 3-13a and Fig. 3-13b are ∼7% and ∼15%, respectively.

The results of this section verify the applicability of the proposed numerical scheme for the shear-thinning non-Newtonian fluids. In the following section, we could inject the microparticles into the model and validate it against the experiments by our group and others [15, 23].

3.2.2 Model Validation

3.2.2.1 Elasto-Inertial Focusing of Microparticles

The capability of our model in predicting the particle trajectories in Newtonian and viscoelastic flows inside a straight channel (Fig. 2-2a) was investigated in reference to our experimental data [15]. The distribution of 9 μm microparticles flowing in deionized (DI) water and 2000 ppm PEO solution at 1.0 ml/hr was simulated around the expansion zone of the device as shown in Fig. 3-14. Note that the experimental Figs. 3-14ai and 3-14bi were produced by Dibaji et al. [15] by overlaying 500 frames of captured images at the expansion region of their device to enhance the visibility of the particles, while the numerical results in Figs. 3-14aii and 4bii are shown for single frames. This resulted in particle concentrations to appear higher in the experimental figures.

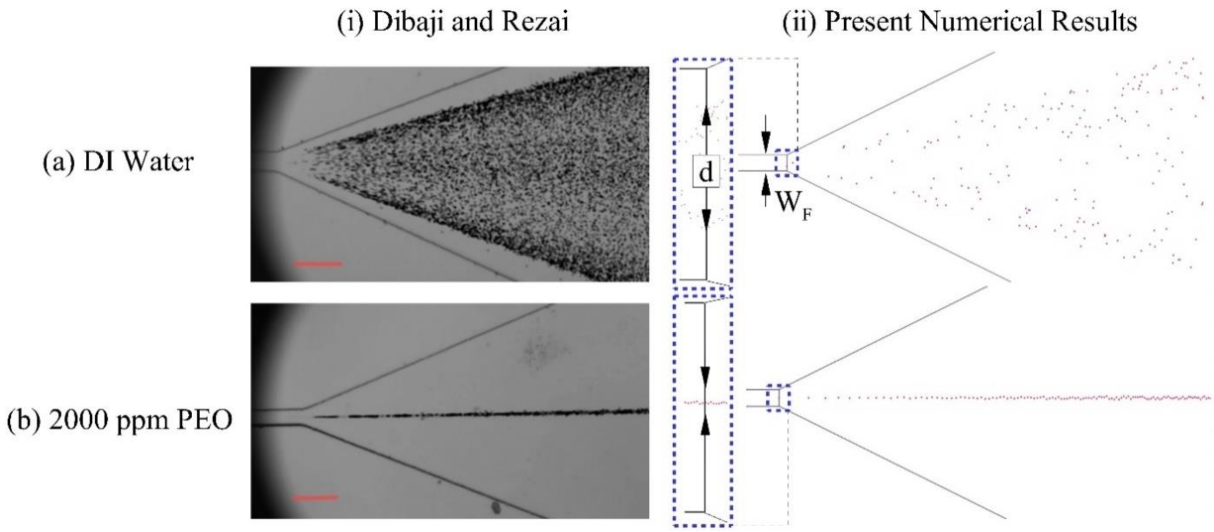

Fig. 3-14. Distribution of 9 µm particles flowing in (a) deionized (DI) water and (b) 2000 ppm PEO solution at 1.0 ml/hr. Comparison of the (i) experimental investigation of Dibaji and Rezai [15] *(scale bars = 200 µm) with the (ii) present numerical results. Particle dispersion, d, is delineated on the numerical results of DI Water. Image reproduced with permission from Journal of Magnetism and Magnetic Materials.*

As observed in Fig. 3-14ai, experimental particles are randomly distributed in the case of Newtonian DI water flow while being slightly diverted away from the channel side walls due to the effect of the wall-induced inertial lift force. This behaviour is well captured by our numerical model as illustrated in Fig 3-14aii. Introducing viscoelasticity to the solution in Fig. 3-14bi, the experimental result shows that the particles focus at the center of the channel, as the elastic lift force dominates the inertial lift and hydrodynamic drag in this case [15], which is again captured well in our model in Fig. 3-14bii. Altogether, there is a strong agreement between the numerical simulation and the experimental results, because our model captures both dispersion (Fig. 3-14aii) and focusing (Fig. 3-14bii) regimes of the microparticles with accuracy.

3.2.2.2 Quantitative Validation of Elasto-Inertial Microparticle Focusing

For quantitative analysis, we used the dimensionless particle dispersion factor, $D = d/D_h$, with d being the dispersion of the particles in the narrow channel (measured at the beginning of the expansion zone) as shown in Fig. 3-14, and $D_h = W_F = H$ being the square channel hydraulic diameter. Using D, the cross section of the channel was divided into different bands with $D=0.2$ intervals. The fraction of focused microparticles at the first focusing band of the microchannel (f_1) that corresponds to the normalized number of particles in the $D=0.2$ circle was determined as shown in Fig. 3-15. The experimental results of Del. Giudice et al. [23] were chosen as reference, in which the focusing of 5 and 10 μm particles in straight microchannels with hydraulic diameters of 50 and 100 μm were investigated under the effects of *De* number, non-dimensional channel length (L) and the particle to channel blockage ratio (β), all combined in their parameter $De.L.\beta^2$ [23].

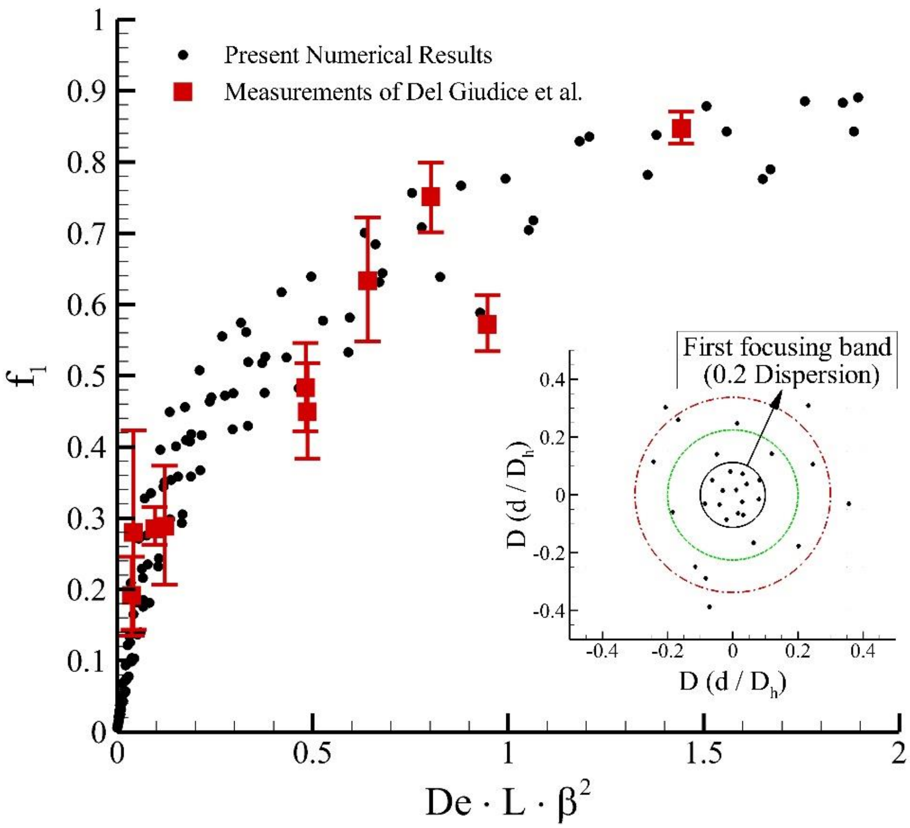

Fig. 3-15. Fraction of particles in the first focusing band, f_1, located at D=d/Dh=0.2, as a function of non-dimensional parameter $De \cdot L \cdot \beta^2$ [23]. Comparison of Del. Giudice et al. [23] experimental results with the present numerical simulation.

As shown in Fig. 3-15, more particles will focus at the first focusing band as the value of parameter $De.L.\beta^2$ increases. This happens because the combined effects of viscoelasticity, inertia, particle diameter and channel dimensions are working favorably towards particle focusing when this complex nondimensional parameter is increased. For the investigated range of $De.L.\beta^2$, our 162 numerical datapoints fit within the thresholds of the 15 experimental datapoints by Del. Giudice et al. [23]. The maximum mismatch occurs at $De.L.\beta^2 = 0.52$ where our numerical prediction overestimates the experimental percentage of focused particles by about 8%. For the remaining cases, there is a reasonable agreement between the numerical predictions and the experimental measurements with an average mismatch of $\sim$ 3%.

The results in this section prove that our model can accurately predict the behavior of viscoelastic flows and suspended microparticles inside microchannels. In the next section, we applied our model to investigate the effect of other parameters on microparticles focusing that has not been reported experimentally to date.

3.2.3 Parametric Numerical Study

We implemented an analysis based on Buckingham Π theorem to determine the significant non-dimensional numbers governing particle focusing in a viscoelastic flow in a straight microchannel with a square cross-section. For this purpose, the significant parameters in particle focusing and their corresponding dimensions were determined in Table 3-1.

Table 3-1. Significant parameters used in the Buckingham Π *analysis*

Variable		Dimension
U	Average Velocity (U=Q/A)	LT^{-1}
d	Particle Dispersion (Fig. 4)	L
d_p	Particle Diameter	L
λ	Relaxation Time	T
μ_0	Viscosity	$ML^{-1}T^{-1}$
ρ	Density	ML^{-3}
D_h	Hydraulic Diameter (D_h=W=H)	L
X	Channel Length	L

According to the Buckingham Π theorem, having 8 variables and 3 primary dimensions results in 8 - 3 = 5 dimensionless numbers that would impact the particle focusing in our channel. These dimensionless numbers are presented in Table 3-2.

Table 3-2. Dimensionless numbers of Buckingham Π analysis

Dimensionless number		Definition	
π_1	D	$\frac{d}{D_h}$	Dimensionless particle dispersion
π_2	β	$\frac{d_p}{D_h}$	Blockage ratio
π_3	De	$\frac{U\lambda}{D_h}$	Deborah number
π_4	Re	$\frac{\rho D_h U}{\mu_0}$	Reynolds number
π_5	L	$\frac{X}{D_h}$	Dimensionless length

We conducted a parametric study with 162 computational simulations based on the variables in Table 3-2. In the parametric study, 4 parameters of flow velocity (U), particle size (d_p), channel hydraulic diameter (D_h) and channel length (X) were changing. The levels used for each parameter and the resulting 162 possible run combinations are provided in Table 3-3.

Table 3-3. Varying parameters and their levels used in the parametric study.

	Level 1	Level 2	Level 3
U (mm/s)	2.78	27.8	278
d_p(µm)	2	6	10
D_h(µm)	75	100	125
X (mm)	27.5	55	N/A

An expression for the dimensionless particle dispersion number, *D*, as a function of other non-dimensional numbers in Table 3-2, for viscoelastic particle flows in straight microchannels of square cross section was sought. Then, our full parametric dataset was plotted against the proposed non-dimensional $De.L.\beta^2$ number by Del Giudice et al. [23] and their hypothesis on particle focusing was evaluated. Finally, our dataset was plotted against a modified version of $De.L.\beta^2$ to account for the *Re* number, and a new expression was proposed for microparticles dispersion in viscoelastic flows inside square cross-section microchannels. These studies are described below.

3.2.3.1 Effect of Channel Hydraulic Diameter on Elasto-Inertial Focusing

The effect of channel hydraulic diameter, D_h, at different PEO concentrations (properties derived from [142])were investigated on the particles dispersion, *d*, for 6 μm microparticles as plotted in Fig. 3-16.

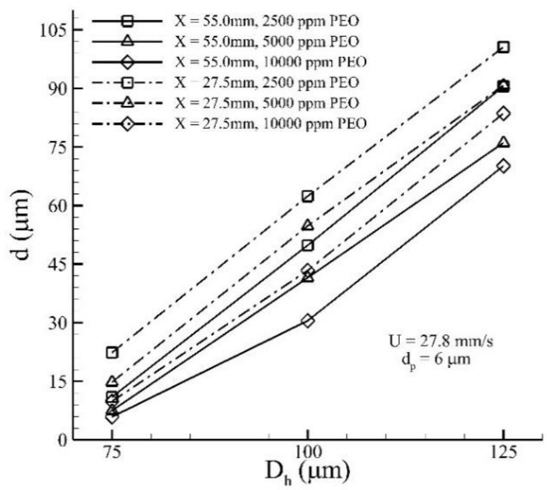

Fig. 3-16. The effect of channel hydraulic diameter, D_h, on particle dispersion, d, for various PEO concentrations for 6 µm particles flowing at U=27.8 mm/s at different channel lengths.

As shown, particle dispersion is increased with channel hydraulic diameter for all the investigated cases. Dimensions of the channel affect the inertial and elastic forces as well as Re, De, and Elasticity number ($El = \frac{2De}{Re} = \frac{2\lambda\mu}{\rho {D_h}^2}$). The inertial lift force in Eq. (10) depends on the squared inverse of the channel hydraulic diameter ($\vec{F}_L \sim \frac{1}{{D_h}^2}$). In particular, the wall component of the inertial lift force ($\vec{F}_{WI} \sim \frac{1}{{D_h}^4}$), that pushes the particles towards the center of the channel, decreases faster than the shear gradient component ($\vec{F}_{SG} \sim \frac{1}{D_h}$) as the channel hydraulic diameter increases. In order to investigate the impact of elastic and inertial lift forces against each other, one can investigate El number as it considers both elasticity and inertial effects. For instance, by decreasing the microchannel size from 125 µm to 75 µm for a 5000 ppm PEO solution in a 55mm channel, El number increases from 4.5 to 12.6. This interaction of forces results in a larger dispersion of particles across the channel width for higher values of hydraulic diameter.

Increasing the PEO concentration of the solution in Fig. 3-16 helps the particles reach elasto-inertial focusing. According to Eq. (12) both relaxation time and polymeric contribution to viscosity increases with an increase in PEO concentration [157, 159]. Elastic lift force is directly proportional to both parameters. Expectedly, particle focusing is reinforced as the elastic lift force is increased. This phenomenon can also be characterized with the help of Elasticity number, El. For instance, for a 100 µm wide microchannel with a 2500 ppm PEO solution, the El number is 0.158 while this value increases to 0.902 at a PEO concentration of 10000 ppm. EI is directly proportional to viscosity and relaxation time and its increase suggests dominance of elastic forces and enhanced focusing of microparticles.

3.2.3.2 Effect of Microparticle Diameter on Elasto-Inertial Focusing

Various sizes of microparticles can be used either as surrogates of biological targets in developing microfluidic sorters, or as carriers for immunocapturing and isolation of target analytes. The impact of changing the microparticle diameter in the range of 2-10 µm on their elasto-inertial focusing in our device was studied numerically in Fig. 3-17.

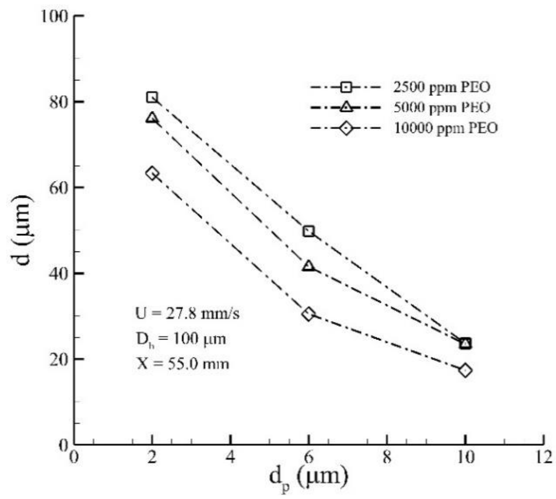

Fig. 3-17. Particle dispersion (d) versus particle diameter (d_p) in viscoelastic fluids with various PEO concentrations, flowing at U=27.8 mm/s in a microchannel with 55 mm length and 100 µm hydraulic diameter.

As shown in Fig. 3-17, when the particle size is increased, the particle dispersion, d, decreases indicating stronger elasto-inertial focusing at the center of the channel. Considering the fact that the magnitudes of the inertial and elastic lift forces are dependent on the 4^{th} and 3^{rd} power of particle diameter, respectively, this significant focusing improvement is expected with increasing the particle diameter.

3.2.3.3 Effect of Flow Velocity on Elasto-Inertial Focusing

Another important parameter affecting elasto-inertial focusing is the flow velocity. The effect of flow velocity on the dispersion of microparticles throughout the width of the focusing channel is shown in Fig. 3-18.

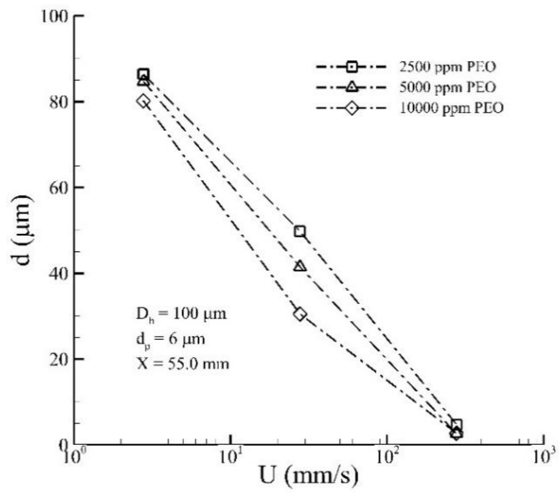

Fig. 3-18. Particle dispersion (d) versus flow velocity (U) in viscoelastic fluids with various PEO concentrations containing 6 µm particles and flowing in a channel with 55 mm length and 100 µm hydraulic diameter.

As shown in Fig. 3-18, increasing the flow velocity would lead to less particle dispersion. Flow velocity affects both the inertial and elastic lift forces according to Eq. (10) and Eq. (12). By increasing the flow velocity, the magnitude of inertial lift and elastic lift on the particles increases. Combination of these enhanced forces would reinforce elasto-inertial focusing and results in less particle dispersion.

From Figs. 3-16 to 3-18, we can deduce that the elasto-inertial focusing is improved with the increase in particle diameter, fluid viscoelasticity and flow velocity while increasing the channel hydraulic diameter would have an inverse influence on focusing. These effects were captured correctly by our numerical model. In order to develop an accurate parametric criterion for particle focusing, we need to investigate the effects of significant non-dimensional numbers which will be presented in the next section.

3.2.4 Non-Dimensional Numerical Analysis of Elasto-Inertial Focusing

In this section, non-dimensional numbers derived from the Buckingham Π analysis in Table 3-2 and their significance and impacts on the non-dimensional dispersion of microparticles, $D=d/D_h$, was numerically investigated as plotted in Fig. 3-19. De numbers versus blockage ratio and dimensionless length are displayed in Fig. 3-19a and 3-19b, respectively. Re numbers versus blockage ratio and dimensionless length are depicted in Fig. 3-19c and 3-19d, respectively. In Fig. 3-19, D-values are depicted in five color coded ranges with higher values indicating a wider dispersion of microparticles across the width of the microchannel. Following Del. Giudice et al. [23] guidelines, $D<0.2$ was considered as elasto-inertial focusing at this stage of our studies, which is not the most accurate representation of elasto-inertial focusing as highlighted later in this chapter.

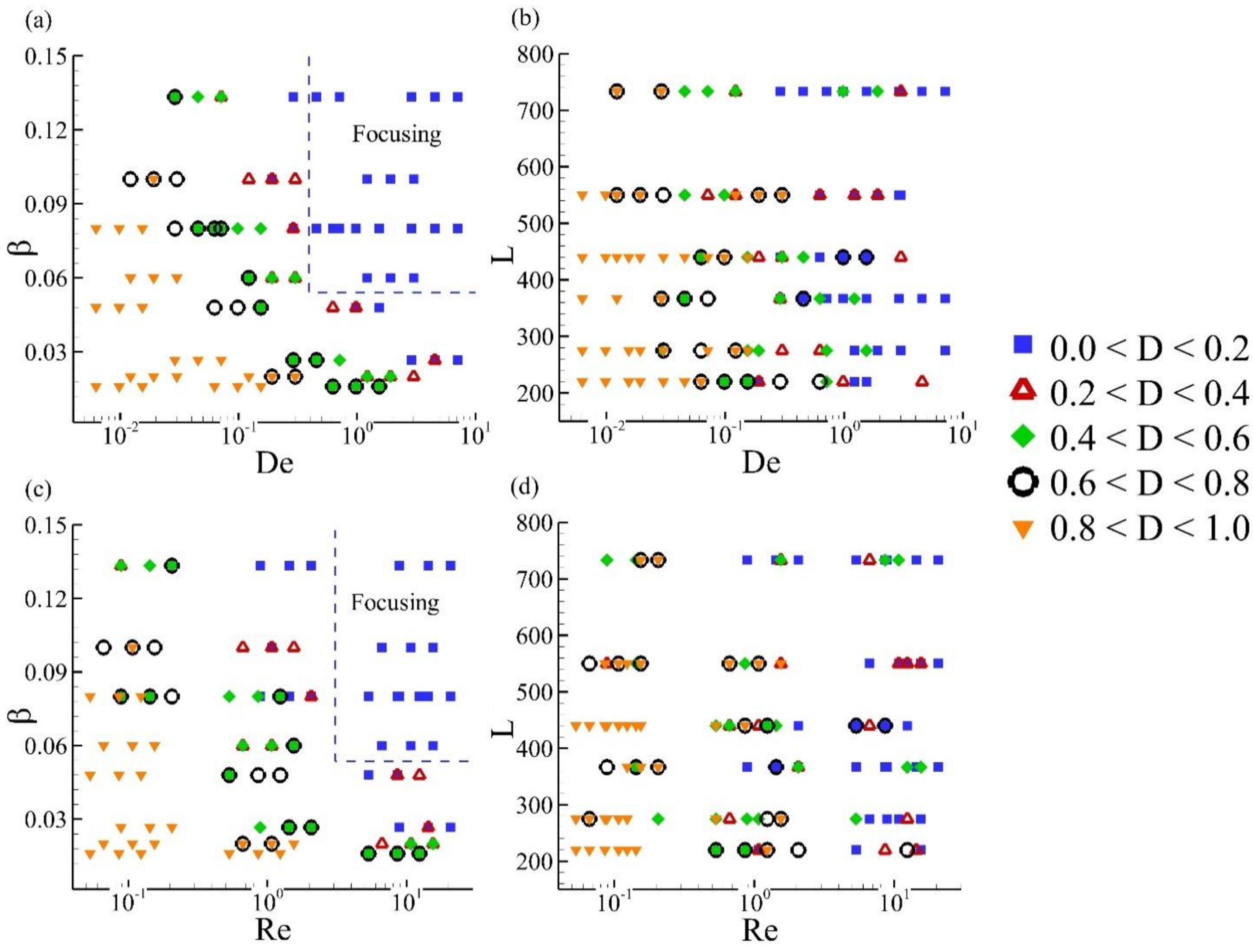

Fig. 3-19: Full numerical dataset of dimensionless particle dispersion, $D=d/D_h$, plotted against other significant non-dimensional parameters based on a Buckingham Π analysis. (a) Blockage ratio vs Deborah number, (b) Dimensionless channel length vs Deborah number, (c) Blockage ratio vs Reynolds number and (d) Dimensionless channel length vs Reynolds number.

According to Fig. 3-19a, increasing both the blockage ratio and the De number would enhance the quality of elasto-inertial particle focusing in the straight microchannel. It is observed that for De>0.4 and β>0.05, particles would be focused over 20% of the channel width. There is not a clear distinction in particle focusing regimes in Fig. 3-19b along the vertical axis, since the impact of dimensionless channel length is not as pronounced as De and β. When De>1, particles experience an enhanced elastic lift force and therefore focus more at the channel center. The same pattern as Fig. 3-19a is observed in Fig. 3-19c, showing that increasing the Re and β would enhance the microparticle focusing quality. For these cases, dimensionless dispersion threshold of D<0.2 is achieved for Re>3 and β>0.05. At higher Re, the inertial lift force is enhanced which will contribute to elasto-inertial focusing of microparticles. Finally, as shown in Fig. 3-19d, the effect of dimensionless channel length is not as significant as Re and β.

In order to examine the combined effects of different non-dimensional parameters and provide a design guideline for microparticle focusing in viscoelastic flows, our full numerical dataset of non-dimensional particle dispersion, D, was plotted against the proposed non-dimensional number by Del-Giudice et al. [23] (i.e., $De \cdot L \cdot \beta^2$) as shown in Fig. 3-20a.

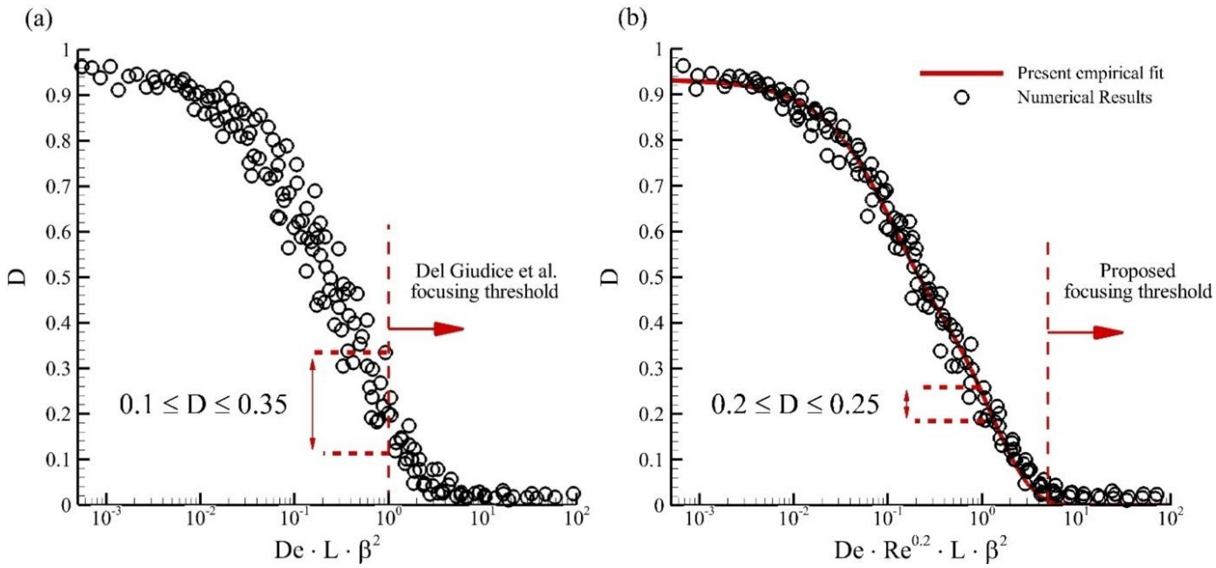

Fig. 3-20. Full numerical dataset of dimensionless particle dispersion, D, against (a) the non-dimensional number of Del. Giudice et al. [23] *($De \cdot L \cdot \beta^2$) and (b) our proposed non-dimensional number ($De \cdot Re^{0.2}. L \cdot \beta^2$).*

From the results in Fig. 3-20a, we confirmed the same distribution pattern of dimensionless particle dispersion D versus ($De \cdot L \cdot \beta^2$) as observed by Del Giudice et al. [23]. There is an almost plateau region of full particle dispersion (D>0.9) when ($De \cdot L \cdot \beta^2$)≤0.01 followed by a linear decrease in dispersion until it plateaus again and enters a focusing regime (D<0.05) when ($De \cdot L \cdot \beta^2$)≥4.0. Our dataset is randomly distributed over the whole range of ($De \cdot L \cdot \beta^2$) values capturing all three modes of full dispersion, full focusing, and the in-between transition region. This highlights the appropriate choice of parameters and their ranges for this study.

At the proposed focusing threshold of $(\mathrm{De} \cdot \mathrm{L} \cdot \beta^2)$=1.0 by Del. Giudice et al [23], the D value is $\sim$0.2. This is expected and validated with our model, as this threshold determines particles to be focused if over 90% of them are concentrated within a 20% dispersion band. However, at this focusing threshold particles are far from being fully focused and are still dispersed throughout 20% of the channel width. Also, at a given $\mathrm{De} \cdot \mathrm{L} \cdot \beta^2$ parameter especially in the middle region, (0.01< $\mathrm{De} \cdot \mathrm{L} \cdot \beta^2$<0.2), the variation in the dispersion is quite large. For instance, at the proposed focusing threshold of $\mathrm{De} \cdot \mathrm{L} \cdot \beta^2 = 1$, the predicted dispersion D varies in the range of $0.1 \leq \mathrm{D} \leq 0.35$.

Deborah number accounts for the effects of fluid elasticity while Reynolds number mainly describes the effects of inertia in microfluidics particle focusing. In this study, we are dealing with elasto-inertial effects, so the contribution of both parameters are physically relevant to be considered. This is further supported by our Buckingham Π analysis reported above. In order to improve the focusing prediction, we added the effect of Re number, i.e. Re^n, to the proposed non-dimensional parameter by Del. Giudice et al. [23] leading to $\sigma = \mathrm{De} \cdot \mathrm{Re}^{\mathrm{n}} \cdot \mathrm{L} \cdot \beta^2$. Different values of power n were tested, and an exponential empirical equation was fitted on datapoints. The root mean squared error was used as a goodness-of-fit measure to compare each fit. A power n of 0.2 was found to provide the best fit to our data with a root mean squared error value of 0.03. Therefore, a modified non-dimensional number $\sigma = \mathrm{De} \cdot \mathrm{Re}^{0.2} \cdot \mathrm{L} \cdot \beta^2$ was introduced as shown in Fig. 3-20b. This modification reduces the variations on predicted dispersion of microparticles from $0.1 < D < 0.35$ in Fig. 3-20a to $0.2 < D < 0.25$ in Fig. 3-20b.

Same pattern as Fig. 3-20a is observable in our modified correlation. Again, plateaus of full dispersion (D > 0.9) and focusing (D < 0.2) modes are seen for $\sigma < 0.009$ and $\sigma > 5$, respectively, with a linearly decreasing dimensionless dispersion in the middle region. Due to the addition of the $\mathrm{Re}^{0.2}$ term, there is less variation in D for a given σ value as datapoints are more compacted in Fig. 3-20b. At $\sigma \geq 5$, particles were found to be focused on a single line with less than 3% dispersion.

Finally, an exponential correlation, Eq. (13), was fitted to our datapoints in Fig. 3-20b to predict elasto-inertial particle dispersion based on the proposed modified dimensionless number. Using this correlation, the variation in predicted particle dispersion is reduced from $\sim$15% to less than $\sim$5%. These findings can be used to optimize the design of elasto-inertial microfluidic particle sorters and facilitate experimental designs.

$$\mathrm{D} = 0.38\ \mathrm{e}^{-10.94\sigma} + 0.55\ \mathrm{e}^{-0.81\sigma} \tag{13}$$

3.3 Microparticle Focusing in Shear-Thickening non-Newtonian Fluids

This section describes the results of an experimental study on microparticle focusing in shear-thickening nanofluids as per the third objective defined in this thesis (section 1.3). The experimental procedures were discussed in section 2.3. As mentioned in chapter 2, the straight microchannel that was tested for Newtonian and shear-thinning non-Newtonian fluids in our group [15] was adopted to investigate the behaviour of microparticles in SiO_2/water shear-thickening non-Newtonian nanofluids. These experimental results can serve as the dataset needed to develop and validate a numerical model for these fluids and expand the studies in our group in the future.

To the best of our knowledge and as reviewed in Chapter 1, this is the first work done on microparticle dynamics in shear thickening fluids in microchannels, therefore the results are mostly preliminary in this section, and the interpretations and discussions are yet to be matured. One major challenge in our research was the lack of our knowledge about the non-dimensional numbers that can describe the shear-thickening behaviour of the fluid, such as the Wi number in the case of shear-thinning fluids. Another challenge was the lack of formulas to estimate the magnitude of passive forces applied to microparticles in shear-thickening fluids, such as Eq. (12) that can be used to estimate the viscoelastic force on microparticles in shear-thinning fluids.

3.3.1 Proof-of-Concept Study for Microparticle Focusing in Shear-Thickening non-Newtonian Fluids

As a proof-of concept, we started our investigations by examining the behaviour of 10 µm microparticles in DI-water and a 2.0% v/v SiO_2/water shear-thickening nanofluid. Particles were injected into the straight microchannel (Fig. 2-3b and 2-3c) and imaged at the expansion region of the device under the microscope. As shown in Fig. 3-21a and 3-21b, particles were randomly distributed over the width of the channel for respective water flow rates of 1 and 5 ml/hr.

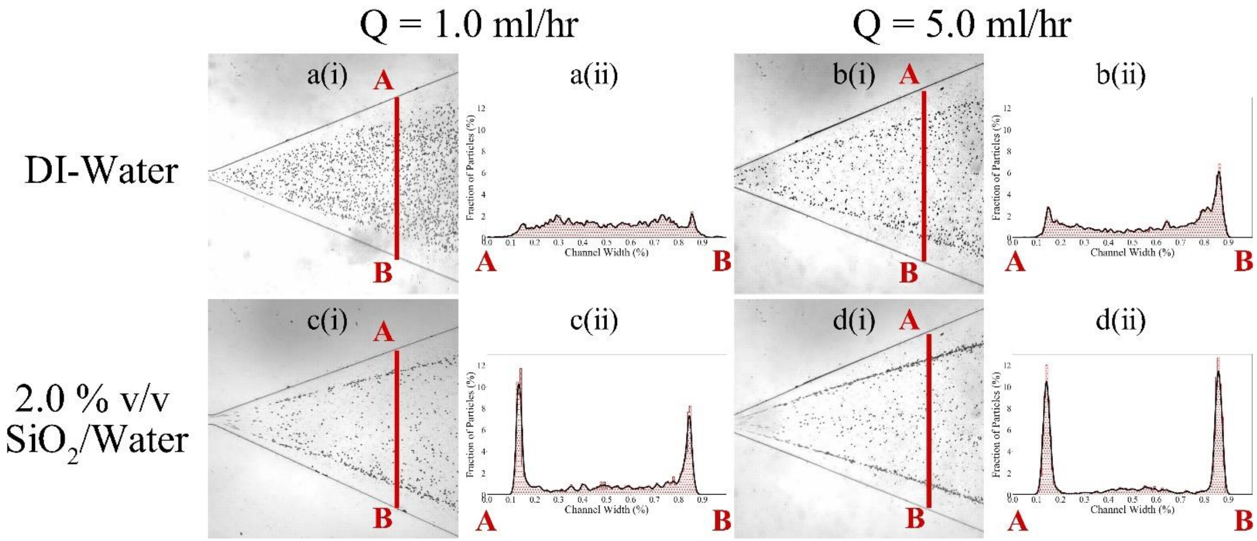

Fig. 3-21. 10 µm particles flowing in DI-Water (a & b) and 2.0% v/v SiO_2/Water nanofluid (c & d) at different flow rates of 1 ml/hr (a & c) and 5 ml/hr (b & d). Results are shown in terms of N=1248 overlayed frames of experimental results in (i) and quantitative fraction of particles across the width of the microchannel in (ii).

As a reminder (see section 3.1.2.3), it is widely accepted in the literature [63, 164] that when Re_p reaches unity, the chances of inertial focusing increases in a straight microchannel. At the water flow rate of 1 ml/hr in Fig. 3-21a, $Re_{p,10} = 0.34$, while this value increases to the marginal inertial focusing value of $Re_{p,10} = 1.7$ at the flow rate of 5 ml/hr. As shown, the $Re_{p,10}$ values above do not warrant inertial focusing while slightly higher inertial effects may be the reason behind a very minor accumulation of microparticles close to the sidewalls observed at 5 ml/hr in Fig. 3-21b.

After switching to the shear-thickening nanofluid, we observed a different behaviour in the microparticles as two distinct focusing lines near the sides of the channel appeared at approximately 15% and 85% of the channel width. First, particles migrated towards the two sidewalls of the channel for the 1 ml/hr case (Fig. 3-21c). As we increased the flow rate to 5 ml/hr (Fig. 3-21d), side focusing was improved and approximately 89% of the particles were found to be focused. Inertial focusing can not the reason for microparticles focusing in our shear thickening solutions as $Re_{p,10}$ for the 10 µm particles flowing at 1ml/hr and 5ml/hr in 2.0% v/v SiO_2/Water are 0.019 and 0.093 ($Re_{p,10} \ll 1$), respectively. Moreover, for strong inertial focusing in square microchannels such as the one used in our experiments, particles are expected to migrate towards the four center sides of the square cross section. Therefore, in a 2D top view of the channel such as the one shown in Fig. 3-21, three focusing lines, i.e., two at the sidewalls and one at the center of the channel, are expected to be seen. All in all, inertial focusing scenario was ruled out in this case and observations in Fig.3-21c and 3-21d were attributed to the shear thickening nature of the nanofluid, which warranted further parametric study on this phenomenon.

3.3.2 Effects of Flow Rate on Particle Focusing in Shear Thickening Fluids

As a major parameter affecting microparticle focusing, we continued our investigations by studying the effect of flow rate on the focusing quality of microparticles in a shear-thickening solution. Behavior of 10 µm particles flowing in 2.0% v/v SiO_2/Water were examined in different flow rates as shown in Fig. 3-22.

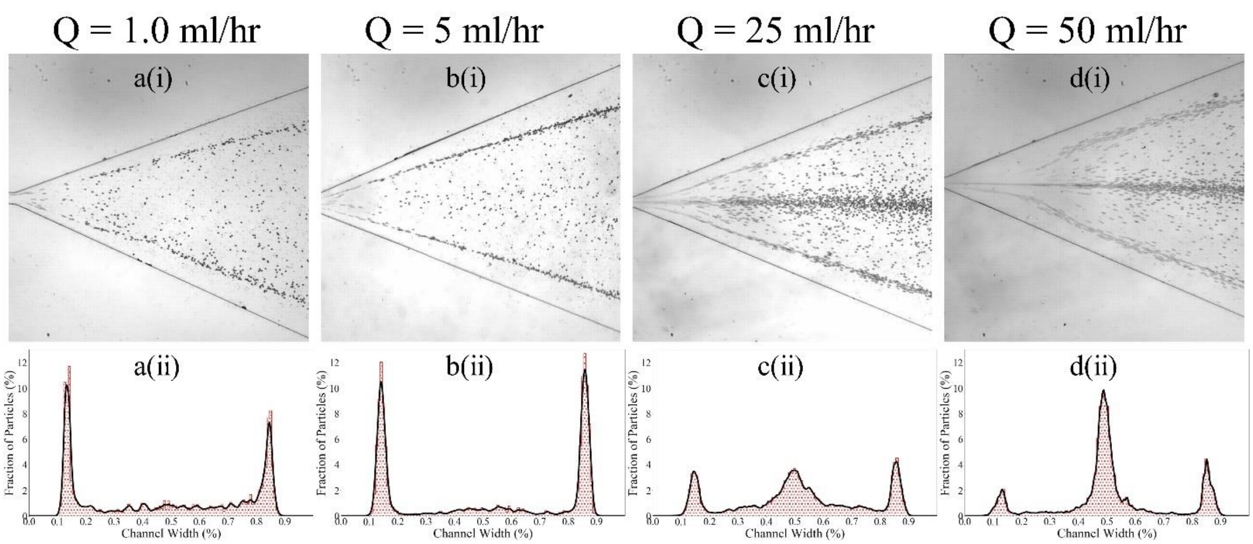

Fig. 3-22. Effects of flow rate on shear thickening focusing. 10 µm particles flowing in 2.0% v/v SiO_2/Water nanofluid at flow rates of (a) 1 ml/hr, (b) 5 ml/hr, (c) 25 ml/hr and (d) 50 ml/hr. Results are shown for N=1248 overlayed frames of experimental results in (i) and quantitative fraction of particles across the width of the microchannel in (ii).

As shown in Fig. 3-22, for the case of 1 ml/hr (Fig. 3-22a), around 68% of particles were found to be focused on the two focusing lines near the sides of the channel. As the flow rate was increased to 5 ml/hr (Fig. 3-22b), focusing was improved where approximately 89% of 10 µm particles were found to be focused. However, we saw a different focusing pattern when the flow rate was increased further to 25 ml/hr (Fig. 3-22c) and then to 50 ml/hr (Fig. 3-22d). In these cases, in addition to two focusing lines near the sides of the channel, a third focusing line at the center of the images started to appear.

For 10 µm particles flowing at 25 ml/hr (Fig. 3-22c) and 50 ml/hr (Fig. 3-22d), Re_p is 0.47 and 0.94, respectively, which is close to the order of inertial focusing threshold ($Re_p = 1$). Also, as discussed earlier (section. 1.2.1), in straight microchannels of square cross section, particles are inertially focused at the four sides of the channel. Therefore, in a 2D top view under the microscope, two focusing lines at the two sides and one focusing line at the center are expected to be seen. Considering the Re_p values and the experimental figures, one can hypothesize that the inertial forces are starting to dominate the shear-thickening effects at 25ml/hr and 50 ml/hr flow rates for 10 µm particles. Therefore, in these flow rates, three focusing lines would suggest that the focusing regime is possibly driven by inertial effects rather than shear-thickening.

3.3.3 Effects of Particle Size on their Focusing in Shear Thickening Fluids

Building up on our findings in the previous section, we investigated the effect of particle size on shear-thickening focusing. In the previous section, we found out that the shear-thickening effects were more pronounced at the flow rate of 5 ml/hr for 10 µm particles. Therefore, we chose this flow rate to study the impact of particle size on shear-thickening focusing in the SiO_2/Water solution. Distributions of microparticles with diameters of 5 µm, 10 µm and 15 µm tested in the above conditions are shown in Fig. 3-23.

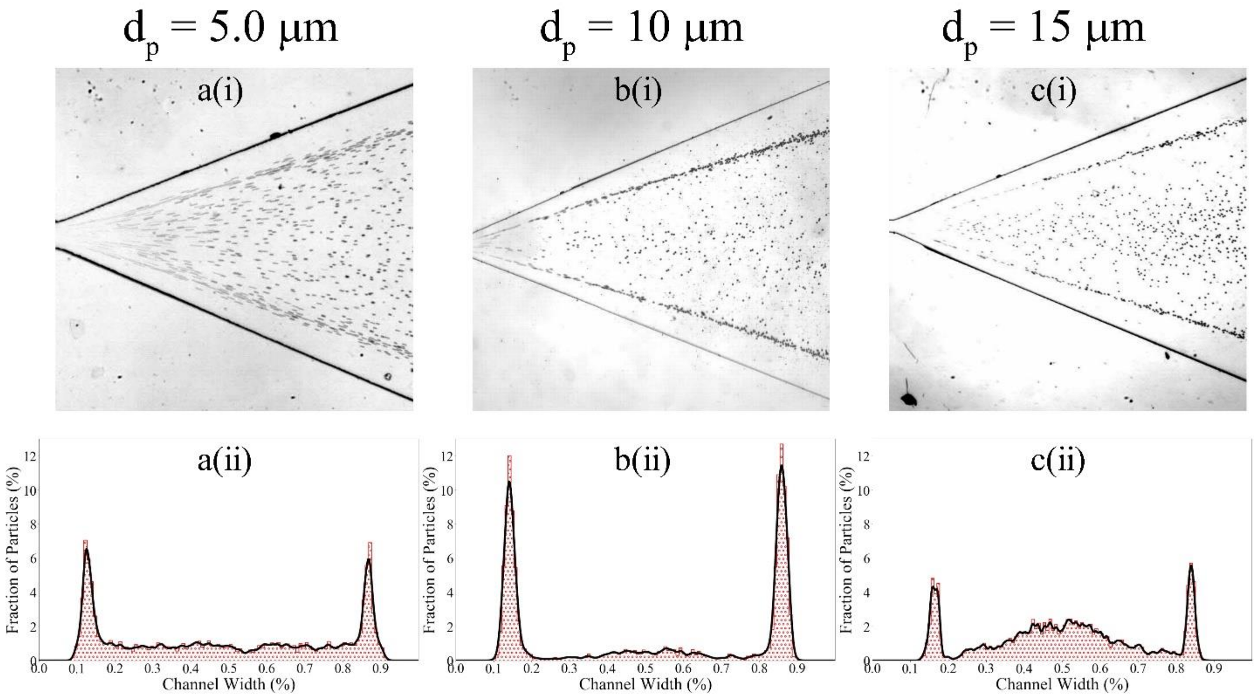

Fig. 3-23. Effect of particle size on shear-thickening focusing. Microparticles with diameters of (a) 5 µm, (b) 10 µm and (c) 15 µm were flown at 5 ml/hr in the 2.0% v/v SiO_2/Water nanofluid. Results are shown for N=1248 overlayed frames of experimental results in (i) and quantitative fraction of particles across the width of the microchannel in (ii).

It can be seen in Fig. 3-23 that the effect of particle size on the fraction of focused particles largely depended on the focusing regime that they were flowing in. In Fig. 3-23a, close to 45% of 5 µm particles were found to be focused near the two sides of the channel. $Re_{p,5}$=0.046 for this case, so the inertial effects are not dominant enough to focus these particles. The semi-focusing regime observed could be attributed to the presence of shear-thickening effects. When the particle size was increased to 10 µm (Fig. 3-23b), focusing was improved where approximately 89% of particles were seen to be focused on the same location near the two sides of the channel. As mentioned previously, $Re_{p,10}$=0.093 in this case, so the inertial focusing is week again and the hydrodynamic focusing potentially happens due to shear-thickening contributions. When we increased the particle size further to 15 µm (Fig. 3-23c), the fraction of focused particles near the two sides was found to be close to 36%, while a third week centerline focusing region started to develop. $Re_{p.15}$=0.14 in this case, so we think that the particles are slowly starting to transition from the two sides of the channel (shear-thickening focusing regions) towards the center-points of the cross section due to the growth in the inertial effects.

3.3.3 Effects of Nanofluid Concentration on Particle Focusing in Shear Thickening Fluids

For our final investigation, we studied the effect of changing the concentration, φ, of the shear-thickening SiO_2/Water nanofluid solution. Distribution of 10 μm particles flowing at 5 ml/hr in three different SiO_2 concentrations of 1%, 2% and 3% in water are shown in Fig. 3-24.

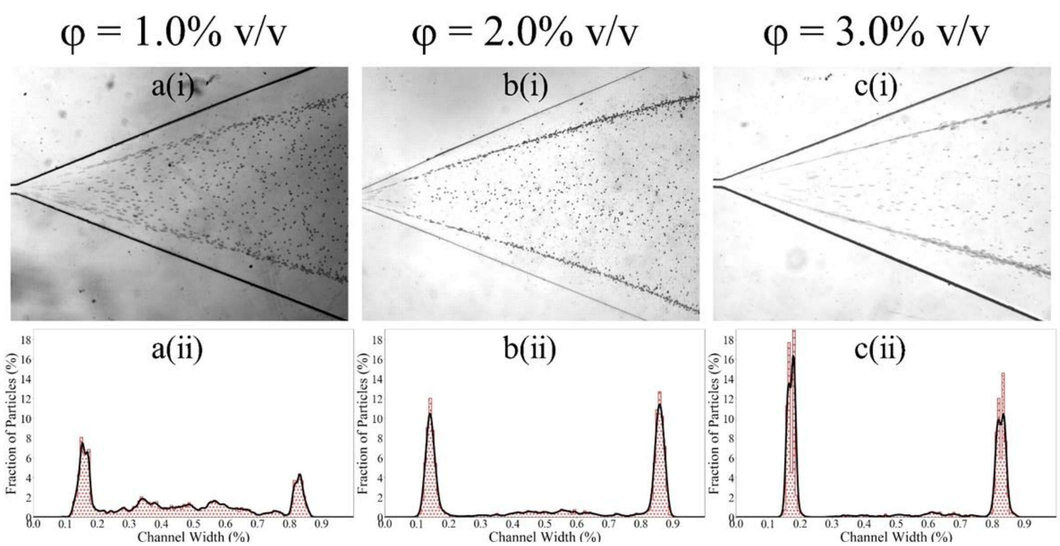

Fig. 3-24. Effects of Nanofluid concentration on shear thickening focusing. 10 μm particles flowing at 5ml/hr in different concentrations, φ, of SiO_2/Water nanofluid. (a) 1.0% v/v, (b) 2.0% v/v and (c) 3.0% v/v. Results are shown for N=1248 overlayed frames of experimental results in (i) and quantitative fraction of particles across the width of the microchannel in (ii).

As demonstrated in Fig. 3-24a-c, with increasing the concentration of the nanofluid solution, more particles were found to be focused near the two sides of the channel. At 1% v/v concentration (Fig. 3-24a), about 53% of particles were found to be focused. As the concentration was increased to 2% v/v (Fig. 3-24b) and the shear-thickening effects were enhanced, focusing was improved and approximately 89% of particles were seen to be focused near the two sides of the channel. At 3%

v/v SiO_2/Water concentration (Fig. 3-24c), the highest focusing fraction was achieved where close to 93 % of 10 μm particles were found to be focused near the two sides of the channel and the shear-thickening effects were most pronounced. It is worth mentioning that the $Re_{p,10}$ in the three concentrations of 1%, 2 and 3% in Fig. 3-24 are 0.094, 0.079 and 0.076, respectively. This shows that the inertial effects were insignificant, and observations were mostly related to the role that the shear thickening effect played in particle focusing.

Our findings in section 3.3 on microparticle focusing in shear-thickening nanofluids, flowing in a straight microchannel, are very recent and have not been published yet. These studies were all experimental. When it comes to the theoretical description of shear-thickening focusing of microparticles in microfluidics, there has not been a publication so far in the literature. This is why we mostly used the Re_p values in our discussions above, only to justify the significance of inertial forces in our experiments. We are currently seeking information on the shear thickening effects and the resulting hydrodynamic forces that may be involved in our experiments. With the help of analytical and/or theoretical studies on the nature of shear-thickening focusing of microparticles in microfluidics, a stronger theoretical description could be developed and many unknown research questions in this field could be answered in the future.

3.4 Closing Remarks

In this chapter, we reported the passive hydrodynamics of microparticles as they flow in straight microchannels, while being suspended in water, PEO-water and SiO2-water solutions as representatives of Newtonian, shear-thinning and shear-thickening fluids. In water, particles are mostly dispersed throughout the channel for the range of the parameters we studied. Some passive focusing close to the center of the side-walls of the microchannel were seen for the Newtonian DI-water which was heavily dominated by the effects of inertial forces. In PEO-water, passive focusing regime changes to a single line focusing at the center. The important factors affecting particle focusing in shear thinning PEO-water solutions are elastic and inertial lift forces. Lastly, in SiO2-water, the focusing regime changes to two side focusing lines possibly at the four corners of the microchannel. Focusing is governed strongly by the effects of shear-thickening fluid and to some extent inertial forces.

Chapter 4
THESIS SUMMARY AND FUTURE WORK

4.1 Thesis Summary

In many areas of biology, biotechnology and medicine, sorting and separation of small substances like cells, microorganisms, and micro- and nano-particles from a heterogeneous mixture are important sample preparation steps. Microfluidic particle separation has attracted attention in biotechnological applications due to their compact, inexpensive, and disposable characteristics. Biological and environmental fluids used in sample preparations can have various rheological properties including Newtonian, shear-thinning, and shear-thickening characteristics.

In this thesis, we investigated microfluidics particle hydrodynamics in Newtonian, shear-thinning, and shear-thickening non-Newtonian fluids. We used straight microfluidic platforms that were experimentally developed in our group for this study. Numerical models were developed to simulate microfluidics particle focusing in Newtonian inertia-magnetic and shear-thinning elasto-inertial regimes to satisfy the 1st and 2nd objectives defined in the thesis (section 1.3), respectively. For the 3rd objective, the straight microchannel that was developed and tested for the Newtonian and shear-thinning non-Newtonian fluids in our group [15] were employed to study particle behavior in shear-thickening non-Newtonian fluids.

For the Newtonian inertia-magnetic regime (1st Objective), after the verification and validation of the model against experimental measurements done in our group [21], we studied the effects of magnetization, particle size and fluid viscosity on the focusing quality and position of microparticles. It was found that, within the range of our studied parameters, increasing magnetization up to 1.35×10^{6} A/M would enhance focusing quality as the 11 µm particles were found to be focused in their narrowest band as magnetic saturation was achieved. Increasing particle size was also found to have a direct impact on particle exit position as larger particles concentrated further away from the channel baseline at a given flow rate. This happens due to the increased inertial forces on larger particles. The last studied parameter in the Newtonian regime was the viscosity; it was found that changing the viscosity of the fluid at a constant Reynolds number would not have a significant impact on the focusing position of microparticles. While, at a constant flow rate, increasing the viscosity of the fluid caused 11µm particles to focus at a position closer to the channel baseline. This is due to the increased drag force on particles in more viscous fluids.

The developed model in the 1st objective was then modified and expanded to include the viscoelastic effects of shear-thinning non-Newtonian fluids for the 2nd objective. This model was also verified and validated by both experimental measurements in our group [15] and the available works in the literature [23]. A parametric study based on the Buckingham Π theorem was developed to study the impact of relevant non-dimensional numbers on elasto-inertial focusing. It was found that focusing is improved with the increase in viscoelasticity, particle diameter, flow velocity and channel length. However, channel hydraulic diameter had an inverse effect on elasto-inertial focusing. Moreover, the effects of Blockage ratio, Deborah and Reynolds numbers were found to be more pronounced on focusing. Based on the non-dimensional investigation, two focusing regions were identified where particles were found to be dispersed no more than the 20% of the channel width when $De>0.4$ and $\beta>0.05$, or $Re>3$ and $\beta>0.05$. The earlier proposed threshold for elasto-inertial particle focusing in straight microchannels of square cross section [23] was modified to reflect the impacts of all effective non-dimensional numbers. The new proposed threshold by us ($\sigma = \mathrm{De} \cdot \mathrm{Re}^{0.2} \cdot \mathrm{L} \cdot \beta^2 = 5$) includes the effect of Reynolds number and assumed a focusing line with dispersion of less than 3%. Finally, an empirical correlation was developed to predict the elasto-inertial dispersion of microparticles in microchannels of square cross section.

As for our final objective, the straight microfluidic device that was experimentally tested for Newtonian and shear-thinning non-Newtonian fluids in our group [15] and numerically modeled in the 2nd objective of this thesis were used to experimentally investigate particle focusing in shear-thickening non-Newtonian SiO_2/water nanofluid for the first time. We observed two side focusing lines for microparticles flowing in shear-thickening SiO_2/water nanofluid. This was a different behavior compared to the Newtonian DI-Water (no focusing) and shear-thinning PEO solutions (1 center line focusing). Furthermore, we found that increasing the concentration of SiO_2/water up to 3.0 v/v % would improve focusing of particles as 93% of 10μm particles were found to be focused in the channel. The effects of flow rate and particle size on fraction of focused particles in shear-thickening regime was also studied. It was found that, within the range of our studied parameters, 10 μm particles flowing at 5 ml/hr would provide the highest focusing quality as 89% of the particles were found to be focused close to the two side walls of the channel.

This thesis and its findings provide an understanding on significant parameters affecting microfluidics particle focusing in Newtonian, shear-thinning and shear-thickening fluids. The presented numerical models could serve as accessible and reliable tools to simulate Newtonian and non-Newtonian shear-thinning microfluidic platforms. The proposed design threshold for elasto-inertial focusing and the predictive correlations can optimize the design of viscoelastic particle sorters and facilitate experimental designs. The experimental findings on particle focusing in shear-thickening fluids can serve as the dataset needed to develop and validate a numerical model for these fluids and expand the fundamental studies in this field in the future.

4.2 Limitations of the Thesis and Proposed Future Work

There has been some challenges and limitations that has impacted this research that must be mentioned. The proposed numerical modeling scheme, though being validated by the experimental study, still has room to enhance accuracy in predicting particle positions. Aside from human and instrument errors, one major source of error would be the position of the magnet. Even though the magnet is reported to be fixed in the experimental setup, with the slightest change in the location or orientation of the magnet, the magnetic field experienced by the particles and their trajectories could be affected. This can become a source of error in the simulation as well. Another limitation of the current numerical modeling is that it does not consider particle-particle interactions. Even though Tween 20 is used in the experiments to ensure the homogeneity of particle samples and avoid problems such as particle agglomeration and sedimentation, this can introduce some inaccuracy into our simulations. Finally, the experimental shear-thickening focusing study is preliminary at this stage. The theoretical descriptions and analysis are largely missing due to the lack of time to acquire enough knowledge on particle hydrodynamics in shear-thickening fluids. This has limited the depth and breadth of this study especially on the theoretical description and justification of the experimental observations.

For continuing this project, the following ideas and suggestions are recommended for further investigation.

The proposed numerical models for particle hydrodynamics in Newtonian and non-Newtonian fluids were verified and validated for straight microchannels. These models could now be further developed to be used for more complex geometries such as curved and spiral channels. As these geometries would introduce new forces on the particles, such as dean drag force in curved channels, the modeling scheme would also need to be matured to account for these effects and their combination with inertial and elastic lift forces. With the help of such model, new experimental designs can be simulated and possibly optimized for further applications.

Furthermore, based on the results from the particle behaviour in Newtonian inertia-magnetic regime, an optimum magnetization value of 1.35×10^6 A/M was identified for the experimental setup. Some design modifications could be considered to accommodate even a weaker magnet, with the same length, in this microfluidic setup to achieve similar results. At lower magnetization values of 4.5×10^5 A/m, increasing the length of the magnet may also allow the particles to better focus along the channel sidewall before entering the expansion zone.

The experimental elasto-inertial device developed in our group could further be optimized using our proposed predictive equation (Eq. 13). The deflection of particles could be customized based on this equation allowing for easier multiplexing of developed microfluidic sorters. Moreover, similar non-dimensional analysis and design thresholds could be developed to predict and customize particle focusing in curved channels.

As mentioned in section 3.3, the theoretical descriptions on shear thickening mechanism are scarce in the literature. The current experimental observations on shear-thickening focusing could be explained and justified by way of non-dimensional numbers similar to the Wi or De numbers in shear-thinning viscoelastic fluids. A fundamental theoretical study on microfluidics particle focusing in shear thickening fluids can follow up. Finally, the shear thickening effects on particle focusing can further be explored in different geometries and/or be combined with other passive and active methods to develop hybrid microfluidic particle sorters.

REFERENCES

1. Beech, J.P., P. Jönsson, and J.O. Tegenfeldt, *Tipping the balance of deterministic lateral displacement devices using dielectrophoresis.* Lab on a Chip, 2009. **9**(18): p. 2698-2706.
2. Davis, J.A., et al., *Deterministic hydrodynamics: taking blood apart.* Proceedings of the National Academy of Sciences, 2006. **103**(40): p. 14779-14784.
3. Yamada, M., M. Nakashima, and M. Seki, *Pinched flow fractionation: continuous size separation of particles utilizing a laminar flow profile in a pinched microchannel.* Analytical chemistry, 2004. **76**(18): p. 5465-5471.
4. Vig, A.L. and A. Kristensen, *Separation enhancement in pinched flow fractionation.* Applied Physics Letters, 2008. **93**(20): p. 203507.
5. Zhou, J. and I. Papautsky, *Fundamentals of inertial focusing in microchannels*. Lab on a Chip, 2013. **13**(6): p. 1121-1132.
6. Zhou, J., et al., *Modulation of aspect ratio for complete separation in an inertial microfluidic channel.* Lab on a Chip, 2013. **13**(10): p. 1919-1929.
7. Wang, X., et al., *A disposable, roll-to-roll hot-embossed inertial microfluidic device for size-based sorting of microbeads and cells.* Lab on a Chip, 2016. **16**(10): p. 1821-1830.
8. Wang, X. and I. Papautsky, *Size-based microfluidic multimodal microparticle sorter.* Lab on a Chip, 2015. **15**(5): p. 1350-1359.
9. Pamme, N. and A. Manz, *On-chip free-flow magnetophoresis: continuous flow separation of magnetic particles and agglomerates.* Analytical chemistry, 2004. **76**(24): p. 7250-7256.
10. Kumar, V. and P. Rezai, *Multiplex Inertio-Magnetic Fractionation (MIMF) of magnetic and non-magnetic microparticles in a microfluidic device.* Microfluidics and Nanofluidics, 2017. **21**(5): p. 83.
11. Yang, S., et al., *Sheathless elasto-inertial particle focusing and continuous separation in a straight rectangular microchannel.* Lab on a Chip, 2011. **11**(2): p. 266-273.
12. Faridi, M.A., et al., *Elasto-inertial microfluidics for bacteria separation from whole blood for sepsis diagnostics.* Journal of nanobiotechnology, 2017. **15**(1): p. 3.
13. Li, Y., et al., *Dynamic control of particle separation in deterministic lateral displacement separator with viscoelastic fluids.* Scientific reports, 2018. **8**(1): p. 1-9.
14. Lu, X. and X. Xuan, *Continuous microfluidic particle separation via elasto-inertial pinched flow fractionation.* Analytical chemistry, 2015. **87**(12): p. 6389-6396.
15. Dibaji, S. and P. Rezai, *Triplex Inertia-Magneto-Elastic (TIME) sorting of microparticles in non-Newtonian fluids.* Journal of Magnetism and Magnetic Materials, 2020. **503**: p. 166620.
16. Liu, X.-Q., et al., *Temperature induced gelation transition of a fumed silica/PEG shear thickening fluid.* Rsc Advances, 2015. **5**(24): p. 18367-18374.
17. Moldoveanu, G.M., et al., *Viscosity estimation of Al2O3, SiO2 nanofluids and their hybrid: an experimental study*. Journal of Molecular Liquids, 2018. **253**: p. 188-196.
18. Gu, C., et al., *Shear thickening effects of drag-reducing nanofluids for low permeability reservoir.* Advances in Geo-Energy Research, 2020. **4**(3): p. 317-325.
19. Lee, Y.K. and K.H. Ahn, *A novel lattice Boltzmann method for the dynamics of rigid particles suspended in a viscoelastic medium.* Journal of Non-Newtonian Fluid Mechanics, 2017. **244**: p. 75-84.

20. Raoufi, M.A., et al., *Experimental and numerical study of elasto-inertial focusing in straight channels.* Biomicrofluidics, 2019. **13**(3): p. 034103.
21. Kumar, V. and P. Rezai, *Magneto-Hydrodynamic Fractionation (MHF) for continuous and sheathless sorting of high-concentration paramagnetic microparticles.* Biomedical microdevices, 2017. **19**(2): p. 39.
22. Fu, T., et al., *Newtonian and Non-Newtonian Flows in Microchannels: Inline Rheological Characterization.* Chemical Engineering & Technology, 2016. **39**(5): p. 987-992.
23. Del Giudice, F., et al., *Particle alignment in a viscoelastic liquid flowing in a square-shaped microchannel.* Lab on a Chip, 2013. **13**(21): p. 4263-4271.
24. Abu Hammad, O., et al. *Factors influencing global variations in COVID-19 cases and fatalities; a review*. in *Healthcare*. 2020. Multidisciplinary Digital Publishing Institute.
25. Majors, C.E., et al., *Point-of-care diagnostics to improve maternal and neonatal health in low-resource settings.* Lab on a Chip, 2017. **17**(20): p. 3351-3387.
26. Lee, W.G., et al., *Nano/Microfluidics for diagnosis of infectious diseases in developing countries.* Advanced drug delivery reviews, 2010. **62**(4-5): p. 449-457.
27. Saliba, A.-E., et al., *Microfluidic sorting and multimodal typing of cancer cells in self-assembled magnetic arrays.* Proceedings of the National Academy of Sciences, 2010. **107**(33): p. 14524-14529.
28. Yilmaz, S. and A.K. Singh, *Single cell genome sequencing.* Current opinion in biotechnology, 2012. **23**(3): p. 437-443.
29. Podar, M., et al., *Targeted access to the genomes of low-abundance organisms in complex microbial communities.* Applied and environmental microbiology, 2007. **73**(10): p. 3205-3214.
30. Andersson, H. and A. Van den Berg, *Microfluidic devices for cellomics: a review.* Sensors and actuators B: Chemical, 2003. **92**(3): p. 315-325.
31. Cheng, C., et al., *Au nanocluster-embedded chitosan nanocapsules as labels for the ultrasensitive fluorescence immunoassay of Escherichia coli O157:H7.* Analyst, 2018. **143**(17): p. 4067-4073.
32. Mach, A.J., O.B. Adeyiga, and D. Di Carlo, *Microfluidic sample preparation for diagnostic cytopathology*. Lab on a Chip, 2013. **13**(6): p. 1011-1026.
33. Leshansky, A.M., et al., *Tunable nonlinear viscoelastic "focusing" in a microfluidic device.* Physical review letters, 2007. **98**(23): p. 234501.
34. Dharmasiri, U., et al., *Microsystems for the capture of low-abundance cells.* Annual review of analytical chemistry, 2010. **3**: p. 409-431.
35. Clark, K.D., C. Zhang, and J.L. Anderson, *Sample preparation for bioanalytical and pharmaceutical analysis*. 2016, ACS Publications.
36. Jung, W., et al., *Point-of-care testing (POCT) diagnostic systems using microfluidic lab-on-a-chip technologies.* Microelectronic Engineering, 2015. **132**: p. 46-57.
37. Mauk, M., et al., *Miniaturized devices for point of care molecular detection of HIV.* Lab on a Chip, 2017. **17**(3): p. 382-394.
38. Julius, M., T. Masuda, and L. Herzenberg, *Demonstration that antigen-binding cells are precursors of antibody-producing cells after purification with a fluorescence-activated cell sorter*. Proceedings of the National Academy of Sciences, 1972. **69**(7): p. 1934-1938.
39. Geens, M., et al., *The efficiency of magnetic-activated cell sorting and fluorescence-activated cell sorting in the decontamination of testicular cell suspensions in cancer patients.* Human Reproduction, 2006. **22**(3): p. 733-742.

40. Adams, J.D., U. Kim, and H.T. Soh, *Multitarget magnetic activated cell sorter.* Proceedings of the National Academy of Sciences of the United States of America, 2008. **105**(47): p. 18165-18170.
41. Gubala, V., et al., *Point of care diagnostics: status and future.* Analytical chemistry, 2012. **84**(2): p. 487-515.
42. Yager, P., G.J. Domingo, and J. Gerdes, *Point-of-care diagnostics for global health.* Annu. Rev. Biomed. Eng., 2008. **10**: p. 107-144.
43. Nagrath, S., et al., *Isolation of rare circulating tumour cells in cancer patients by microchip technology.* Nature, 2007. **450**(7173): p. 1235.
44. Chen, J., J. Li, and Y. Sun, *Microfluidic approaches for cancer cell detection, characterization, and separation.* Lab on a Chip, 2012. **12**(10): p. 1753-1767.
45. Lee, M.G., et al., *Label-free cancer cell separation from human whole blood using inertial microfluidics at low shear stress.* Analytical chemistry, 2013. **85**(13): p. 6213-6218.
46. Pappas, D., *Microfluidics and cancer analysis: cell separation, cell/tissue culture, cell mechanics, and integrated analysis systems.* Analyst, 2016. **141**(2): p. 525-535.
47. Ozkumur, E., et al., *Inertial focusing for tumor antigen–dependent and–independent sorting of rare circulating tumor cells.* Science translational medicine, 2013. **5**(179): p. 179ra47-179ra47.
48. Karabacak, N.M., et al., *Microfluidic, marker-free isolation of circulating tumor cells from blood samples.* Nature protocols, 2014. **9**(3): p. 694.
49. Dalili, A., E. Samiei, and M. Hoorfar, *A review of sorting, separation and isolation of cells and microbeads for biomedical applications: microfluidic approaches.* Analyst, 2019. **144**(1): p. 87-113.
50. Ng, A.H., U. Uddayasankar, and A.R. Wheeler, *Immunoassays in microfluidic systems.* Analytical bioanalytical chemistry, 2010. **397**(3): p. 991-1007.
51. Ramadan, Q., et al., *Flow-through immunomagnetic separation system for waterborne pathogen isolation and detection: Application to Giardia and Cryptosporidium cell isolation.* Analytica chimica acta, 2010. **673**(1): p. 101-108.
52. Richardson, S.D. and T.A. Ternes, *Water analysis: emerging contaminants and current issues.* Analytical chemistry, 2011. **83**(12): p. 4614-4648.
53. Bayat, P. and P. Rezai, *Microfluidic curved-channel centrifuge for solution exchange of target microparticles and their simultaneous separation from bacteria.* Soft Matter, 2018. **14**(26): p. 5356-5363.
54. Jiang, Y., S. Zou, and X. Cao, *Rapid and ultra-sensitive detection of foodborne pathogens by using miniaturized microfluidic devices: a review.* Analytical Methods, 2016. **8**(37): p. 6668-6681.
55. Baker, C.A., et al., *Recent advances in microfluidic detection systems.* Bioanalysis, 2009. **1**(5): p. 967-975.
56. Bélanger, M.C. and Y. Marois, *Hemocompatibility, biocompatibility, inflammatory and in vivo studies of primary reference materials low-density polyethylene and polydimethylsiloxane: A review.* Journal of Biomedical Materials Research, 2001. **58**(5): p. 467-477.
57. Cui, F., et al., *Microfluidic sample preparation for medical diagnostics.* Annual review of biomedical engineering, 2015. **17**: p. 267-286.

58. Wyatt Shields Iv, C., C.D. Reyes, and G.P. López, *Microfluidic cell sorting: a review of the advances in the separation of cells from debulking to rare cell isolation.* Lab on a Chip, 2015. **15**(5): p. 1230-1249.
59. Huang, L.R., et al., *Continuous particle separation through deterministic lateral displacement.* Science, 2004. **304**(5673): p. 987-990.
60. Zhang, J., et al., *Fundamentals and applications of inertial microfluidics: A review.* Lab on a Chip, 2016. **16**(1): p. 10-34.
61. McGrath, J., M. Jimenez, and H. Bridle, *Deterministic lateral displacement for particle separation: a review.* Lab on a Chip, 2014. **14**(21): p. 4139-4158.
62. Bhagat, A.A.S., S.S. Kuntaegowdanahalli, and I. Papautsky, *Continuous particle separation in spiral microchannels using dean flows and differential migration.* Lab on a Chip, 2008. **8**(11): p. 1906-1914.
63. Di Carlo, D., *Inertial microfluidics.* Lab on a Chip, 2009. **9**(21): p. 3038-3046.
64. Martel, J.M. and M. Toner, *Inertial focusing in microfluidics.* Annual review of biomedical engineering, 2014. **16**: p. 371-396.
65. Bijarchi, M.A., et al., *Experimental investigation of on-demand ferrofluid droplet generation in microfluidics using a Pulse-Width Modulation magnetic field with proposed correlation.* Sensors and Actuators B: Chemical, 2021. **329**: p. 129274.
66. Guo, J., et al., *Auto-affitech: an automated ligand binding affinity evaluation platform using digital microfluidics with a bidirectional magnetic separation method.* Lab on a Chip, 2020. **20**(9): p. 1577-1585.
67. Zhang, Y. and X. Chen, *Blood cells separation microfluidic chip based on dielectrophoretic force.* Journal of the Brazilian Society of Mechanical Sciences and Engineering, 2020. **42**(4): p. 1-11.
68. Kwizera, E.A., et al., *Methods of Generating Dielectrophoretic Force for Microfluidic Manipulation of Bioparticles.* ACS Biomaterials Science & Engineering, 2021.
69. Zhao, H., et al., *Continuous optical sorting of nanoscale biomolecules in integrated microfluidic-nanophotonic chips.* Sensors and Actuators B: Chemical, 2021. **331**: p. 129428.
70. Sun, L., et al., *Dynamic fabrication of microfluidic systems for particles separation based on optical projection lithography.* Biomedical Microdevices, 2020. **22**(4): p. 1-7.
71. Sajeesh, P. and A.K. Sen, *Particle separation and sorting in microfluidic devices: a review.* Microfluidics and Nanofluidics, 2014. **17**(1): p. 1-52.
72. Saeed, O.O., R. Li, and Y. Deng, *Microfluidic approaches for cancer cell separation.* Journal of Biomedical Science Engineering, 2014. **7**(12): p. 1005.
73. Inglis, D.W., et al., *Continuous microfluidic immunomagnetic cell separation.* Applied Physics Letters, 2004. **85**(21): p. 5093-5095.
74. Hejazian, M., W. Li, and N.-T. Nguyen, *Lab on a chip for continuous-flow magnetic cell separation.* Lab on a Chip, 2015. **15**(4): p. 959-970.
75. Ngamsom, B., et al., *Multiplex sorting of foodborne pathogens by on-chip free-flow magnetophoresis.* Analytica chimica acta, 2016. **918**: p. 69-76.
76. Golozar, M., M. Molki, and J. Darabi, *Computational and performance analysis of a continuous magnetophoretic bioseparation chip with alternating magnetic fields.* Microfluidics and Nanofluidics, 2017. **21**(4): p. 73.
77. Alnaimat, F., et al., *Microfluidics based magnetophoresis: A review.* The Chemical Record, 2018. **18**(11): p. 1596-1612.

78. Adams, J.D., U. Kim, and H.T. Soh, *Multitarget magnetic activated cell sorter.* Proceedings of the National Academy of Sciences, 2008. **105**(47): p. 18165-18170.
79. Xia, N., et al., *Combined microfluidic-micromagnetic separation of living cells in continuous flow.* Biomedical microdevices, 2006. **8**(4): p. 299.
80. Phurimsak, C., et al., *On-chip determination of C-reactive protein using magnetic particles in continuous flow.* Analytical chemistry, 2014. **86**(21): p. 10552-10559.
81. Pamme, N., J.C. Eijkel, and A. Manz, *On-chip free-flow magnetophoresis: Separation and detection of mixtures of magnetic particles in continuous flow.* Journal of magnetism and magnetic materials, 2006. **307**(2): p. 237-244.
82. Tarn, M.D., et al., *The importance of particle type selection and temperature control for on-chip free-flow magnetophoresis.* Journal of magnetism and magnetic materials, 2009. **321**(24): p. 4115-4122.
83. Gossett, D.R., et al., *Label-free cell separation and sorting in microfluidic systems.* Analytical and bioanalytical chemistry, 2010. **397**(8): p. 3249-3267.
84. Haynes, R.H. and A.C. Burton, *Role of the non-Newtonian behavior of blood in hemodynamics.* American Journal of Physiology-Legacy Content, 1959. **197**(5): p. 943-950.
85. Rantonen, P.J. and J.H. Meurman, *Viscosity of whole saliva.* Acta Odontologica Scandinavica, 1998. **56**(4): p. 210-214.
86. Robins, A., *Non-newtonian behaviour of dilute DNA solutions.* Transactions of the Faraday Society, 1964. **60**: p. 1344-1351.
87. Morison, K.R., J.P. Phelan, and C.G. Bloore, *Viscosity and non-Newtonian behaviour of concentrated milk and cream.* International journal of food properties, 2013. **16**(4): p. 882-894.
88. Lu, X., et al., *Particle manipulations in non-Newtonian microfluidics: A review.* Journal of colloid and interface science, 2017. **500**: p. 182-201.
89. D'Avino, G., et al., *Single line particle focusing induced by viscoelasticity of the suspending liquid: theory, experiments and simulations to design a micropipe flow-focuser.* Lab on a Chip, 2012. **12**(9): p. 1638-1645.
90. Lee, D.J., et al., *Multiplex particle focusing via hydrodynamic force in viscoelastic fluids.* Scientific reports, 2013. **3**: p. 3258.
91. Li, D., X. Lu, and X. Xuan, *Viscoelastic separation of particles by size in straight rectangular microchannels: a parametric study for a refined understanding.* Analytical chemistry, 2016. **88**(24): p. 12303-12309.
92. Lim, E.J., et al., *Inertio-elastic focusing of bioparticles in microchannels at high throughput.* Nature communications, 2014. **5**(1): p. 1-9.
93. Lim, H., J. Nam, and S. Shin, *Lateral migration of particles suspended in viscoelastic fluids in a microchannel flow.* Microfluidics and nanofluidics, 2014. **17**(4): p. 683-692.
94. d'Avino, G., et al., *Viscoelasticity-induced migration of a rigid sphere in confined shear flow.* Journal of Non-Newtonian Fluid Mechanics, 2010. **165**(9-10): p. 466-474.
95. Nam, J., et al., *Hybrid capillary-inserted microfluidic device for sheathless particle focusing and separation in viscoelastic flow.* Biomicrofluidics, 2015. **9**(6): p. 064117.
96. D'Avino, G., F. Greco, and P.L. Maffettone, *Particle migration due to viscoelasticity of the suspending liquid and its relevance in microfluidic devices.* Annual Review of Fluid Mechanics, 2017. **49**: p. 341-360.

97. Karimi, A., S. Yazdi, and A. Ardekani, *Hydrodynamic mechanisms of cell and particle trapping in microfluidics.* Biomicrofluidics, 2013. **7**(2): p. 021501.
98. Boersma, W.H., J. Laven, and H.N. Stein, *Viscoelastic properties of concentrated shear-thickening dispersions.* Journal of colloid and interface science, 1992. **149**(1): p. 10-22.
99. Fischer, C., et al., *Structures with adaptive stiffness and damping integrating shear thickening fluids*. 2009.
100. Wasserman, S.H., et al., *Cable comprising a shear thickening composition*. 2011, Google Patents.
101. Decker, M., et al., *Stab resistance of shear thickening fluid (STF)-treated fabrics.* Composites science and technology, 2007. **67**(3-4): p. 565-578.
102. Barnes, H.A., J.F. Hutton, and K. Walters, *An introduction to rheology*. Vol. 3. 1989: Elsevier.
103. Wagner, N.J. and J.F. Brady, *Shear thickening in colloidal dispersions.* Physics Today, 2009. **62**(10): p. 27-32.
104. Zhang, X., W. Li, and X. Gong, *The rheology of shear thickening fluid (STF) and the dynamic performance of an STF-filled damper.* Smart Materials and Structures, 2008. **17**(3): p. 035027.
105. Zhang, X., W. Li, and X. Gong, *Study on magnetorheological shear thickening fluid.* Smart materials and structures, 2008. **17**(1): p. 015051.
106. Chellamuthu, M., E.M. Arndt, and J.P. Rothstein, *Extensional rheology of shear-thickening nanoparticle suspensions.* Soft Matter, 2009. **5**(10): p. 2117-2124.
107. Ding, J., et al., *Review on shear thickening fluids and applications.* 2013.
108. Hoffman, R., *Discontinuous and dilatant viscosity behavior in concentrated suspensions. I. Observation of a flow instability*. Transactions of the Society of Rheology, 1972. **16**(1): p. 155-173.
109. Hoffman, R., *Discontinuous and dilatant viscosity behavior in concentrated suspensions. II. Theory and experimental tests.* Journal of Colloid and Interface Science, 1974. **46**(3): p. 491-506.
110. Hoffman, R.L., *Discontinuous and dilatant viscosity behavior in concentrated suspensions III. Necessary conditions for their occurrence in viscometric flows.* Advances in colloid and interface science, 1982. **17**(1): p. 161-184.
111. Bender, J.W. and N.J. Wagner, *Optical measurement of the contributions of colloidal forces to the rheology of concentrated suspensions.* Journal of colloid and interface science, 1995. **172**(1): p. 171-184.
112. Bossis, G. and J. Brady, *The rheology of Brownian suspensions.* The Journal of chemical physics, 1989. **91**(3): p. 1866-1874.
113. Petel, O.E., et al., *The effect of particle strength on the ballistic resistance of shear thickening fluids.* Applied Physics Letters, 2013. **102**(6): p. 064103.
114. Choi, S.U. and J.A. Eastman, *Enhancing thermal conductivity of fluids with nanoparticles*. 1995, Argonne National Lab., IL (United States).
115. Chen, H., Y. Ding, and C. Tan, *Rheological behaviour of nanofluids.* New journal of physics, 2007. **9**(10): p. 367.
116. Sharma, A.K., A.K. Tiwari, and A.R. Dixit, *Rheological behaviour of nanofluids: a review.* Renewable and Sustainable Energy Reviews, 2016. **53**: p. 779-791.

117. Matsuoka, Y., Y. Nakayama, and T. Kajiwara, *Prediction of shear thickening of particle suspensions in viscoelastic fluids by direct numerical simulation.* Journal of Fluid Mechanics, 2021. **913**.
118. Matsuoka, Y., Y. Nakayama, and T. Kajiwara, *Effects of viscoelasticity on shear-thickening in dilute suspensions in a viscoelastic fluid.* Soft matter, 2020. **16**(3): p. 728-737.
119. Bazaz, S.R., et al., *Computational inertial microfluidics: a review.* Lab on a Chip, 2020. **20**(6): p. 1023-1048.
120. Matas, J.-P., J.F. Morris, and É. Guazzelli, *Inertial migration of rigid spherical particles in Poiseuille flow*. Journal of Fluid Mechanics, 2004. **515**: p. 171-195.
121. Yang, B.H., et al., *Migration of a sphere in tube flow.* Journal of Fluid mechanics, 2005. **540**: p. 109-131.
122. Feng, J., H.H. Hu, and D.D. Joseph, *Direct simulation of initial value problems for the motion of solid bodies in a Newtonian fluid Part 1. Sedimentation.* Journal of Fluid Mechanics, 1994. **261**: p. 95-134.
123. Feng, J., H.H. Hu, and D.D. Joseph, *Direct simulation of initial value problems for the motion of solid bodies in a Newtonian fluid. Part 2. Couette and Poiseuille flows.* Journal of fluid mechanics, 1994. **277**: p. 271-301.
124. Modak, N., A. Datta, and R. Ganguly, *Cell separation in a microfluidic channel using magnetic microspheres.* Microfluidics and Nanofluidics, 2009. **6**(5): p. 647.
125. Telleman, P., et al. *Cell sorting in microfluidic systems*. in *Micro Total Analysis Systems' 98*. 1998. Springer.
126. Krishnan, J.N., et al., *Rapid microfluidic separation of magnetic beads through dielectrophoresis and magnetophoresis.* Electrophoresis, 2009. **30**(9): p. 1457-1463.
127. Amin, A., *High throughput particle separation using differential fermat spiral microchannel with variable channel width*, in *Mechanical Engineering*. 2014, University of Akron: University of Akron.
128. Parrott, C., *Computational Fluid Dynamics (CFD) Simulation of Microfluidic Focusing in a Low-Cost Flow Cytometer*, in *Mechanical Engineering*. 2017, Oregon State University: Oregon State University.
129. Yang, R.-J., et al., *Micro-magnetofluidics in microfluidic systems: A review.* Sensors and Actuators B: Chemical, 2016. **224**: p. 1-15.
130. Nandy, K., et al., *Analytical model for the magnetophoretic capture of magnetic microspheres in microfluidic devices.* Journal of Magnetism and Magnetic Materials, 2008. **320**(7): p. 1398-1405.
131. Zhu, T., et al., *Analytical model of microfluidic transport of non-magnetic particles in ferrofluids under the influence of a permanent magnet.* Microfluidics and Nanofluidics, 2011. **10**(6): p. 1233-1245.
132. Modak, N., et al., *Experimental and numerical characterization of magnetophoretic separation for MEMS-based biosensor applications.* Biomedical microdevices, 2010. **12**(1): p. 23-34.
133. Zolgharni, M., et al., *A numerical design study of chaotic mixing of magnetic particles in a microfluidic bio-separator.* Microfluidics and Nanofluidics, 2007. **3**(6): p. 677-687.
134. Forbes, T.P. and S.P. Forry, *Microfluidic magnetophoretic separations of immunomagnetically labeled rare mammalian cells.* Lab on a Chip, 2012. **12**(8): p. 1471-1479.

135. Hale, C. and J. Darabi, *Magnetophoretic-based microfluidic device for DNA isolation.* Biomicrofluidics, 2014. **8**(4): p. 044118.
136. Kim, M.J., et al., *Two step label free particle separation in a microfluidic system using elasto-inertial focusing and magnetophoresis.* RSC advances, 2016. **6**(38): p. 32090-32097.
137. Trofa, M., et al., *Numerical simulations of the competition between the effects of inertia and viscoelasticity on particle migration in Poiseuille flow.* Computers & Fluids, 2015. **107**: p. 214-223.
138. Lebas, R., et al., *Numerical simulation of primary break-up and atomization: DNS and modelling study.* International Journal of Multiphase Flow, 2009. **35**(3): p. 247-260.
139. Moghadam, M.C., A. Eilaghi, and P. Rezai, *Inertia-magnetic particle sorting in microfluidic devices: a numerical parametric investigation.* Microfluidics and Nanofluidics, 2019. **23**(12): p. 135.
140. Charjouei Moghadam, M., A. Eilaghi, and P. Rezai, *Elasto-inertial microparticle focusing in straight microchannels: A numerical parametric investigation.* Physics of Fluids, 2021. **33**(9): p. 092002.
141. Incropera, F. and D. DeWitt, *Introduction to heat transfer.* 1985.
142. Ebagninin, K.W., A. Benchabane, and K. Bekkour, *Rheological characterization of poly (ethylene oxide) solutions of different molecular weights.* Journal of colloid and interface science, 2009. **336**(1): p. 360-367.
143. Cho, K.S., K.-W. Song, and G.-S. Chang, *Scaling relations in nonlinear viscoelastic behavior of aqueous PEO solutions under large amplitude oscillatory shear flow.* Journal of Rheology, 2010. **54**(1): p. 27-63.
144. Sharifi, A. and M.C. Moghadam, *CFD simulation of blood flow inside the corkscrew collaterals of the Buerger's disease.* BioImpacts: BI, 2016. **6**(1): p. 41.
145. Sharifi, A., et al., *Numerical simulation of blood flow in intracranial aneurysms treated by endovascular Woven EndoBridge technique.* International Journal of Modern Physics C (IJMPC), 2020. **31**(05): p. 1-14.
146. Ounis, H., G. Ahmadi, and J.B. McLaughlin, *Brownian diffusion of submicrometer particles in the viscous sublayer.* Journal of Colloid Interface Science, 1991. **143**(1): p. 266-277.
147. Tian, F., et al., *Microfluidic co-flow of Newtonian and viscoelastic fluids for high-resolution separation of microparticles.* Lab on a Chip, 2017. **17**(18): p. 3078-3085.
148. Bush, M. and N. Phan-Thien, *Drag force on a sphere in creeping motion throug a carreau model fluid.* Journal of non-newtonian fluid mechanics, 1984. **16**(3): p. 303-313.
149. Chhabra, R., P. Uhlherr, and D. Boger, *The influence of fluid elasticity on the drag coefficient for creeping flow around a sphere.* Journal of Non-Newtonian Fluid Mechanics, 1980. **6**(3-4): p. 187-199.
150. Ho, B. and L. Leal, *Inertial migration of rigid spheres in two-dimensional unidirectional flows.* Journal of fluid mechanics, 1974. **65**(2): p. 365-400.
151. Ho, B. and L. Leal, *Migration of rigid spheres in a two-dimensional unidirectional shear flow of a second-order fluid.* Journal of fluid mechanics, 1976. **76**(4): p. 783-799.
152. Pathak, J.A., D. Ross, and K.B. Migler, *Elastic flow instability, curved streamlines, and mixing in microfluidic flows.* Physics of fluids, 2004. **16**(11): p. 4028-4034.
153. Yuan, D., et al., *Recent progress of particle migration in viscoelastic fluids.* Lab on a Chip, 2018. **18**(4): p. 551-567.

154. Magda, J., et al., *Second normal stress difference of a Boger fluid.* Polymer, 1991. **32**(11): p. 2000-2009.
155. Morozov, A. and S.E. Spagnolie, *Introduction to complex fluids*, in *Complex fluids in biological systems*. 2015, Springer. p. 3-52.
156. D'Avino, G. and P.L. Maffettone, *Particle dynamics in viscoelastic liquids.* Journal of Non-Newtonian Fluid Mechanics, 2015. **215**: p. 80-104.
157. Tirtaatmadja, V., G.H. McKinley, and J.J. Cooper-White, *Drop formation and breakup of low viscosity elastic fluids: Effects of molecular weight and concentration.* Physics of fluids, 2006. **18**(4): p. 043101.
158. Graessley, W.W., *Polymer chain dimensions and the dependence of viscoelastic properties on concentration, molecular weight and solvent power.* Polymer, 1980. **21**(3): p. 258-262.
159. Rodd, L.E., et al., *The inertio-elastic planar entry flow of low-viscosity elastic fluids in micro-fabricated geometries.* Journal of Non-Newtonian Fluid Mechanics, 2005. **129**(1): p. 1-22.
160. Xia, Y. and G. Whitesides, *Angew. soft lithography.* Chem. Int. Ed. Engl, 1998. **37**(5): p. 550-575.
161. Eyal, S. and S.R. Quake, *Velocity-independent microfluidic flow cytometry.* Electrophoresis, 2002. **23**(16): p. 2653-2657.
162. Shardt, O., S.K. Mitra, and J. Derksen, *Lattice Boltzmann simulations of pinched flow fractionation.* Chemical engineering science, 2012. **75**: p. 106-119.
163. Mach, A.J. and D. Di Carlo, *Continuous scalable blood filtration device using inertial microfluidics.* Biotechnology and bioengineering, 2010. **107**(2): p. 302-311.
164. Di Carlo, D., et al., *Continuous inertial focusing, ordering, and separation of particles in microchannels.* Proceedings of the National Academy of Sciences, 2007. **104**(48): p. 18892-18897.
165. Cleary, J., D. Maher, and D. Diamond, *Development and deployment of a microfluidic platform for water quality monitoring*, in *Smart Sensors for Real-Time Water Quality Monitoring*. 2013, Springer. p. 125-148.
166. Jaywant, S.A. and K.M. Arif, *A comprehensive review of microfluidic water quality monitoring sensors.* Sensors, 2019. **19**(21): p. 4781.
167. Nam, J., et al., *Microfluidic device for sheathless particle focusing and separation using a viscoelastic fluid.* Journal of Chromatography A, 2015. **1406**: p. 244-250.
168. Nam, J., et al., *Continuous separation of microparticles in a microfluidic channel via the elasto-inertial effect of non-Newtonian fluid.* Lab on a Chip, 2012. **12**(7): p. 1347-1354.
169. Lu, X., et al., *Particle manipulations in non-Newtonian microfluidics: A review.* Journal of colloid interface science, 2017. **500**: p. 182-201.
170. Zhang, J., et al., *A novel viscoelastic-based ferrofluid for continuous sheathless microfluidic separation of nonmagnetic microparticles.* Lab on a Chip, 2016. **16**(20): p. 3947-3956.
171. Zhou, Y., et al., *Submicron particle focusing and exosome sorting by wavy microchannel structures within viscoelastic fluids.* Analytical chemistry, 2019. **91**(7): p. 4577-4584.
172. Sabaghan, A., et al., *Nanofluid flow and heat transfer in a microchannel with longitudinal vortex generators: two-phase numerical simulation.* Applied Thermal Engineering, 2016. **100**: p. 179-189.

APPENDICES

Appendix A: python code to calculate fraction of focused particles

```
#
import cv2
import pylab
import itertools
from scipy import ndimage
import scipy.stats as st
from os import listdir
from os.path import isfile, join
import numpy as np
import matplotlib.pyplot as plt
from matplotlib.ticker import PercentFormatter
from scipy.stats import gaussian_kde
import xlwt
from tempfile import TemporaryFile
%matplotlib inline

centers_list = []
total = 0
im_l_t = 0
mypath = '/Users/mchar/Desktop/Feb 27th/slices-10mlhr-15' # The path of saved image sequence
print('DIR: ', mypath)
onlyfiles = [ f for f in listdir(mypath) if isfile(join(mypath,f)) ]
im = np.empty(len(onlyfiles), dtype=object)
for n in range(0, len(onlyfiles)):
  im[n] = cv2.imread( join(mypath,onlyfiles[n]) )
  gray = cv2.cvtColor(im[n], cv2.COLOR_BGR2GRAY)
  gray = cv2.GaussianBlur(gray, (5,5), 0)
  maxValue = 255
  adaptiveMethod =
cv2.ADAPTIVE_THRESH_GAUSSIAN_C#cv2.ADAPTIVE_THRESH_MEAN_C
#cv2.ADAPTIVE_THRESH_GAUSSIAN_C
  thresholdType = cv2.THRESH_BINARY#cv2.THRESH_BINARY
#cv2.THRESH_BINARY_INV
  blockSize = 7 # odd number like 3,5,7,9,11
  C = -3 # constant to be subtracted
  im_thresholded = cv2.adaptiveThreshold(gray, maxValue, adaptiveMethod, thresholdType,
blockSize, C)
  labelarray, particle_count = ndimage.measurements.label(im_thresholded)
  im_center = ndimage.measurements.center_of_mass(gray)
  im_l = list(im_center)
```

```
  im_l_t = im_l_t + im_l[0] * 2
  centers = ndimage.measurements.center_of_mass(im_thresholded, labels=labelarray,
index=range(1, particle_count+1))
  centers_list.append(centers)
  total = total + particle_count
print('Total Number of Particles: ', total)
im_l_wt = im_l_t / (len(onlyfiles) + 1)
print('Image Length: ', im_l_wt)
centers_list_f = list(itertools.chain(*centers_list))
a, b = zip(*centers_list_f)
x = list(a)
x_st15_1 = [ j / im_l_wt for j in x]


plt.rcParams['figure.figsize'] = 20,12
plt.xlim (0 , 1)
plt.ylim (0 , 19)
density = gaussian_kde(x_st15_1)
xs = np.linspace(0,1.0,400)
density.covariance_factor = lambda : .02
density._compute_covariance()
plt.plot(xs,density(xs),color = 'black')
plt.xlabel('Channel Width (%)', fontsize=30)
plt.ylabel('Fraction of Particles (%)', fontsize=30)
plt.xticks(fontsize=30)
plt.yticks(fontsize=30)
plt.show()

book = xlwt.Workbook()
sheet1 = book.add_sheet('sheet1')

for i,e in enumerate(x_st15_1):
    sheet1.write(i,1,e)

name = "10mlhr-15.xls"
book.save(name)
book.save(TemporaryFile())
```